

AN ABSTRACT OF THE THESIS OF

Tammy G. Amos for the degree of Doctor of Philosophy in Chemistry presented on October 24, 2000.

Title: Negative Thermal Expansion in AOMO₄ Compounds

Redacted for Privacy

Abstract approved: _____

Arthur W. Sleight

Several members of the AOMO₄ family have been evaluated for their potential as negative thermal expansion (NTE) materials. In these systems the A and M pentavalent cations are coordinated by oxygen to form octahedra and tetrahedra, respectively, and their overall connectivity consists of a three-dimensional framework built of corner-shared polyhedra. The structures of tetragonal NbOPO₄, TaOPO₄, monoclinic NbOPO₄, orthorhombic TaOVO₄, and a solid solution member of the Ta-V-As-O system were investigated as a function of temperature using diffraction techniques.

All structural work was carried out using X-ray powder diffraction measurements and in some cases high-resolution powder neutron diffraction. Dilatometry and differential scanning calorimetry were employed for preliminary thermal analysis to gain an understanding of the bulk thermal expansion and transition temperatures. Computer simulations were compiled using two separate

computer programs, Distance Least Squares and CRUSH, both of which give an indication of the flexibility of the framework structures studied.

A phase transition was found for most of the compounds studied. Negative thermal expansion was seen in the high temperature polymorphs of NbOPO_4 and TaOPO_4 and also in the orthorhombic TaOVO_4 structure.

One mechanism for negative thermal expansion has been identified for all these NTE compounds. This is based on the transverse motion of the polyhedral bridging oxygen atoms.

Negative Thermal Expansion in $AOMO_4$ Compounds

by

Tammy G. Amos

A THESIS

submitted to

Oregon State University

in partial fulfillment of
the requirements for the degree of

Doctor of Philosophy

Completed October 24, 2000
Commencement June 2001

Doctor of Philosophy thesis of Tammy G. Amos presented on October 24, 2000.

APPROVED:

Redacted for Privacy

Major Professor, representing Chemistry

Redacted for Privacy


Chair of the Department of Chemistry

Redacted for Privacy


Dean of Graduate School

I understand that my thesis will become part of the permanent collection at Oregon State University libraries. My Signature below authorizes release of my thesis to any reader upon request.

Redacted for Privacy

Tammy G. Amos, Author

Acknowledgement

I wish to convey my deepest appreciation and respect for my advisor, Dr. Arthur Sleight. It was with his patience, guidance, and friendship that made it possible for me to pursue and obtain success. His extensive knowledge, intuition, and enthusiasm for our work have been constant sources of encouragement. He has let me set my own pace and find my way through this process and has always remained extremely supportive. I consider myself very honored to have worked with him.

I would like to extend my appreciation for my committee members for their time and commitment to my program: Dr. Carroll DeKock, Dr. Douglas Keszler, Dr. John Loeser, and Dr. William Warnes.

I want to acknowledge my co-workers in the Sleight group: Rebecca Bliesner, Dr. Uma Sitharaman, Ju-Zhou Tao, Dr. Alex Yokochi, Chris Pyle, Xiumei Xun, Jun Li, Dr. Nagarajan Rajamani, Vanaja Achuthan, Dr. Niangao Duan, and Sasha Oblezov for their support and valuable discussions.

Many people have come and gone in the Sleight group and I wish to recognize some of the ones I knew. Thanks to Dr. Martin Atfield for getting me started with the Rietveld method, Dr. Ivana Radosavljevic for teaching me the basics of crystallography and spending a fantastic four days collecting data at NIST together, and Dr. Kameswari Upadhyala for being my home-away-from-home mother figure in the lab and introducing me to fine Indian cuisine.

Special thanks go to (soon-to-be-Dr.) Nipaka Sukpirom and Dr. Karen Castle for their very valued friendships.

I would like to thank Dr. Brian Toby and Dr. Judy Stallick for their help with data collection at NIST. I look forward to my collaboration with both of them in the future. Also I would like to acknowledge the assistance of Dr. Mas A. Subramanian with the DuPont Co. for his preparation of the tetragonal form of TaOPO₄.

Thanks to my father and mother for always supporting my decisions and being proud of their daughter who chose to do something different.

My work and life would not be complete without the constant love and support from my husband, John Cowgill. Thank you for always being there and encouraging me to do my best and beyond.

Table of Contents

	<u>Page</u>
1. Introduction	1
1.1. Negative Thermal Expansion	1
1.2. AOMO ₄ Family	9
1.2.1. Polymorphs of Niobium Orthophosphate	9
1.2.2. Polymorphs of Tantalum Orthophosphate	18
1.2.3. Orthorhombic TaOVO ₄	19
1.2.4. Orthorhombic NbOVO ₄	21
1.2.5. Tetragonal MoOPO ₄	23
1.2.6. Tantalum Orthoarsenate	23
1.2.7. Polymorphs of Niobium Orthoarsenate.....	24
1.2.8. Polymorphs of Vanadium Orthophosphate	27
1.2.9. Vanadium Orthoarsenate.....	30
1.2.10. Antimony Orthophosphate	31
1.2.11. VOSO ₄ and VOMoO ₄	32
1.3. References	34
2. Negative Thermal Expansion in the High Temperature Polymorph of Tetragonal NbOPO₄	42
2.1. Introduction	42
2.2. Experimental.....	42
2.3. Description of Structure.....	44
2.4. Preliminary Thermal Analysis.....	48
2.5. Structural Refinements	49
2.6. High Temperature Phase Transition	51
2.7. Distance Least Squares Results	58
2.8. Discussion.....	62
2.9. References	64

Table of Contents (Continued)

	<u>Page</u>
3. Phase Transition in Monoclinic NbOPO₄	65
3.1. Introduction	65
3.2. Experimental.....	65
3.3. Description of Structure.....	67
3.4. Preliminary Thermal Analysis.....	68
3.5. Structural Refinements	69
3.6. High Temperature Phase Transition	74
3.7. Discussion.....	94
3.8. References	101
4. Negative Thermal Expansion in the High Temperature Polymorph of Tetragonal TaOPO₄	102
4.1. Introduction	102
4.2. Experimental.....	102
4.3. Description of Structure.....	104
4.4. Structural Refinements	106
4.5. High Temperature Phase Transition	112
4.6. Discussion.....	119
4.7. References	120
5. Negative Thermal Expansion in Orthorhombic TaOVO₄	121
5.1. Introduction	121
5.2. Experimental.....	122

Table of Contents (Continued)

	<u>Page</u>
5.3. Description of Structure.....	123
5.4. Preliminary Thermal Analysis.....	124
5.5. Structural Refinements	126
5.6. Discussion.....	129
5.7. TaAs _x V _{1-x} O ₅ Solid Solutions	141
5.7.1. Experimental	141
5.7.2. Results and Discussion.....	142
5.7.3. Thermal Expansion Properties of TaAs _{0.1} V _{0.9} O ₅	142
5.8. References	148
6. A Comparative Analysis of AOMO₄ Structures and Future Work .	149
6.1. Polymorphs.....	149
6.2. Octahedral Distortions.....	151
6.3. Phase Transitions.....	152
6.4. Suggestions for Future Work.....	155
6.5. References	156
Bibliography.....	157

List of Figures

<u>Figure</u>		<u>Page</u>
1.1.	A schematic of the potential energy diagram for a harmonic oscillator	2
1.2.	A schematic of the potential energy diagram for an anharmonic oscillator	3
1.3.	Polyhedra connectivity in tetragonal NbOPO ₄	10
1.4.	Octahedral distortions in the NbO ₆ chains	11
1.5.	Schematic representation of n water molecules in between layers of NbOPO ₄	12
1.6.	Polyhedra connectivity in monoclinic NbOPO ₄	17
1.7.	Polyhedra connectivity in orthorhombic TaOVO ₄	20
1.8.	Polyhedra connectivity in monoclinic α -NbOAsO ₄	25
1.9.	The NbAsO ₅ structure (left) is cleaved along the long Nb-O bonds to form the RbNbAsO ₅ Cl structure (right)	26
1.10.	Polyhedra connectivity in orthorhombic β -NbOAsO ₄	27
1.11.a.	-P-O(2)-V-O(2)-P- chain in α_I -VOPO ₄	29
1.11.b.	-P-O(2)-V-O(2)-P- chain in α_{II} -VOPO ₄	29
1.12.	Polyhedra connectivity in LiVOAsO ₄ along the <i>bc</i> plane	31
2.1.	Coordination of niobium and phosphorus	45
2.2.	Polyhedra connectivity in tetragonal NbOPO ₄	46
2.3.	Ferroelectric-type distortion along the NbO ₆ octahedral chains	47
2.4.	Dilatometer curve for tetragonal NbOPO ₄	48
2.5.	Cell dimensions <i>a</i> and <i>c</i> as a function of temperature.....	52

List of Figures (Continued)

<u>Figure</u>		<u>Page</u>
2.6.	Variation of O(2) x parameter with temperature	54
2.7.a.	Observed, calculated, and difference profiles for tetragonal NbOPO ₄ at 25 °C	55
2.7.b.	Observed, calculated, and difference profiles for tetragonal NbOPO ₄ at 327 °C	55
2.8.	Anisotropic thermal parameters for metal atoms	59
2.9.	Anisotropic thermal parameters of oxygen atoms	60
2.10.	Variation of a cell edge with O2 x position	61
2.11.	Structure of tetragonal NbOPO ₄ viewed down the c axis. Central structure is in space group $P4/nmm$. The tilted structures to each side are in space group $P4/n$	63
3.1.	Polyhedra connectivity in monoclinic NbOPO ₄ looking down the a axis	67
3.2.	Differential scanning calorimetry plot for monoclinic NbOPO ₄	68
3.3.	Le Bail refinement plot for monoclinic NbOPO ₄ at 20 °C. The Si standard is marked with an *	70
3.4.a.	Rietveld refinement plot with no preferred orientation parameter refined	71
3.4.b.	Rietveld refinement plot after refinement with preferred orientation parameter	71
3.5.a.	Observed, calculated, and difference profiles for NbOPO ₄ at 25 °C	73
3.5.b.	Observed, calculated, and difference profiles for NbOPO ₄ at 340 °C	73
3.6.	Polyhedra connectivity in orthorhombic NbOPO ₄ looking down the a axis	75

List of Figures (Continued)

<u>Figure</u>		<u>Page</u>
3.7.	Cell dimensions a and b determined by neutron diffraction (open circles) and X-ray diffraction (closed diamonds) analysis	76
3.8.	Cell dimensions c and β determined by neutron diffraction (open circles) and X-ray diffraction (closed diamonds) analysis	77
3.9.	Changes in volume with temperature	78
3.10.	Isotropic thermal parameters for niobium and phosphorus atoms.....	86
3.11.	Isotropic thermal parameters for oxygen atoms	87
3.12.	Partial view of the anisotropic thermal parameters in the orthorhombic NbOPO ₄ structure looking down the a axis.....	88
3.13.a.	Titling angles in the monoclinic NbOPO ₄ structure.....	93
3.13.b.	Tilting angles in the orthorhombic NbOPO ₄ structure	93
3.14.	Polyhedra tilt angles as a function of temperature	94
3.15.	Partial view of the anisotropic thermal parameters in the orthorhombic NbOPO ₄ structure looking down the b axis.....	96
3.16.	Schematic of decreasing metal-metal bonds	97
3.17.	Changes in metal-oxygen-metal angles with temperature.....	98
3.18.	Changes in average P-O bond distance with temperature	99
3.19.	Possible rocking motion for NbOPO ₄ looking down the a axis.....	100
4.1.	Polyhedra connectivity in tetragonal TaOPO ₄	104
4.2.	Ferroelectric-type distortion along the TaO ₆ octahedral chains.....	105

List of Figures (Continued)

<u>Figure</u>	<u>Page</u>
4.3.a.	Observed, calculated, and difference profiles for tetragonal TaOPO ₄ at 25 °C..... 108
4.3.b.	Observed, calculated, and difference profiles for tetragonal TaOPO ₄ at 600 °C..... 108
4.4.	Peak broadening in the tetragonal TaOPO ₄ sample 109
4.5.	Variation of cell edge lengths with temperature..... 114
4.6.	Variation of volume with temperature 115
4.7.	Structure of tetragonal TaOPO ₄ looking down the <i>c</i> axis. Central structure represents the <i>P4/nmm</i> setting and the tilted versions on each side are in space group <i>P4/n</i> 116
4.8.a.	Partial view of the tetragonal TaOPO ₄ structure in the <i>P4/n</i> space group..... 118
4.8.b.	Partial view of the tetragonal TaOPO ₄ structure in the <i>P4/nmm</i> space group..... 118
5.1.	Polyhedra connectivity in orthorhombic TaOVO ₄ along the <i>bc</i> plane..... 124
5.2.	Dilatometer plot for orthorhombic TaOVO ₄ 125
5.3.	Differential scanning calorimetry plot for orthorhombic TaOVO ₄ 126
5.4.a.	Observed, calculated, and difference profiles for orthorhombic TaOVO ₄ at 25 °C 128
5.4.b.	Observed, calculated, and difference profiles for orthorhombic TaOVO ₄ at 600 °C 128
5.5.	Changes in <i>a</i> and <i>b</i> cell edges as a function of temperature..... 130
5.6.	Changes in <i>c</i> and volume as a function of temperature..... 131

List of Figures (Continued)

<u>Figure</u>		<u>Page</u>
5.7.	Polyhedra connectivity along the <i>ab</i> and <i>ac</i> planes.....	132
5.8.	Variation of isotropic thermal parameters with temperature.....	135
5.9.a.	Variation of V-O bond lengths with temperature.....	137
5.9.b.	Variation of Ta-O bond lengths with temperature	137
5.10.	Bridging oxygen atoms in the polyhedra linkages	138
5.11.	Possible polyhedral tilt that results in negative thermal expansion.....	140
5.12.	Cell dimensions as a function of As concentration, x	143
5.13.	Variation of <i>a</i> and <i>b</i> cell edges with temperature.....	145
5.14.	Variation of <i>c</i> cell edge and volume with temperature.....	146
5.15.	Variation of metal-oxygen bond lengths with temperature.....	147
6.1.	Chains of corner-shared polyhedra in tetragonal AOMO ₄ compounds.....	149
6.2.a.	Chains of corner-shared polyhedra in monoclinic AOMO ₄ compounds.....	150
6.2.b.	Chains of corner-shared polyhedra in orthorhombic AOMO ₄ compounds	150

List of Tables

<u>Table</u>	<u>Page</u>
1.1. Reported Information on Selected AOMO ₄ Compounds	15
2.1. Atomic Coordinates for Tetragonal NbOPO ₄	44
2.2. Refinement Statistics for Tetragonal NbOPO ₄	50
2.3. Variation of Atomic Coordinates with Temperature.....	53
2.4. Selected Interatomic Bond Distances (Å)	56
2.5. Selected Bond Angles (°).....	57
3.1. Neutron Diffraction Refinement Statistics for NbOPO ₄	72
3.2. Thermal Expansion Coefficients for NbOPO ₄	79
3.3. Atomic Coordinates for Monoclinic NbOPO ₄ at 25 and 200 °C..	80
3.4. Atomic Coordinates for Monoclinic NbOPO ₄ Converted to the Orthorhombic Setting at 25 and 200 °C.....	81
3.5. Atom Transformation from the Monoclinic to the Orthorhombic Setting	82
3.6. Atomic Coordinates for Orthorhombic NbOPO ₄ at 325 and 400 °C	83
3.7. Displacement Distances from Each Monoclinic Atom to the Equivalent Orthorhombic Atom	85
3.8. Selected Bond Distances for 25 and 200 °C Data	89
3.9. Selected Bond Distances for 325 and 400 °C Data	90
3.10. Refined Anisotropic Thermal Parameters (Å ²) for 325 and 400 °C Data.....	91
3.11. Corrected Bond Distances for 325 and 400 °C Data	92
4.1. X-ray Diffraction Refinement Statistics for Tetragonal TaOPO ₄	107

List of Tables (Continued)

<u>Table</u>		<u>Page</u>
4.2.	Strain Values for Tetragonal TaOPO ₄	110
4.3.	Particle Sizes for Tetragonal TaOPO ₄	111
4.4.	Thermal Expansion Coefficients for Tetragonal TaOPO ₄	113
4.5.	Variation of Atomic Coordinates with Temperature.....	117
5.1.	Atomic Coordinates for Orthorhombic TaOVO ₄	123
5.2.	Refinement Statistics for Orthorhombic TaOVO ₄	127
5.3.	Thermal Expansion Coefficients for Orthorhombic TaOVO ₄	129
5.4.	Variation of Metal Atom Positions with Temperature.....	133
5.5.	Variation of O(2) Atom Positions with Temperature.....	133
5.6.	Variation of O(3) and O(4) Atom Positions with Temperature.....	134
5.7.	Variation of Selected Bond Distances (Å) with Temperature.....	139
5.8.	Refinement Statistics for TaAs _{0.1} V _{0.9} O ₅	144
5.9.	Coefficients of Thermal Expansion for TaAs _{0.1} V _{0.9} O ₅	144
6.1.	Phase Transitions of the Investigated Systems.....	152
6.2.	Polyhedra Volumes (Å ³) for the High Temperature Polymorphs.....	154
6.3.	Thermal Expansion Coefficients.....	155

Negative Thermal Expansion in AOMO₄ Compounds

Chapter 1

Introduction

1.1. Negative Thermal Expansion

Negative thermal expansion (NTE) in oxide compounds has gained considerable interest in recognition of the need for materials with tailored thermal expansion properties. In composites, compounds that contract when heated can be designed to compensate for the undesired positive expansion of other phases. Advancing the understanding of the behavior of such NTE materials has both scientific and technological significance.

Thermal expansion of solids is one physical property that depends on the nature of the inter-atomic binding forces. As two atoms are brought together, attractive forces dominate the overall potential energy of the system until their distance becomes too short and bonding electrons cannot overcome the internuclear repulsion. It is at this point that the energy increases. Figure 1.1 shows a graphical form of a general interatomic potential for a simple harmonic oscillator. The attractive interactions involve a decrease in energy as two atoms come closer together and bond formation begins. The repulsion interaction of the electrons is reflected on the left side of the curve from the minimum and rising

with decreasing internuclear distance. If the temperature of this system increases from T_1 to T_2 there is no change in the equilibrium bond length, R (indicated by the arrows).

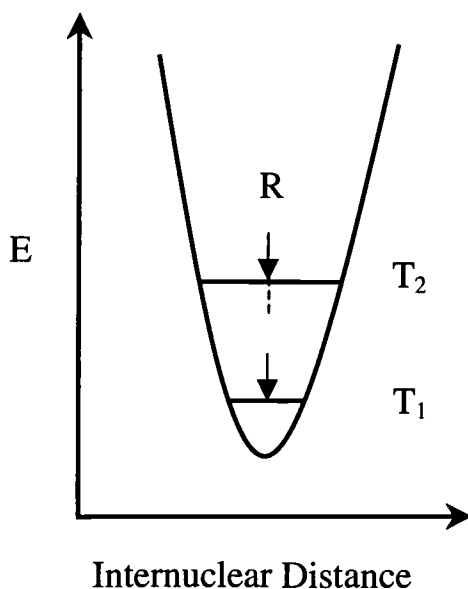


Figure 1.1. A schematic of the potential energy diagram for a harmonic oscillator

In reality atoms vibrate or oscillate in an anharmonic fashion. This anharmonicity gives rise to an asymmetric potential energy well. Figure 1.2 represents the variation of the potential energy with internuclear distance for an anharmonic oscillation. At one particular temperature, T_1 , the intersection of the horizontal line with the curve marks the extreme values of the internuclear distance where the oscillation energy is all potential energy. The midpoint of the line marks the mean value. As the temperature is increased to T_2 , the mean value

shifts to larger distances, depending on the extent of asymmetry associated with the well. This increase in the mean internuclear distance is one contribution to thermal expansion. The asymmetry is dependent on bond strength. A weaker bond results in a more asymmetric well. This gives rise to greater bond expansion at elevated temperatures for the weaker bond.

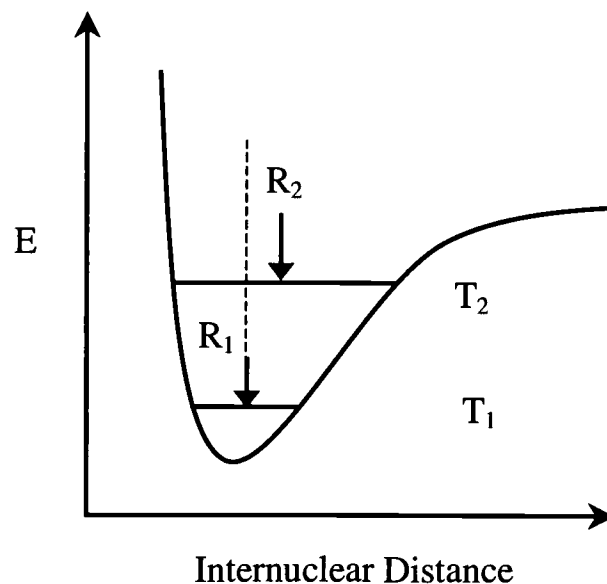


Figure 1.2. A schematic of the potential energy diagram for an anharmonic oscillator

This diagram can represent both an atom moving between certain points in the crystal and can also serve as a representation of a mode whose oscillation amplitude is related to some parameter in the crystal.

Based on this simple energy diagram, a common view of thermal expansion involves an increase in atomic separation and in atomic vibrations

when a solid is heated. This gives rise to a positive expansion. However, this does not explain how some crystals contract on heating. It becomes obvious that other factors must be considered when trying to understand how negative thermal expansion can occur. There have been a few structures found to demonstrate negative thermal expansion.

Roy and co-workers present a review of some very low thermal expansion coefficient materials (1), including β -spodumene ($\text{LiAlSi}_2\text{O}_6$), the cordierite family ($2\text{Mg}_2\text{O}\cdot 2\text{Al}_2\text{O}_3\cdot 5\text{SiO}_2$), and NZP ($\text{NaZr}_2\text{P}_3\text{O}_{12}$). They tabulate some general structural features associated with compounds that exhibit low and even negative thermal expansion, these include 1) strongly bonded polyhedra linked in three-dimensions, 2) an open structure, and 3) structures with ferromagnetic or ferroelectric microdomains. Strong bonds correspond to more symmetric potential energy diagrams and this leads to smaller changes in bond length as the temperature is increased. An open structure with large openings or cavities allows the lattice to absorb some of the thermal energy from transverse vibrations perpendicular to bond distances. Dimension changes caused by thermal energy can be somewhat compensated if a ferroic microdomain distribution can change over temperature. Megaw attempted to correlate crystal structure properties with thermal expansion (2). She incorporated the tilting effects of network structure polyhedra and electrostatic considerations in her discussion of thermal expansion. Both reports recognize the importance of examining the linkage and rotation of the polyhedral network when trying to understand bulk thermal expansion.

Smyth (3) commented on the role of transverse oxygen vibrations in the thermal expansion behavior of titania-silica glasses and β -spodumene. He discussed two cases, 1) when the oxygen lies on a straight line between its two cation neighbors and 2) when the oxygen lies to one side of the cation-cation line. In first case, simple motion perpendicular to this line brings about a decrease in the cation-cation distance. If the cation-oxygen-cation angle is less than 180° then the motions that contribute to negative thermal expansion are vibrations parallel to the cation-cation line and rotations around this line.

In 1998, Sleight presented an overview of compounds that contract on heating (4). Some materials have been found to contract in one or more directions when heated and a few mechanisms for NTE have been explained. However, the compounds most significantly noted are those based on open framework structures where the oxygen atoms are in two-fold coordination and the framework polyhedra have the ability to tilt in different directions.

Our research group has been exploring negative thermal expansion in network structures where polyhedra share corners only. For networks with oxygen in two-fold coordination there are constraints on possible formulas (4). An oxide that contains only corner-shared octahedra will have the general formula AO_3 , while one that consists of corner-shared tetrahedra is represented by the general formula of MO_2 . Combinations of octahedra and tetrahedra lead to the formulas AM_2O_7 , $A_2M_3O_{12}$, and AMO_5 , where the A and M represent octahedrally and tetrahedrally coordinated cations, respectively.

Thermal expansion data has been reported for ZrP_2O_7 (5), ZrV_2O_7 (6), HfV_2O_7 , and HfP_2O_7 systems (5). These materials undergo phase transitions at low temperatures. Below the phase transition the cell volumes increase as the temperature is raised. At higher temperatures these materials exhibit negative thermal expansion. The NTE seen at high temperatures has been attributed to the transverse thermal motion of oxygen atoms in the metal-oxygen-metal linkages.

Similar conclusions about the mechanism of NTE have been deduced for members of the $\text{A}_2\text{M}_3\text{O}_{12}$ family (7-10). NTE is seen in $\text{Sc}_2\text{W}_3\text{O}_{12}$ (8), $\text{Y}_2\text{W}_3\text{O}_{12}$ (9), and $\text{Lu}_2\text{W}_3\text{O}_{12}$ (10) over specific temperature ranges. Evans et al. reported a monoclinic to orthorhombic phase transition in $\text{Sc}_2\text{Mo}_3\text{O}_{12}$ (11). They impute the NTE seen in the orthorhombic phase to low-energy vibrational modes, mainly accessible through the transverse motions of bridging oxygen atoms.

Another structure that has gained considerable interest for its negative thermal expansion is cubic zirconium tungstate, ZrW_2O_8 (12, 13). This structure is similar to the AM_2O_7 family except that the WO_4 tetrahedral groups in ZrW_2O_8 are not linked to each other. This lends to more flexibility in the ZrW_2O_8 structure.

The flexibility of network structures has been recognized as an important factor for understanding how structures react to certain conditions such as changes in temperature or pressure (14). Flexibility relates to the ease with which some polyhedra in a network can tilt or rock back and forth. Polyhedra sizes also play an important role in the flexibility of networks. In several members of the

AM₂O₇ family, as the polyhedra become larger, it is easier for them to change shape and the NTE is dependent on the more facile polyhedral rocking motions (4).

Dove and co-workers developed the idea of rigid unit modes (RUMs) (15). These are low-frequency phonon modes that arise from framework linkages that have some internal degrees of freedom that propagate without any distortions of the polyhedra. Giddy et al. describe a computational method for determining possible phonon modes in framework crystal structures that leave the fundamental polyhedra undistorted (16, 17). Their program is referred to as CRUSH.

In order to quantitatively compare the extent of thermal expansion or contraction in solids, the thermal expansion coefficient (α) can be calculated. This describes the dimensional change occurring with a change in temperature at constant pressure. The thermal expansion coefficient is defined in Equation 1.1.

$$\alpha_l = \frac{l - l_o}{l_o (T - T_o)} \quad \text{Equation 1.1}$$

where l_o and l represent the cell lengths at temperatures T_o and T , respectively. The volume thermal expansion coefficient can be approximated as the sum of the α 's using Equation 1.2.

$$\alpha_v \approx \alpha_a + \alpha_b + \alpha_c \quad \text{Equation 1.2}$$

where α_a , α_b , and α_c represent the thermal expansion coefficients of each dimension. The following derivation shows how the volume thermal expansion coefficient can be approximated as the above summation. Assume a_T , b_T , and c_T represent cell lengths at temperature T , a_o , b_o , and c_o represent initial lengths and α , β , and γ represent the different thermal expansion coefficients associated with lengths a , b , and c , it follows that:

$$a_T = a_o (1 + \alpha T)$$

$$b_T = b_o (1 + \beta T)$$

$$c_T = c_o (1 + \gamma T)$$

The volume at temperature T is defined by:

$$\begin{aligned} V_T &= a_T \times b_T \times c_T = a_o \times b_o \times c_o (1 + \alpha T) (1 + \beta T) (1 + \gamma T) \\ &= V_o (1 + \alpha T) (1 + \gamma T + \beta T + \beta \gamma T^2) \\ &= V_o (1 + \gamma T + \beta T + \beta \gamma T^2 + \alpha T + \alpha \gamma T^2 + \alpha \beta T^2 + \alpha \beta \gamma T^3) \\ &= V_o [1 + T(\gamma + \beta + \alpha) + T^2(\beta \gamma + \alpha \gamma + \alpha \beta) + T^3(\alpha \beta \gamma)] \end{aligned}$$

Differentiating this expression gives the following:

$$\frac{1}{V_o} \cdot \frac{dV_T}{dT} = (\alpha + \beta + \gamma) + 2T(\beta \gamma + \alpha \gamma + \alpha \beta) + 3T^2(\alpha \beta \gamma)$$

The last two terms are generally considered negligible and the volume thermal expansion coefficient can be approximated by the sum of the cell length thermal expansion coefficients.

This thesis work involves the investigation of the negative thermal expansion properties in the AMO_5 family of compounds.

1.2. AOMO₄ Family

The compounds under investigation can be represented by the general formula $AOMO_4$, where the A and M cations are coordinated by oxygen to form octahedra and tetrahedra, respectively. The connectivity of these structures results in three-dimensional frameworks built of corner-shared polyhedra. The synthesis methods of some of these compounds have been reported in literature, however, no systematic investigation of their structural properties as a function of temperature has been carried out.

1.2.1 Polymorphs of Niobium Orthophosphate

$NbOPO_4$ crystallizes in three polymorphs: monoclinic, orthorhombic, and tetragonal systems. These framework structures contain corner-shared NbO_6 octahedra and PO_4 tetrahedra. The connectivity linkages of the monoclinic and orthorhombic forms are similar, but both differ from those in the tetragonal phase.

Preparation and chemical analysis of tetragonal $NbOPO_4$ was first accomplished and reported by Hahn in 1951 (18). Four different methods were employed to synthesize the stable salt and the X-ray diffraction patterns were compared. The first three involved precipitation and ignition at 1000 °C. These gave identical characteristic X-ray diffraction patterns. In the fourth method,

Nb_2O_5 and an excess of concentrated phosphoric acid were mixed and heated at $1000\text{ }^\circ\text{C}$. The resulting diffraction pattern was similar to those obtained by the other methods, although, impurity peaks corresponding to the oxides were also present. Only un-indexed diffraction lines were reported.

Haider later established a tetragonal unit cell for this compound with unit cell axes of $a = 6.394\text{ \AA}$ and $c = 4.103\text{ \AA}$ (19). Longo and Kierkegaard determined the crystal structure of the tetragonal phase from a crystal grown by hydrothermal technique (20). The three-dimensional framework consists of chains of NbO_6 octahedra sharing opposite corners along the c axis (Figure 1.3). A layer of polyhedra has been omitted from this picture for clarity.

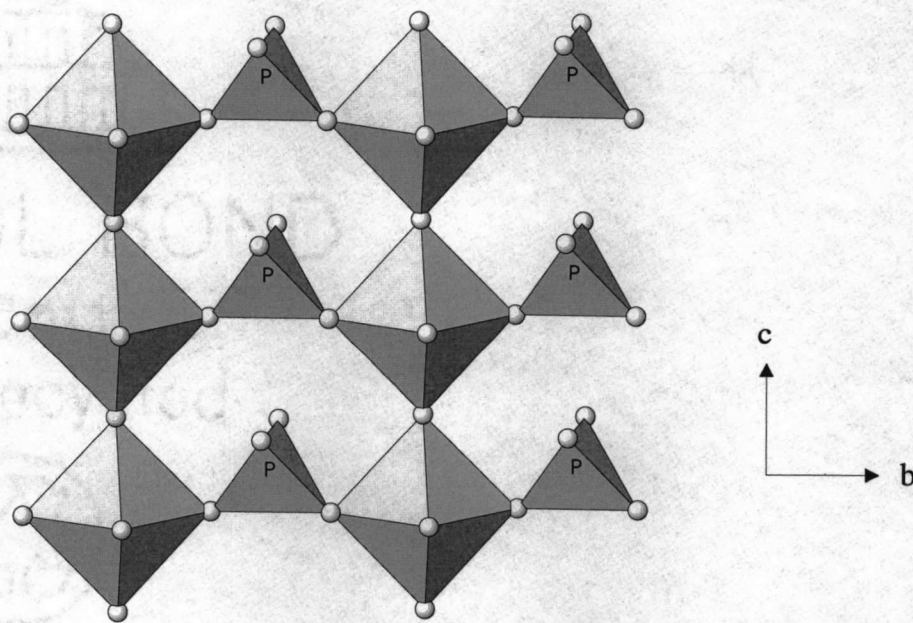


Figure 1.3. Polyhedra connectivity in tetragonal NbOPO_4

Along the NbO_6 chains there is a ferroelectric-type distortion in that one niobium atom is slightly displaced in the octahedral environment. Infrared measurements showed the presence of PO_4^{3-} groups and the stretching modes of both the short and long Nb-O bonds present in this structure (21). This material exhibits no ferroelectricity because adjacent chains of NbO_6 octahedra have opposite polarities and no net moment occurs over the entire structure (Figure 1.4).

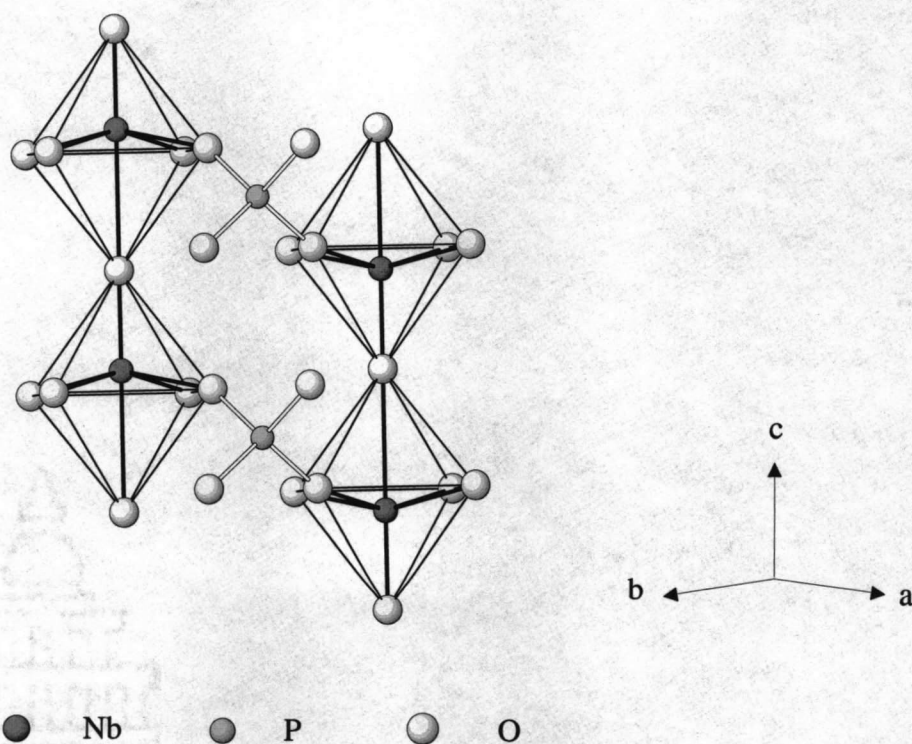


Figure 1.4. Octahedral distortions in the NbO_6 chains

Stranford and Condrate (22) reported that hydrated phases of NbOPO_4 involved incorporation of water between the layers via cleavage of the long Nb-O bonds. Figure 1.5 represents intercalation of water into the structure. Raman spectra were measured for hydrated NbPO_5 phases after different stages of dehydration. Analysis suggested that one water molecule bonds directly to a niobium ion and directly replaces the elongated van der Waal Nb-O bond, while another is located between phosphate groups of adjacent layers in the $\text{NbOPO}_4 \cdot 2\text{H}_2\text{O}$ structure.

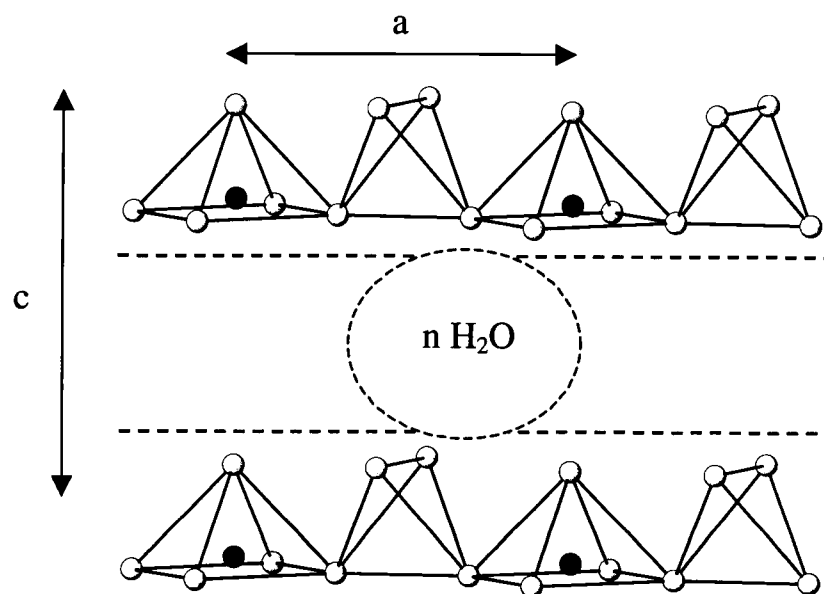


Figure 1.5. Schematic representation of n water molecules in between layers of NbOPO_4

NbOPO_4 hydrates exhibit rich interlayer chemistry. Preparation of the intercalated compounds involves the initial reaction with $\text{NbOPO}_4 \cdot x\text{H}_2\text{O}$.

Intercalation is achieved via replacement of water molecules in between the layers. Many different organic compounds have been intercalated into the tetragonal phase of $\text{NbOPO}_4 \cdot 2\text{H}_2\text{O}$. In an attempt to achieve unusual electrical, optical, and mechanical properties, Melanova et al. studied the intercalation of poly(ethylene) compounds into the hydrated NbOPO_4 and isomorphous MoOPO_4 host lattices (23). From basal spacing analysis, they determined that the polymer chains deposited parallel to the layers in the host material. Different amines can be intercalated into NbOPO_4 (24). Various alcohols have also been intercalated into this tetragonal structure (25, 26). In these cases alcohol molecules are placed between host layers in a bimolecular way, being anchored to them by donor-acceptor bonds between the Nb atom and the oxygen atom of the hydroxyl group as well as hydrogen bonds. Wang and co-workers have also presented the single crystal structure of amino acid intercalated layered niobium phosphate (27). NbOPO_4 layers are bridged by carboxylic groups of a particular amino acid with H_2PO_4 , F, and OH anions located in interlayer spaces. A similar structure of glycine intercalated NbOPO_4 was reported by Vitezslav, Benes and Melanova (28).

Johnson and Jacobson have patented the intercalation of lewis bases into the layered AOMO_4 compounds (29). These include different tetragonal phases of layered mixed oxides such as VOPO_4 , VOAsO_4 , VOMoO_4 , NbOPO_4 , NbOAsO_4 , TaOPO_4 and MoOPO_4 , the structures of which will be discussed later. In these cases, the adjacent layers of AOMO_4 are covalently bonded to the Lewis

base. A second patent (30) involves the intercalation of monovalent, divalent, or polyvalent cations into the hydrated forms of AOMO₄ compounds.

The NbOPO₄·2H₂O compound also permits the exchange of protons for Li⁺ ions (31). This study found a high ionic conductivity for LiNb(OH)OPO₄ that increases up to 880 K, above which the ionic conductivity discontinues due to Li⁺ ions finding permanent positions in the network. Lithium ion intercalation has also been investigated for solid solution structures of tetragonal Nb_{2-x}V_xO₅ (0.2 < x < 1.0) for potential in lithium battery cathode applications (32).

Many solid solutions have been prepared for the tetragonal NbOPO₄ structure. Both V⁵⁺ (32, 33) and Mo⁵⁺ ions (34) have been successfully substituted into the octahedral Nb⁵⁺ sites. The solid solution V_{1-x}Nb_xOPO₄ has been found to have high catalytic activity for the oxidation of butane to maleic anhydride (35). This catalyst has similar activity to the (VO)₂P₂O₇ compound and also provides strong Lewis acid sites. The catalysis ability of non-substituted NbOPO₄ has also been investigated for the preparation of benzonitrile from methyl benzoate and ammonia (36).

Levin and Roth determined a partial phase diagram for the Nb₂O₅-P₂O₅ system (37). They reported on the transformation of the tetragonal NbOPO₄ to a monoclinic phase at approximately 1250 °C. Only indexed diffraction peaks and unit cell dimensions were listed for the monoclinic NbOPO₄ phase (Table 1.1).

Infrared spectroscopy on the monoclinic polymorph carried out by Stranford and Condrate (38) show similarities with those done for the tetragonal phase (21). The bands between 580 and 890 cm⁻¹ were assigned to various

Table 1.1. Reported Information on Selected AOMO₄ compounds

Compound	Symmetry	S.G.	Ref.	a	b	c	b	d g/cm ³	diffraction
NbOPO ₄	T		19	6.394		4.103		4.039	powder
	T	P4/n	20	6.3873 (10)		4.1037 (8)		4.047	x-tal
	T		37	6.382 (1)		4.101 (1)		4.056	powder
	M		37	11.257 (2)	5.276 (1)	6.606 (1)	90.17 (1)	3.454	powder
	M	P2 ₁ /c	40	13.064 (5)	5.283 (2)	13.240 (4)	120.13 (2)	3.429	powder
	M	P2 ₁ /c	39	13.0969 (16)	5.2799 (6)	13.2281 (16)	120.334 (8)	3.433	x-tal
	TaOPO ₄	M	P2 ₁ /c	40	13.07 (1)	5.281 (4)	13.24 (1)	120.25 (4)	4.914
	M		37	11.272 (1)	5.281 (1)	6.621 (1)	90.13 (1)	4.921	powder
	T	P4/n	41	6.425 (3)		4.001 (3)		5.872	powder
TaOVO ₄	O	Pnma	42	11.860 (3)	5.516 (1)	6.928 (1)		4.572	powder
			43	11.85	5.505	6.923		4.589	powder
NbOVO ₄	O	Pnma	47	11.866 (4)	5.514 (1)	6.915 (2)		3.288	powder
Ta _{0.8} Nb _{0.2} VO ₅	O	Pnma	53	11.8899 (7)	5.5294 (4)	6.9505 (5)		4.279	powder
Ta _{0.5} Nb _{0.5} VO ₅	O	Pnma	53	11.8916 (9)	5.5309 (4)	6.9502 (6)		3.894	powder
Ta _{0.25} Nb _{0.75} VO ₅	O	Pnma	53	11.893 (1)	5.5327 (6)	6.9468 (9)		3.575	powder

Table 1.1., Continued

Compound	Symmetry	S.G.	Ref.	a	b	c	b	d g/cm ³	diffraction
MoOPO ₄	T	P4/n	55	6.1768 (3)		4.2932 (3)		4.197	x-tal
TaOAsO ₄			58	11.57	5.31	6.66			powder
NbOAsO ₄	T		59	6.57		4.67		4.086	powder
	M	P2/n	61	6.5343 (9)	4.0816 (8)	6.5317 (9)	90.002 (11)	4.728	x-tal
	O	Pnma	61	7.686 (1)	6.642 (1)	7.442 (1)		4.336	x-tal
VOPO ₄	O	Pnma	63	7.77 (3)	6.143 (3)	6.965 (3)		3.241	x-tal
α _I -VOPO ₄	T	P4/n	50	6.20 (2)		4.11 (2)		3.42	powder
α _{II} -VOPO ₄	T	P4/n	16	6.014 (7)		4.434 (2)		3.363	x-tal
SbOPO ₄	M	C2/c	4	6.791 (1)	8.033 (1)	7.046 (1)	115.9 (1)	4.476	x-tal
VOSO ₄	O	Pnma	102,103	7.3710 (12)	6.2692 (8)	7.0821 (9)		3.308	powder
	T	P4/n	105	6.261 (3)		4.101 (3)		3.388	powder
VOMoO ₄	T	P4/n	67	6.6078 (2)		4.2646 (3)		4.049	x-tal

stretching Nb-O modes and indicated the octahedrally coordinated Nb atom. Their results showed the short Nb-O bond of the monoclinic phase at lower wave numbers compared to that in the tetragonal phase, suggesting that the bond order for the related bonds is not as high as in the tetragonal phase. They contend that niobium and tantalum cations form more regular AO_6 octahedra in crystalline compounds with lower space group symmetry.

In 1986, LeClaire et al. presented complete structure information of the monoclinic phase based on single crystal X-ray diffraction analysis (39). They conclude that adjustment stresses induced by phosphate tetrahedra lead to different deformations that account for supercells seen in electron diffraction (40).

In this structure the connectivity of the polyhedra is such that there are zig-zag chains of NbO_6 octahedra along the b axis (Figure 1.6).

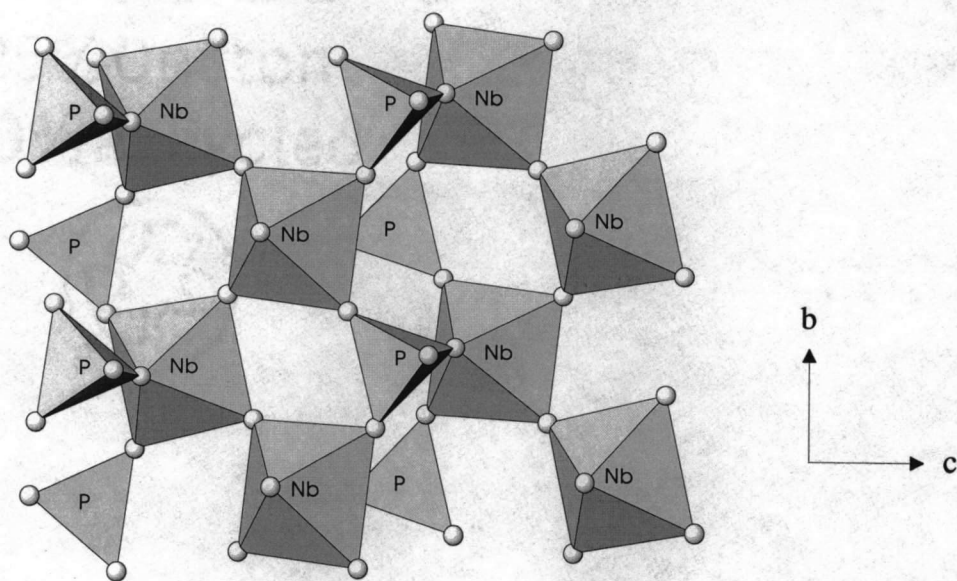


Figure 1.6. Polyhedra connectivity in monoclinic NbOPO_4

1.2.2. Polymorphs of Tantalum Orthophosphate

TaOPO₄ crystallizes in two different polymorphs, a monoclinic and tetragonal form. Both of these compounds are similar to those found in the niobium analogs.

Hahn prepared the monoclinic tantalum orthophosphate in 1951 (18). The synthesis used freshly prepared potassium tantalate and excess phosphoric and nitric acids. This mixture was digested in a water-bath for an hour and the resulting precipitate was centrifuged and washed with an acetone-water mixture. This was subsequently ignited at 1000 °C. Levin and Roth (37) reported the indexed powder diffraction pattern and the cell dimensions of monoclinic TaOPO₄ (Table 1.1). This structure was found to be isomorphous with the monoclinic NbOPO₄ compound (39).

Hydrated tantalum phosphate materials have also been prepared by initial precipitation of the materials from aqueous solution (41). These phases were amorphous when examined with X-ray diffraction. The dehydration of TaOPO₄·xH₂O results in the formation of crystalline monoclinic TaOPO₄.

The tetragonal phase of tantalum phosphate can be synthesized using high pressure (42). Longo and co-workers studied the formation of this compound over a range of 25 to 60 kbar and 500 to 1500 °C. It was found that at pressures greater than 25 kbar and over the entire temperature range studied, the monoclinic polymorph of TaOPO₄ transformed to a tetragonal phase that could be retained at

atmospheric pressure by quenching. This TaOPO₄ compound is isostructural with tetragonal NbOPO₄ (20) with similar cell dimensions (Table 1.1).

1.2.3 Orthorhombic TaOVO₄

In a study of the ZnO-Ta₂O₅-V₂O₅ system, Brown reported the formation of the 1:1 binary TaVO₅ compound (43, 44). No synthesis conditions were detailed except for the use of tantalum pentoxide and ammonium metavanadate as starting materials. They present dilatometer thermal expansion data. A coefficient of thermal expansion (α) of $-4.4 \times 10^{-7} \text{ }^\circ\text{C}^{-1}$ was reported over a temperature range of 25 to 700 °C. No structural information was discussed.

A powder sample of orthorhombic TaOVO₄ was prepared with soft thermal conditions by Chahboun et al. in 1988 (45). A mixture of V₂O₅ and defect pyrochlore H₂Ta₂O₆H₂O was heated at 873 K and then annealed for 12 hours at 1073 K. Cell dimensions and atomic positional parameters were reported. The polyhedra linkage is similar in monoclinic NbOPO₄ (20) and TaOPO₄ (37) structures, however the polyhedra are not as tilted in the orthorhombic structure and many of the atoms have moved onto mirror planes. A representation of the three-dimensional linkage can be seen in Figure 1.7.

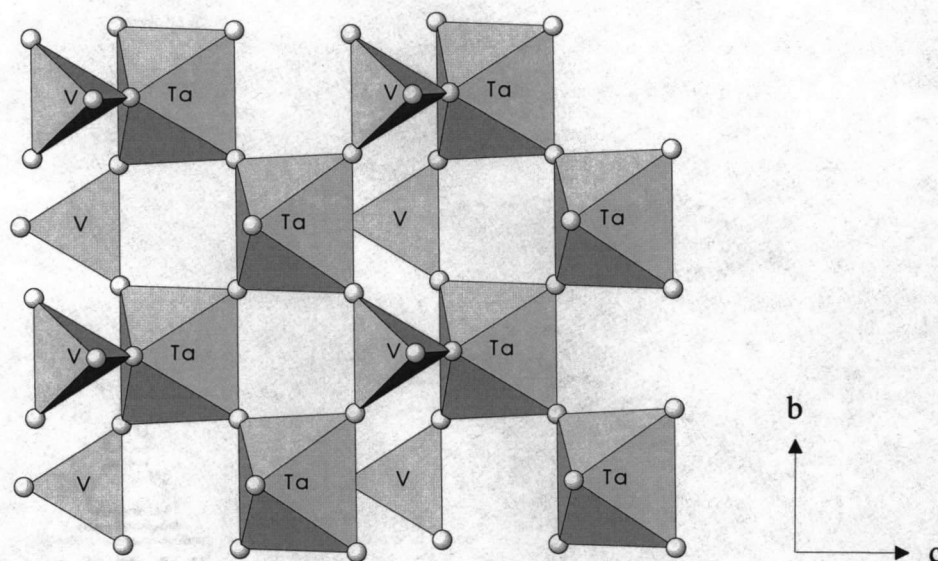


Figure 1.7. Polyhedra connectivity in orthorhombic TaOVO₄

The cell dimensions of the TaOVO₄ listed in Table 1.1 show an increase relative to the niobium phosphate analog. This is directly related to the increase in ionic radii for the vanadium ion relative to the tetrahedrally coordinated phosphorus. Infrared spectroscopy analysis showed a single band at 816 cm⁻¹ (corresponding to asymmetric stretching V-O bond), 684 cm⁻¹ (symmetric stretching Ta-O), and bands below 500 cm⁻¹ (O-V-O and coupled O-Ta-O bending) (45).

Compound formation in the Ta₂O₅-V₂O₅ system has been studied using amorphous materials prepared by the simultaneous hydrolysis of tantalum and vanadyl alkoxides (46). Three compounds were found to exist in this system: 9Ta₂O₅·V₂O₅, 9Ta₂O₅·2V₂O₅, and TaOVO₄. Orthorhombic TaOVO₄ crystallizes at approximately 540 °C and decomposes into 9Ta₂O₅·V₂O₅ and V₂O₅ at 1010 °C.

The thermal expansion coefficient of TaOVO₄ between 140 and 380 K was determined using dilatometry (47). From 140 K to about 260 K, the compound displayed positive thermal expansion and above this temperature the thermal expansion decreased as the temperature was raised. The thermal expansion coefficient for higher temperatures was found to be -4×10^{-6} /K. The authors indicate that there is a phase transformation that occurs near 260 K. No further conclusions on the nature of the phase transformation could be made on the basis of dilatometer data.

Skibsted and co-workers studied the TaOVO₄ compound using solid-state ⁵¹V NMR (48). The basis of this study focused on extracting structural information on the local environments of the vanadium nuclei. This technique can be extended to characterize complex catalytic systems where long-range order is absent.

1.2.4 Orthorhombic NbOVO₄

The phase diagram for the V₂O₅-Nb₂O₅ system developed by Waring and Roth shows a tendency to segregation of the orthorhombic V₂O₅ phase when the V₂O₅/Nb₂O₅ molar ratio is greater than 1/9 (49). Only about 5 mole percent of V₂O₅ could be accepted into the Nb₂O₅ solid solution using solid state synthesis techniques. The 1:1 composition of NbOVO₄ could not be synthesized in this study. Amarilla, Casal and Ruiz-Hitzky synthesized NbOVO₄ using a sol-gel method (50). Their preparation involved niobium pentachloride and vanadyl

triisobutoxide as starting materials. X-ray analysis showed that NbOVO₄ is isostructural with orthorhombic TaOVO₄ (45), their cell dimensions are compared in Table 1.1. Infrared spectroscopy measurements (50) gave information on the stretching and bending vibrations of the V-O and Nb-O bonds and were similar to those found for the orthorhombic TaOVO₄. The isostructural local environments are reflected in the optimized ⁵¹V NMR data (51), which show similarities for the quadrupole coupling. A separate study done by Davis et al. investigated the NbOVO₄ compound with ⁵¹V and ⁹³Nb high resolution NMR by comparison with V₂O₅ and LiNbO₃ structures (48). The distortion of the VO₄ tetrahedra is smaller in the NbOVO₄ case than in V₂O₅ and the shielding of the Nb nucleus is much more efficient when compared to LiNbO₃.

Amarilla and co-workers have studied Li⁺ insertion into the orthorhombic structures of NbOVO₄ and TaOVO₄ (52, 53) for their potential as electrode materials in solid-state battery applications. Lithium intercalation limits achieved after the reduction process were $x = 1.95$ for NbVO₅ and $x = 1.57$ for TaVO₅. These compounds show a good reversibility of the Li⁺ insertion process.

Electron transfer in the hydrogen intercalated MVO₅ (M = Nb, Ta) compound has been reported (54). The oxidation ability of the vanadium cation allows for the complete charge transfer from the intercalated hydrogen ion to the host lattice.

Ternary oxides of the general formula Ta_xNb_{1-x}VO₅ ($0 < x < 1$) have been synthesized via sol-gel route (55) similar to the preparation for orthorhombic NbOVO₄. The X-ray diffraction data indicate that the Ta_xNb_{1-x}VO₅ materials are

isostructural with the binary MVO_5 ($M = Nb, Ta$) (45, 50). Lithium intercalation has also been examined for the $Ta_xNb_{1-x}VO_5$ mixed oxides (56).

1.2.5 Tetragonal $MoOPO_4$

The structure of molybdenum orthophosphate was first presented by Kierkegaard and Westerlund (57) and later refined by Kierkegaard and Longo based on single crystal analysis (58). This compound is isostructural with the tetragonal form of $NbOPO_4$ (20) and $TaOPO_4$ (42). In 1984, Stranford and Condrate measured the vibrational spectra of the tetragonal $AOPO_4$ ($A = Nb, Mo, V$) compounds (59). Calculated force constants for the shortened A-O bonds indicate double bond character and those for the elongated A-O bonds suggest that the interaction forces between their atoms are weak Van der Waals type forces.

Lezama et al. investigated the magnetic properties of $MoOPO_4$ using ^{31}P NMR (60). These studies indicate 3D antiferromagnetic behavior below 18 K. This structure has mono-dimensional interactions along the c axis by direct or superexchange Mo-Mo coupling and interactions within the ab plane via phosphate tetrahedra.

1.2.6 Tantalum Orthoarsenate

Chernorukov and co-workers successfully prepared a polycrystalline compound of $TaOAsO_4$ (61). Their method involved dissolving metallic tantalum

in a mixture of HF/HNO₃, adding an excess of H₃AsO₄, washing the precipitate, and calcining at 800 °C. This reference does not report any structural data other than cell dimensions (Table 1.1).

1.2.7 Polymorphs of Niobium Orthoarsenate

A powder sample of NbOAsO₄·4H₂O, and its thermal dehydration product, NbOAsO₄ were first prepared by Chernorukov, Egorov, and Korshunova in 1979 (62, 63). Their X-ray diffraction analysis yielded unit cell dimensions and tetragonal cell symmetries for both compounds (Table 1.1). They proposed a hydrated structure with water molecules in between layers of NbAsO₅ and Nb atoms in pyramidal coordination.

Two different polymorphs of niobium arsenate have been structurally characterized by single crystal X-ray diffraction studies (64). A polycrystalline sample of α-NbOAsO₄ was prepared from Nb₂O₅ and As₂O₅ starting materials. These were loaded in a silica ampoule and sealed under vacuum. This was heated up to 300 °C, slow heated to 350 °C and maintained at this temperature for 12 hours. The temperature was then raised to 910 °C and held for 2 days, followed by quench cooling. The unit cell dimensions are listed in Table 1.1.

Single crystals of the monoclinic α form and orthorhombic β form were prepared with the β form as a precursor and an extensive heating program was employed. Thermogravimetric analysis (TGA) of the monoclinic NbOAsO₄ in a flow of oxygen showed peaks at 1050 and 1120 °C, corresponding to the

decomposition to $\text{Nb}_9\text{AsO}_{25}$ and Nb_2O_5 , respectively (determined by X-ray diffraction after each heating).

The linkage of the $\alpha\text{-NbOAsO}_4$ structure is very similar to the tetragonal phases of NbOPO_4 and TaOPO_4 (20, 42). Figure 1.8 shows a representation of the polyhedra in three dimensions. The structure consists of chains of corner-shared NbO_6 octahedra running parallel to the b axis. The O-Nb-O bond angle is 180° in this structure. Each octahedron is connected to two other NbO_6 octahedra in a trans configuration, while the apex corners share AsO_4 tetrahedra. Each AsO_4 tetrahedron shares its four corners with four different octahedral chains.

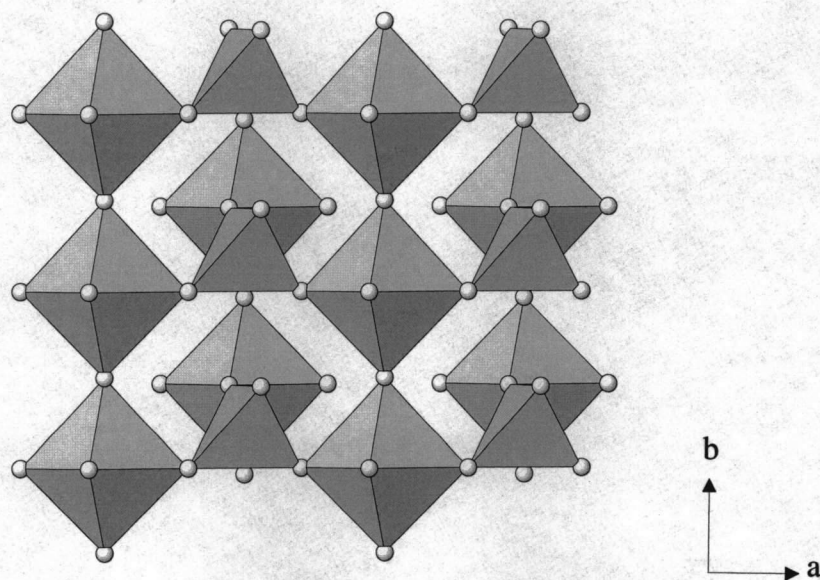


Figure 1.8. Polyhedra connectivity in monoclinic $\alpha\text{-NbOAsO}_4$

Original structure refinement with $P4/n$ (No. 85) symmetry resulted in very short As-As distances and negative thermal parameter values for two unique

oxygen atoms. This prompted the author to choose space group $P2/n$ (No. 13), a subgroup of $P4/n$ for the refinement.

Ulutagay and co-workers successfully synthesized single crystals of ANbAsO_5Cl ($A = \text{Rb}, \text{Cs}$) (65). These both crystallize in the tetragonal $P4/n$ space group. The analysis indicates that these have alternating layers of NbAsO_5 and ACl rock salt sheets. Figure 1.9 represents the coordination of NbAsO_5 intercalated with the RbCl salt. The NbAsO_5 lattice contains elongated Nb-O bonds along the c axis, these are broken to incorporate the Rb and Cl ions.

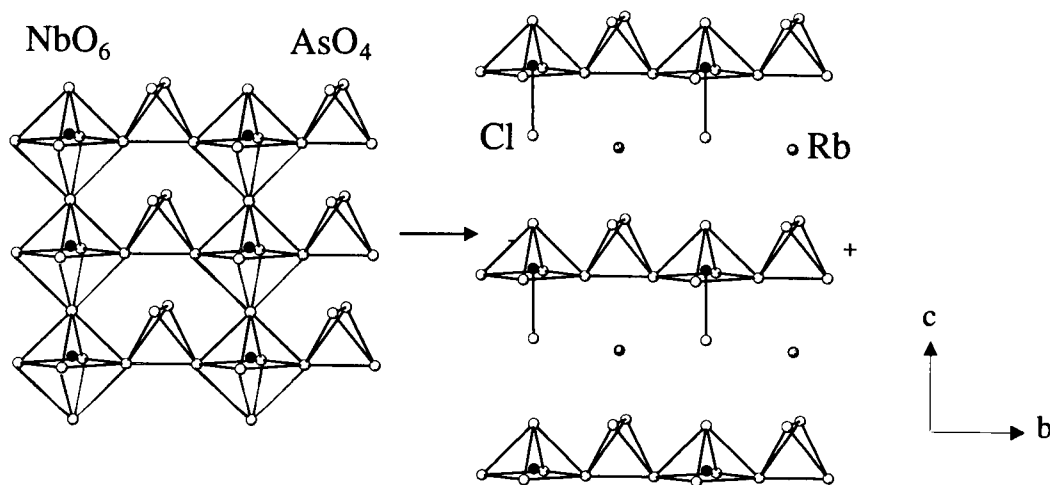


Figure 1.9. The NbAsO_5 structure (left) is cleaved along the long Nb-O bonds to form the $\text{RbNbAsO}_5\text{Cl}$ structure (right)

The $\beta\text{-NbOAsO}_4$ crystallizes in the orthorhombic space group $Pnma$ (No. 62). This structure contains NbO_6 octahedral chains with alternating long and

short Nb-O bond distances along the a axis. The main differences in this structure involve the connectivity of the AsO_4 tetrahedra. One AsO_4 tetrahedron is connected to two NbO_6 octahedra within the chain along the a axis, while the other two connect separate octahedra. This results in a buckling of the octahedral chain and a resulting Nb-O-Nb bond angle of approximately 151° (Figure 1.10).

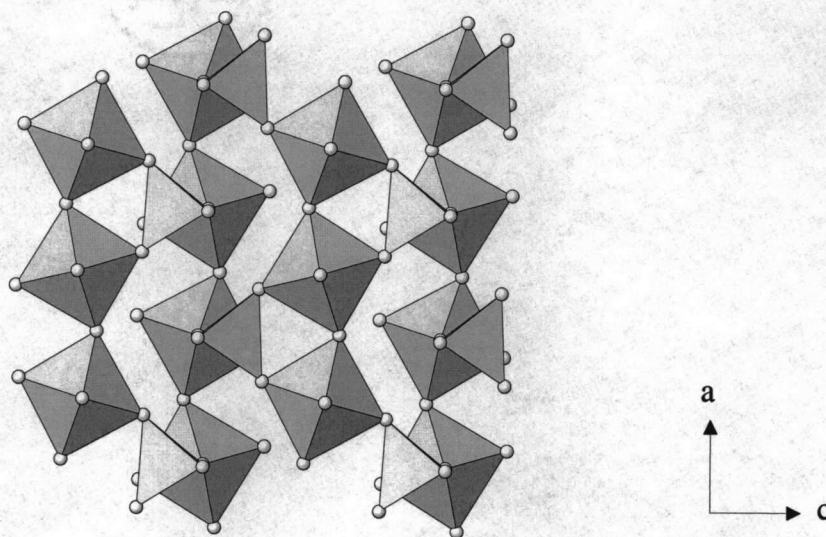


Figure 1.10. Polyhedra connectivity in orthorhombic $\beta\text{-NbOAsO}_4$

1.2.8 Polymorphs of Vanadium Orthophosphate

The pentavalent vanadium cation can also be found in octahedral coordination. VOPO_4 represents one such compound. Vanadium orthophosphate crystallizes in a tetragonal ($\alpha\text{-VOPO}_4$) and an orthorhombic ($\beta\text{-VOPO}_4$) form. Gopal and Calvo (66) reported the single crystal analysis for $\beta\text{-VOPO}_4$. They

describe the β -VOPO₄ as a framework structure with corner-sharing irregular VO₆ groups arrayed parallel to the a axis. The vanadium atom is displaced from the center of the octahedron. This structure is isomorphous with β -NbOAsO₄ (67).

Jordan and Calvo studied the crystal structure of α -VOPO₄ (68). This structure crystallizes in space group $P4/n$ and the linkage connectivity is similar to that of the tetragonal NbOPO₄ (20) and TaOPO₄ (42) compounds. Unlike reports for the tetragonal phases of NbOPO₄ and TaOPO₄, this study introduced disorder on an oxygen site (O2 in an xyz general position) due to an unusually large thermal displacement.

Tachez, Theobald and Bordes have proposed a structural distinction for two forms of tetragonal vanadium orthophosphate (α_I - and α_{II} - VOPO₄) according to the preparation method of α -VOPO₄ (69). The α_{II} -VOPO₄ type is isomorphous with tetragonal structures of NbOPO₄ (20), TaOPO₄ (42), MoOPO₄ (58), and VOMoO₄ (70). The α_I -VOPO₄ is obtained by decomposition of VOPO₄·2H₂O, and atoms are on the same side of the equatorial chain V-O(2)-P-O(2)-V, whereas in the α_{II} form, prepared by heating a mixture of oxides, these atoms are on alternate sides of that chain. Figure 1.11 shows the VO₆ octahedral connectivity for the α_I - and α_{II} - VOPO₄ compounds.

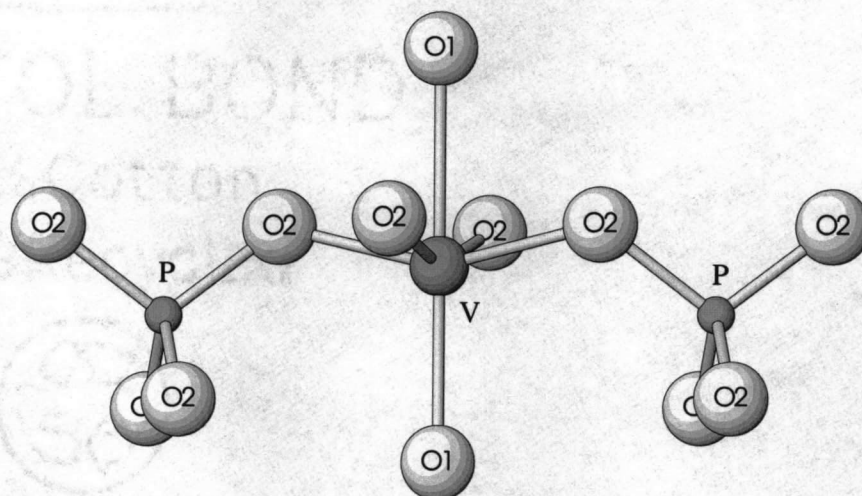


Figure 1.11.a. $-P-O(2)-V-O(2)-P-$ chain in α_I-VOPO_4

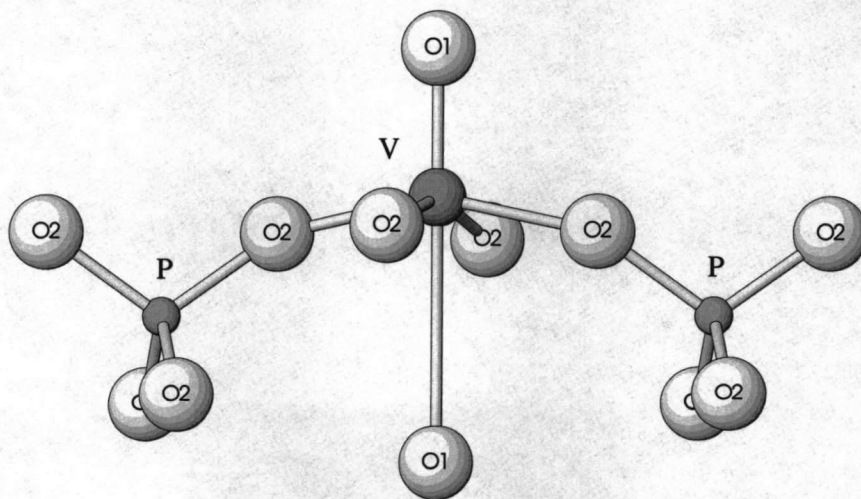


Figure 1.11.b. $-P-O(2)-V-O(2)-P-$ chain in $\alpha_{II}-VOPO_4$

Several intercalation studies have been done with the α_I-VOPO_4 structure and many review articles written (71-73). Intercalation reactions can be divided into two groups, the first involves acid-base interactions between the layered host

lattice (Lewis acid) and the guest (base). The second entails the reduction of V^{5+} to V^{4+} with intercalation of charged species to counterbalance the negative layer charge. Numerous investigations including the insertion of water (74-76), alcohols (77, 78), amines (79, 80), carboxylic acids (81), amides (82), glycine (83, 84), ferrocene and derivatives (85-87), and rhodium carbonyl (88) substitute through acid-base interactions with the $VOPO_4 \cdot 2H_2O$ structure. Redox intercalation of ammonium ions (89, 90) has been reported. The reaction of crystalline $VOPO_4 \cdot 2H_2O$ with an ethanolic solution of an iodide of alkali metals and Mg, Mn, Co, Ni or Zn ions constitutes a redox intercalation, (91-95). A barium derivative of the form $Ba(VOPO_4)_2 \cdot 4H_2O$ has also been identified (96). Lithium insertion has been examined and the conductance measured (92-95) for applications as solid-state battery electrodes.

1.2.9 Vanadium Orthoarsenate

Vanadyl arsenate forms several hydrates. $VOAsO_4 \cdot 3H_2O$ can be prepared by refluxing V_2O_5 and H_3AsO_4 . This hydrate converts to the dihydrate at 50 °C, the monohydrate at 85 °C, and finally complete dehydration occurs at 105 °C (97). The anhydrous $VOAsO_4$ is isomorphous with the tetragonal $AOMO_4$ compounds previously discussed. These hydrates have been the subject of many studies that include insertion of different amines (98), aliphatic carboxylic acids (99), and Li^+ ions (100).

The single crystal structure of LiVOAsO_4 was reported in 2000 (100). This orthorhombic compound has a three-dimensional linkage system similar to the tetragonal AOMO_4 compounds but with Li^+ ions inserted between the polyhedra. Figure 1.12 shows a perspective view of the LiVOAsO_4 structure.

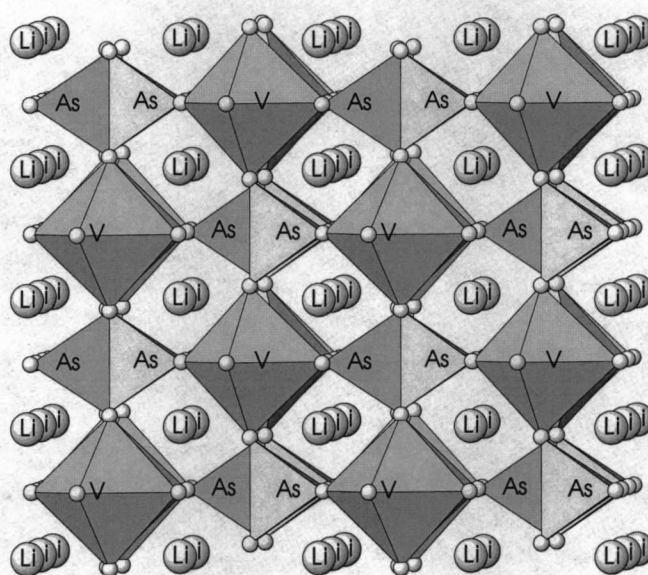


Figure 1.12. Polyhedra connectivity in LiVOAsO_4 along the bc plane.

1.2.10 Antimony Orthophosphate

Piffard et al. (101) reported the single crystal analysis of monoclinic SbOPO_4 . This compound was prepared by solid state reaction at high temperatures with $(\text{NH}_4)\text{H}_2\text{PO}_4$ and $\text{Sb}_2\text{O}_5 \cdot n\text{H}_2\text{O}$. The structure is isomorphous with the $\beta\text{-NbOAsO}_4$ compound and cell dimensions are listed in Table 1.1. Solid state ^{31}P NMR studies were done on different antimony phosphates in 1988 (102).

This study related the chemical shift anisotropy and the dimensionality of the solid network, for three-dimensional lattices. They found that water intercalation revealed NMR shifts concurrent with protonation of some of the PO_4^{3-} groups. Infrared absorption and Raman diffusion measurements were completed in order to assess the structural features of the compound (103).

Layered $\text{HSb}(\text{PO}_4)_2 \cdot x\text{H}_2\text{O}$ compounds have been prepared by an ion-exchange process (104). Titration data suggest that this compound exhibits ion-exchange behavior with Li^+ and NH_4^+ ions. In addition to these compounds, transition metal and lanthanide ions have been introduced by ion exchange.

1.2.11 VOSO_4 and VOMoO_4

The V^{4+} cation can also adopt the octahedral site within the AOMO_4 family as seen in VOSO_4 and VOMoO_4 . For charge balance to occur, the resulting M ions, S and Mo, are 6+ cations.

Vanadium orthosulfate crystallizes in an orthorhombic and a tetragonal form. Kierkegaard and Longo refined the crystal structure of $\beta\text{-VOSO}_4$ (105, 106). They found that it was orthorhombic and built up of corner-shared VO_6 octahedra and SO_4 tetrahedra. This structure is isomorphous with $\beta\text{-NbOAsO}_4$. The distorted VO_6 octahedra are linked together by sharing opposite vertices. Along the chains a bridging sulfate group connects adjacent VO_6 octahedra.

Li^+ insertion into the $\beta\text{-VOSO}_4$ structure has been investigated (107). Galvanistic cycling indicates that this process is partly reversible.

Longo and Arnott studied a sample of α -VOSO₄ by powder X-ray diffraction (108). They determined a tetragonal cell and concluded that the structure was isomorphous with tetragonal MoOPO₄ (58). This compound exhibits an octahedral distortion, similar to the isomorphous tetragonal phase previously described. The vanadium cation is displaced from the centers of the octahedra to form one short and one elongated V-O bond. The *a* and *c* cell edges were also determined at 400 °C. Both increased relative to the room temperature cell dimensions, however no further structural information was reported at this higher temperature.

Intercalation studies of this compound include the insertion of various carboxylic acids such as formic, acetic, propionic and butyric acids (109), alcohols (110, 111), acetone hydrazones (112) and amines (113). These can be formed by exchange reactions with the hydrated VOSO₄ compounds.

Single crystal refinement was reported for the VOMoO₄ phase in 1966 (114). Crystals were prepared by sealing mixtures of V₂O₃, V₂O₅, and MoO₃ (V:Mo:O ratio of 1:1:5) into evacuated platinum tubes and heated at 900 °C for three days. This structure is isomorphous with tetragonal NbOPO₄ (20), TaOPO₄ (42), MoOPO₄ (58), and α -VOSO₄ (108).

Magnetic studies (115) as a function of temperature indicate that VOMoO₄ is a 1D antiferromagnet. The cell dimensions were determined over a temperature range of 5 to 300 K. The cell edges decreased with decreasing temperature between 300 and 100 K. The *a* cell edge exhibited negative thermal expansion from 100 to 30 K and then went positive again, indicating a phase transition. At

34 K, the susceptibility changed dramatically, followed by a ferromagnetic hump at lower temperature (116), suggesting a magnetic phase transition.

West et al. studied the intercalation of Li^+ into this structure (116). VOMoO_4 can cycle approximately 1.7 Li per formula unit.

The compounds in the AOMO_4 family present framework structures that have many interesting features and have potential in a variety of applications. This thesis work is an investigation of the unique thermal expansion properties of some of these oxides. Structure relationships have been examined as a function of temperature. One aim of this research is to gain a better understanding of negative thermal expansion that will help further the advancement of applications for these materials.

1.3. References

1. Rustum Roy, D. K. Agrawal and H. A. McKinstry, *Annu. Rev. Mater. Sci.*, 19, 59 (1989)
2. Helen D. Megaw, *Mat. Res. Bull.*, 6, 1007 (1971)
3. Harold T. Smyth, *AIP Conf. Proc.*, 3, 244 (1972)
4. A. W. Sleight, *Inorg. Chem.*, 37, 2854 (1998)
5. V. Korthius, N. Khosrovani, A. W. Sleight, N. Roberts, R. Dupree and W. W. Wareen Jr., *Chem. Mater.*, 7, 412 (1995)
6. N. Khosrovani and A. W. Sleight, *J. Solid State Chem.*, 132, 355 (1997)
7. J. S. O. Evans, T. A. Mary and A. W. Sleight, *J. Solid State Chem.*, 133, 580 (1997)
8. J. S. O. Evans, T. A. Mary and A. W. Sleight, *J. Solid State Chem.*, 137, 148 (1998)

9. P. M. Forster and A. W. Sleight, *Inter. J. Inorg. Mater.*, 1, 123 (1999)
10. P. M. Forster, A. Yokochi and A. W. Sleight, *J. Solid State Chem.*, 140(1), 157 (1998)
11. John S. O. Evans and T. A. Mary, *Inter. J. Inorg. Mater.*, 2, 143 (2000)
12. T. A. Mary, J. S. O. Evans, A. W. Sleight and T. Vogt, *Science*, 272, 90 (1996)
13. J. S. O. Evans, T. A. Mary, T. Vogt, M. A. Subramanian and A. W. Sleight, *Chem. Mater.*, 8, 2809 (1996)
14. N. Khosrovnabi and A. W. Sleight, *J. Solid State Chem.*, 121, 2 (1996)
15. M. T. Dove, V. Heine and K. D. Hammonds, *Mineral. Magn.*, 59, 629 (1995)
16. Andrew P. Giddy, Martin T. Dove, G. Stuart Pawley and Volker Heine, *Acta Cryst.*, A49, 697 (1993)
17. Kenton D. Hammonds, Martin T. Dove, Andrew P. Giddy and Volker Heine, *Am. Mineral.*, 79, 1207 (1994)
18. Richard B. Hahn, *J. Am. Chem. Soc.* 73, 5091 (1951)
19. S. Z. Haider, *Proc. Pakis. Acad. Sci.*, 1, 19 (1964)
20. John M. Longo and Peder Kierkegaard, *Acta Chem. Scand.*, 20, 72, (1966)
21. S. Z. Haider, *Anal. Chim. Acta*, 24, 250 (1961)
22. G. T. Stranford and R. A. Condrate Sr., *J. Solid State Chem.*, 76, 407 (1988)
23. Klara Melanova, Ludvik Benes, Vitezslav Zima and Regina Vahalova, *Chem. Mater.*, 11, 2173 (1999)
24. K. Beneke and G. Lagaly, *Inorg. Chem.*, 22, 1503 (1983)
25. Ludvik Benes, Klara Melanova and Vitezslav Zima, *J. Solid State Chem.*, 151, 255 (2000)
26. Ludvik Benes, Klara Melanova, Vitezslav Zima and Jiri Votinsky, *J. Solid State Chem.*, 141(1), 64 (1998)

27. Xiqu Wang, Lumei Liu, Heidi Cheng and Allan J. Jacobson, *Chem. Commun.*, 24, 2531 (1999)
28. Vitezslav Zima, Ludvik Benes and Klara Melanova, *Solid State Ionics*, 106(3,4), 285 (1998)
29. Jack W. Johnson and Allan J. Jacobson U. S. Patent 82-40356, 1984
30. Jack Wayne Johnson and Allan Joseph Jacobson, Eur. Patent EP 81-305298, 1982
31. S. Bruque, M. Martinez Lara, L. Moreno, T. Ramirez-Cardenas, J. Chaboy, M. Marziali and S. Stizza, *J. Solid State Chem.*, 114(2), 317 (1995)
32. N. Kumagai, N. Ikenoya, I. Ishiyama and K. Tanno, *Solid State Ionics*, 28, 862 (1988)
33. A. L. Garcia-Ponce, L. Moreno-Real and A. Jimenez-Lopez, *Inorg. Chem.*, 27 (19), 3372 (1988)
34. S. Arsalane, R. Brochu, J. Chassaing and M. Quarton, *J. Chim. Phys. Phys.-Chim. Biol.*, 88(10), 1951 (1991)
35. Ikuya Mastuura, Tomohiro Ishimura, Satoko Hayakawa and Naomasa Kimura, *Catal. Today*, 28(1,2), 133 (1996)
36. Anil Wali, S. Unnikrishnan, S. Pillai and S. Satish, *Indian J. Chem. Technol.*, 5(3), 172 (1998)
37. Ernest M. Levin and Robert S. Roth, *J. Solid State Chem.*, 2, 250 (1970)
38. Stranford, G. T. and Condrate Sr., R. A., *J. Mat. Sci. Letters*, 3, 303 (1984)
39. A. LeClaire, H. Chahboun, D. Groult and B. Raveau, *Z. fur Krist.*, 177, 277 (1986)
40. H. Chahboun, D. Groult, M. Hervieu and B. Raveau, *J. of Solid State Chem.*, 65, 331 (1986)
41. G. T. Stranford and R. A. Condrate, Sr., *J. Solid State Chem.*, 85, 326 (1990)
42. J. M. Longo, J.W. Pierce and J. A. Kafalas, *Mat. Res. Bull.*, 6, 1157 (1971)

43. Jesse Jefferson Brown, Jr., Ph.D. Thesis, Pennsylvania State University, 1964
44. Jesse J. Brown and F. A. Hummel, *Trans. Brit. Ceram. Soc.*, 64, 419 (1965)
45. H. Chahboun, D. Groult and B. Raveau, *Mat. Res. Bull.*, 23, 805 (1988)
46. Osamu Yamaguchi, Yasumichi Mukaida and Hiroyasu Shigeta, *J. Am. Ceram. Soc.*, 72 (10), 1914 (1989)
47. C. N. Chu, N. Saka and N. P. Suh, *J. Engin. Mater. Tech.*, 108, 275 (1986)
48. Heiko Mathis, Robert Glaum and Reginald Gruehn, *Acta Chem. Scand.*, 45, 781 (1991)
49. J. L. Waring and R. S. Roth, *J. Res. Nat. Bur. Stand., Sect. A*, 69, 2, 119 (1965)
50. J. M. Amarilla, B. Casal and E. Ruiz-Hitzky, *Mat. Letters*, 8, 132 (1989)
51. Jorge Skibsted, Claus J. H. Jacobsen and Hans J. Jakobsen, *Inorg. Chem.*, 37, 3083 (1998)
52. Jose-Manuel Amarilla, Blanca Casal, Juan-Carlos Galvan and Eduardo Ruiz-Hitzky, *Chem. Mater.*, 4, 62 (1992)
53. J. M. Amarilla, B. Casal and E. Ruiz-Hitzky, *J. Mater. Chem.*, 6(6), 1005, (1996)
54. A. L. Ponce, X. Lin and J. J. Fripat, *Solid State Ionics*, 84(3,4), 213 (1996)
55. J. M. Amarilla, B. Casal and E. Ruiz-Hitzky, *J. Solid State Chem.*, 99, 258 (1992)
56. J. M. Amarilla, B. Casal, J. C. Galvan and E. Ruiz-Hitzky, *Mater. Sci. Forum*, 91-93, 153 (1992)
57. P. Kierkegaard and Margarita Westerlund, *Acta Chem. Scand.*, 18, 2217 (1964)
58. P. Kierkegaard and J. M. Longo, *Acta Chem. Scand.*, 24, 427 (1970)
59. G. T. Stranford and R. A. Condrate Sr., *J. Solid State Chem.*, 52, 248 (1984)

60. L. Lezama, K. S. Suh, G. Villeneuve and T. Rojo, *Solid State Commun.*, 7614, 449 (1990)
61. N. G. Chernorukov, N.P. Egorov, E.V. Shitova and Yu. I. Chigirinskii, *Russ. J. Inorg. Chem.*, 26 (10), 1454 (1981)
62. N. G. Chernorukov, N. P. Egorov and I. A. Korshunova, *Inorg. Mater.*, 15, 1722 (1979)
63. N. G. Chernorukov, N. P. Egorov and I. A. Korshunov, *Izv. Akad. Nauk SSSr, Neorg. Mater.*, 15(2), 335 (1979)
64. Ulutagay, M. M.S. Thesis, Clemson University, Clemson, SC, 1997
65. Mutlu Ulutagay, George L. Schimek, Shiou-Jyh Hwu and Hanna Taye, *Inorg. Chem.*, 37 (7), 1507 (1998)
66. R. Gopal and C. Calvo, *J. Solid State Chem.*, 5, 432 (1972)
67. J. M. Amarilla, B. Casal and E. Ruiz-Hitzky, *J. Solid State Chem.*, 99, 258 (1992)
68. Byron Jordan and Crispin Calvo, *Can. J. of Chem.*, 51, 2621 (1973)
69. M. Tachez, F. Theobald and E. Bordes, *J. Solid State Chem.*, 40, 280 (1981)
70. Harry Eick and Lars Kihlberg, *Acta Chem. Scand.*, 20, 722 (1966)
71. Jaroslava Kalousova, Jiri Votinsky, Ludvik Benes, Klara Melanova and Vitezslav Zima, *Collect. Czech. Chem. Commun.*, 63(1), 1 (1998)
72. Ludvik Benes, Klara Melanova, Vitezslav Zima, Jaroslava Kalousova and Jiri Votinsky, *J. Inclusion Phenom. Mol. Recognit. Chem.*, 31(3), 275 (1998)
73. Ludvik Benes and Vitezslav Zima, *Sci. Pap. Univ. Pardubice, Ser. A*, 2, 121 (1996)
74. V. Zima, L. Benes, J. Malek and M. Vlcek, *Mater. Res. Bull.*, 29, 687 (1994)
75. C. R'Kha, T. Vandenborre and J. Livage, *J. Solid State Chem.*, 63, 202 (1986)
76. K. Beneke and G. Lagaly, *Inorg. Chem.*, 22, 1503 (1983)

77. L. Benes, J. Votinsky, J. Kalousova and J. Klikorka, *Inorg. Chim. Acta*, 114, 47 (1986)
78. L. Benes, K. Melanova, V. Zima, J. Kalousova and J. Votinsky, *Inorg. Chem.*, 36, 2850 (1997)
79. L. Benes, R. Hyklova, J. Kalousova and J. Votinsky, *Inorg. Chim. Acta*, 177, 71 (1990)
80. N. Kinomura, T. Toyama and N. Kumada, *Solid State Ionics*, 78, 281 (1995)
81. L. Benes, J. Votinsky, J. Kalousova and K. Handlir, *Inorg. Chim. Acta*, 176, 255 (1990)
82. M. Martinez-Lara, L. Moreno-Real, A. Jimenez-Lopez, S. Bruque-Gamez and A. Rodriguez-Garcia, *Mater. Res. Bull.*, 21, 13 (1986)
83. V. Zima, L. Benes and K. Melanova, *Solid State Ionics*, in press
84. V. Zima, M. Vlcek, L. Benes, L. Casciola, L. Massinelli and R. Palombari, *Chem. Mater.*, 8, 2505 (1996)
85. E. Rodriguez-Castellon, A. Jimenez-Lopez, M. Martinez-Lara and L. Moreno-Real, *J. Inclusion Phenom. Mol. Recogn. Chem.*, 5, 335 (1987)
86. G. Matsubayashi and S. Ohta, *Chem. Lett.*, 787 (1990)
87. A. J. Jacobson, Intercalation Chemistry (M. S. Whittingham and A. J. Jacobson, Eds), p260. Academic Press, NY 1982
88. A. Datta, S. Bhaduri, R. Y. Kelkar and H. I. Khwaja, *J. Phys. Chem.*, 98, 11811 (1994)
89. M. Martinez-Lara, A. Jimenez-Lopez, L. Moreno-Real, S. Bruque-Gamez, B. Casal and E. Ruiz-Hitzky, *Mater. Res. Bull.*, 20, 549 (1985)
90. M. Morris, J. M. Adams and A. Dyer, *J. Mater. Chem.*, 1, 43 (1991)
91. A. J. Jacobson, J. W. Johnson, J. F. Brody, J. C. Scanlong and J. T. Lewandowski, *Inorg. Chem.*, 24, 1782 (1985)
92. V. Zima, L. Benes, J. Votinsky and J. Kalousova, *Solid State Ionics*, 82, 33 (1995)

93. R. Siskova, L. Benes, V. Zima, M. Vlcek, J. Votinsky and J. Kalousova, *Polyhedron*, 12, 181 (1993)
94. V. Zima, L. Benes, R. Siskova, P. Fatena and J. Votinsky, *Solid State Ionics*, 67, 227 (1994)
95. V. Zima, L. Benes, J. Votinsky and J. Kalousova, *Mol. Cryst. Liq. Cryst. Sci. Technol., Sect. A*, 224, 121 (1994)
96. Manuel Roca, M. Dolores Marcos, Pedro Amoros, Jaime Alamo, Aurelio Beltran-Porter and Daniel Beltran-Porter, *Inorg. Chem.*, 36, 3414 (1997)
97. N. G. Chernorukov, N.P. Egorov and I. A. Korshunov, *Zh. Neorg. Khim.*, 23, 2672 (1978)
98. M. Martinez-Lara, L. Moreno-Real, A. Jimenez Lopez, S. Gamez Bruque and A. Rodriguez Garcia, *Mater. Res. Bull.*, 21(1), 13 (1986)
99. L. Benes, J. Votinsky, J. Kalousova and K. Handlir, *Inorg. Chim. Acta*, 176, 255 (1990)
100. J. Gaubicher, F. Orsini, T. Le Mercier, S. Llorente, A. Villesuzanne, J. Angenault and M. Quarton, *J. Solid State Chem.*, 150(2), 250 (2000)
101. Y. Piffard, S. Oyetola, A. Verbaere and M. Tournoux, *J. of Solid State Chem.*, 63, 81 (1986)
102. F. Taulelle, C. Sanchez, J. Livage, A. Lachgar and Y. Piffard, *J. Phys. Chem. Solids*, 49(3), 299 (1988)
103. E. Husson, F. Genet, A. Lachgar and Y. Piffard, *J. Solid State Chem.*, 75(2), 305 (1988)
104. Y. Piffard, A. Verbaere, S. Oyetola, S. Deniard-Courant and M. Tournoux, *Eur. J. Solid State Inorg. Chem.*, 26(2), 113 (1989)
105. P. Kierkegaard, J. M. Longo, J. M. and Bengt-Olov Marinder, *Acta Chem. Scand.*, 19 (3), 763 (1965)
106. P. Kierkegaard and J. M. Longo, *Acta Chem. Scand.*, 19, 1906 (1965)
107. J. Gaubicher, Y. Chabre, J. Angenault, A. Lautie and M. Quarton, *J. Alloys Compd.*, 262, 34 (1997)

108. J. M. Longo and R. J. Arnott, *J. Solid State Chem.*, 1, 394 (1970)
109. Jiri Votinsky, Ludvik Benes, Jaroslava Kalousova and Jiri Klikorka, *Inorg. Chim. Acta*, 126(1), 19 (1987)
110. Ludvik Benes, Jiri Votinsky, Jaroslava Kalousova and Jiri Klikorka, *Inorg. Chim. Acta*, 114(1), 47 (1986)
111. Gerhard Ladwig, *Z. Chem.*, 20(2), 70 (1980)
112. Ya. S. Usmanhodzhaeva, O. F. Khodzhaev, Z. M. Musaev and N. A. Parpiev, *Uzb. Khim. Zh.*, 1, 6 (1984)
113. Mohd. Mahfooz Khan, Naseer Ahmad, A. U. Malik, *J. Inorg. Nucl. Chem.*, 31(9), 2955 (1969)
114. Harry Eick and Lars Kihlberg, *Acta Chem. Scand.*, 20, 722 (1966)
115. Ikuyo Shiozaki, *J. Phys.: Condens. Matter*, 10, 9813 (1988)
116. K. West, B. Zachau-Christiansen, S. Skaarup and T. Jacobsen, *Solid State Ionics*, 53, 356 (1992)

Chapter 2

Negative Thermal Expansion in the High Temperature Polymorph of Tetragonal NbOPO₄

2.1. Introduction

Hahn reported the preparation of tetragonal NbOPO₄ in 1951 (1). This compound was examined using X-ray diffraction, but only un-indexed diffraction lines were reported. Haider later established a tetragonal unit cell for this compound with unit cell axes of $a = 6.394 \text{ \AA}$ and $c = 4.103 \text{ \AA}$ (2). Longo and Kierkegaard determined the structure of the tetragonal phase from a crystal grown by hydrothermal technique (3). This compound crystallizes in the space group $P4/n$.

2.2. Experimental

A polycrystalline sample of tetragonal NbOPO₄ was prepared from starting materials of Nb₂O₅ (Alfa Aesar, 99.9+%) and concentrated phosphoric acid (85 %). A fivefold excess of H₃PO₄ was placed with Nb₂O₅ in a platinum crucible. This was heated at a rate of 5 °C/minute to 900 °C and maintained at this temperature for 12 hours. After cooling to room temperature at a rate of 5°C/minute, the product was washed with boiling water and then heated at 1090°C for 8 hours. A white colored product was obtained.

A differential scanning calorimetry measurement was taken with a TA Instruments Differential Scanning Calorimeter 2920. A 22 mg sample was heated in an aluminum pan under a nitrogen flow at a rate of 10 °C/minute from 20 to 550 °C.

The bulk thermal expansion was determined from a dilatometer measurement carried out using a Netzsch STA 409 system. A 25 cm × 5 cm × 5 cm pellet was heated at a rate of 5 °C/minute from room temperature to 800 °C.

X-ray powder diffraction data were obtained with an INEL diffractometer using monochromated Cu K α radiation. The sample was mounted in a capillary and diffraction patterns were obtained over the temperature range from 25 to 500°C.

Neutron powder diffraction data were collected using the BT-1 32 detector neutron powder diffractometer at the NIST Center for Neutron Research reactor. A Cu(311) monochromator with a 90 ° take-off angle, $\lambda = 1.5402(2)$ Å, and in-pile collimation of 15 minutes of arc were used. Data were collected over the range of 3-168 ° 2 θ with a step size of 0.05 °. The sample was loaded in a vanadium sample container of length 50 mm and a diameter of 15.6 mm. Diffraction measurements were collected over the temperature range from 25 to 327 °C.

2.3. Description of Structure

Tetragonal NbOPO₄ crystallizes in the space group *P4/n* (No. 85). The unit cell contains two formula units and consists of unique niobium and phosphorus atoms and two distinct oxygen atoms. Table 2.1 lists the positional parameters of tetragonal NbOPO₄ at room temperature (3). These positions are given with respect to origin choice 2 in space group *P4/n*.

Table 2.1 Atomic Coordinates for Tetragonal NbOPO₄ (3)

Atom	Wyckoff position	Site Symmetry	x	y	z
Nb	2c	4	1/4	1/4	0.7828(4)
P	2b	$\bar{4}$	1/4	3/4	1/2
O (1)	2c	4	1/4	1/4	0.2172(28)
O (2)	8g	1	0.7737(14)	0.4462(14)	0.2902(24)

Figure 2.1 shows a view of the coordination around the unit cell metal atoms. Each niobium is in octahedral coordination, while the phosphorus atoms are tetrahedrally coordinated. The connectivity of this structure involves corner-shared NbO_6 octahedra and PO_4 tetrahedra. Each NbO_6 octahedron is connected to two other octahedra in a trans configuration (on opposite corners), giving rise to chains of NbO_6 octahedra along the c axis. Phosphate tetrahedra couple these chains together and the overall connectivity results in a three-dimensional framework (Figure 2.2). One layer of polyhedra has been removed for clarity

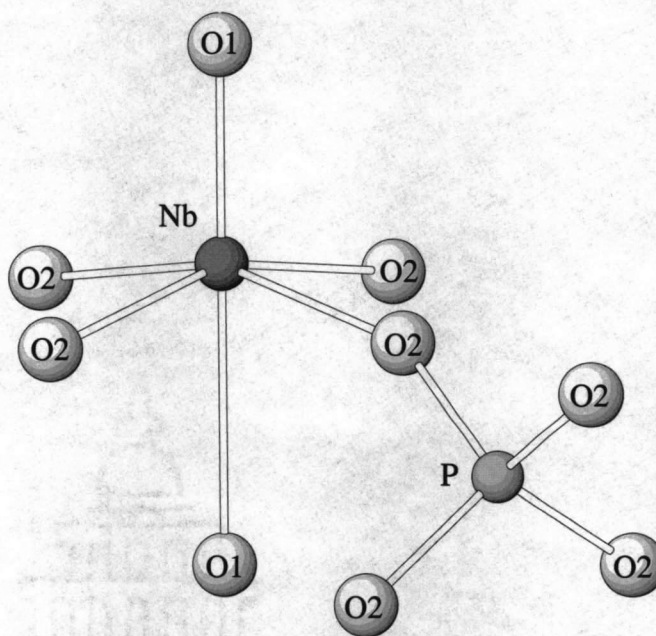


Figure 2.1. Coordination of niobium and phosphorus

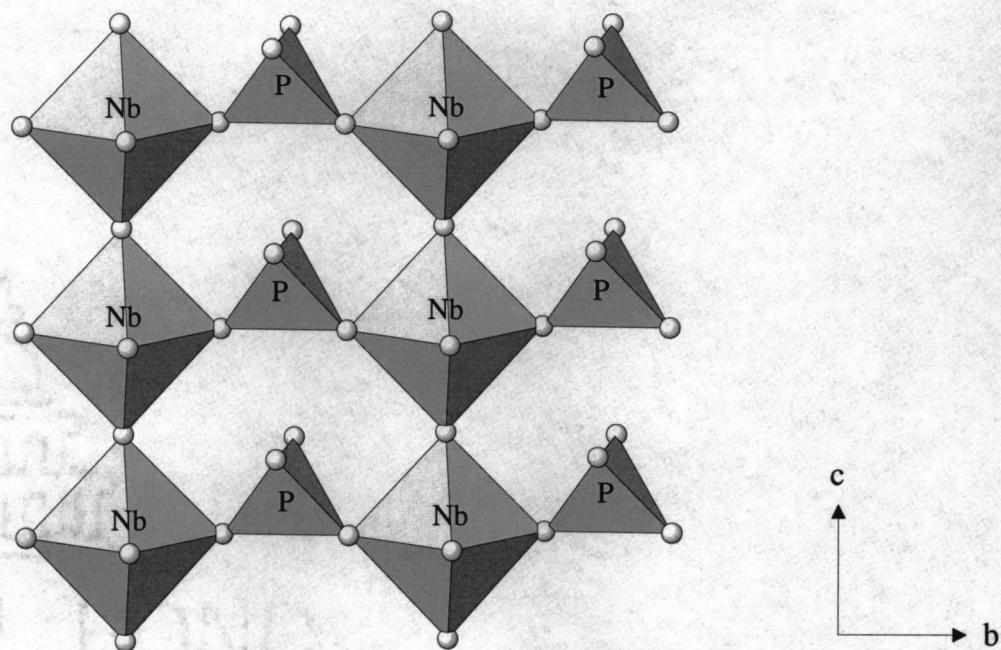


Figure 2.2. Polyhedra connectivity in tetragonal NbOPO₄

This structure contains a ferroelectric-type distortion. The niobium atom within the NbO₆ octahedron is displaced towards the apex oxygen along the *c* direction. Figure 2.3 shows the short and elongated Nb-O bond distances. This is not a true ferroelectric material because adjacent chains have opposite polarities and therefore no net polarization occurs.

2.4. Preliminary Thermal Analysis

A change in the bulk thermal expansion was observed in the dilatometer curve for the tetragonal NbOPO₄ (Figure 2.4). From room temperature up until approximately 200 °C, the relative cell expansion is positive. Above 200 °C, the bulk thermal expansion decreases as the temperature is raised.

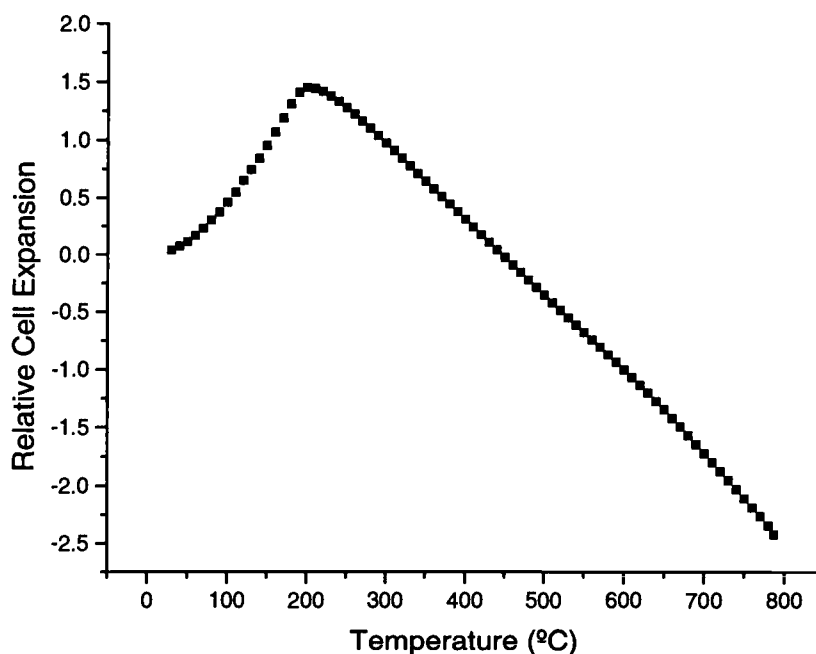


Figure 2.4. Dilatometer curve for tetragonal NbOPO₄

Differential scanning calorimetry showed no change in heat flow over this same temperature range.

2.5. Structural Refinements

Each temperature measurement was refined using the Rietveld method and GSAS software (4). For the room temperature data, initial starting parameters were taken from details reported by Longo and Kierkegaard (3). A total of 26 parameters (scale, lattice dimensions, 5 background coefficients, zero point, 5 positional parameters, and 12 anisotropic thermal factors) were refined and final agreement factors of $\chi^2 = 1.514$, $R_p = 6.65\%$, and $wR_p = 8.85\%$ were achieved. Accurate cell dimensions obtained by least squares refinement of the powder diffraction data were found to be: $a = 6.3916(2) \text{ \AA}$ and $c = 4.1047(2) \text{ \AA}$.

At temperatures greater than 25 °C, the zero point was fixed at 0.0105 degrees. A similar refinement strategy was used for each data point. Refinement statistics are given in Table 2.2.

Table 2.2. Refinement Statistics for Tetragonal NbOPO₄

Temp. (°C)	χ^2	R _p	wR _p
25	1.514	0.0665	0.0885
100	1.452	0.0658	0.0859
175	1.428	0.0681	0.0880
200	1.344	0.0646	0.0844
225	1.378	0.0652	0.0855
275	1.203	0.0725	0.0917
327	1.384	0.0657	0.0845

2.6. High Temperature Phase Transition

X-ray and neutron diffraction data analysis proves to have interesting results. The variation of the unit cell edges a and b with temperature is shown in Figure 2.5. From 25 to 200 °C the unit cell edge a increases with increasing temperature. The thermal expansion coefficient (α) for this temperature region has a value of 1.2×10^{-5} /°C. Above this temperature these cell edges decrease as the temperature increases. This suggests a phase transition close to 200 °C. The best candidate for the high temperature structure appeared to be tetragonal NbOPO₄, space group $P4/nmm$. The systematic absences ($hk0$: $h + k = 2n$, $h00$: $h = 2n$) are the same in both the $P4/n$ (No. 85) and $P4/nmm$ (No. 129) space groups. In the higher temperature structure the a and b cell edges show slightly negative thermal expansion with $\alpha = -1.0 \times 10^{-6}$ /°C. The c axis displays positive thermal expansion over the entire temperature range studied and α corresponding to this cell edge is 2.0×10^{-5} /°C (Figure 2.5). This dominates the overall bulk linear thermal expansion in the high temperature form. The α above 200 °C is 6×10^{-6} /°C. Careful examination of the structural features and their changes with temperature allowed for the identification of a reasonable mechanism for the negative thermal expansion seen in the high temperature polymorph.

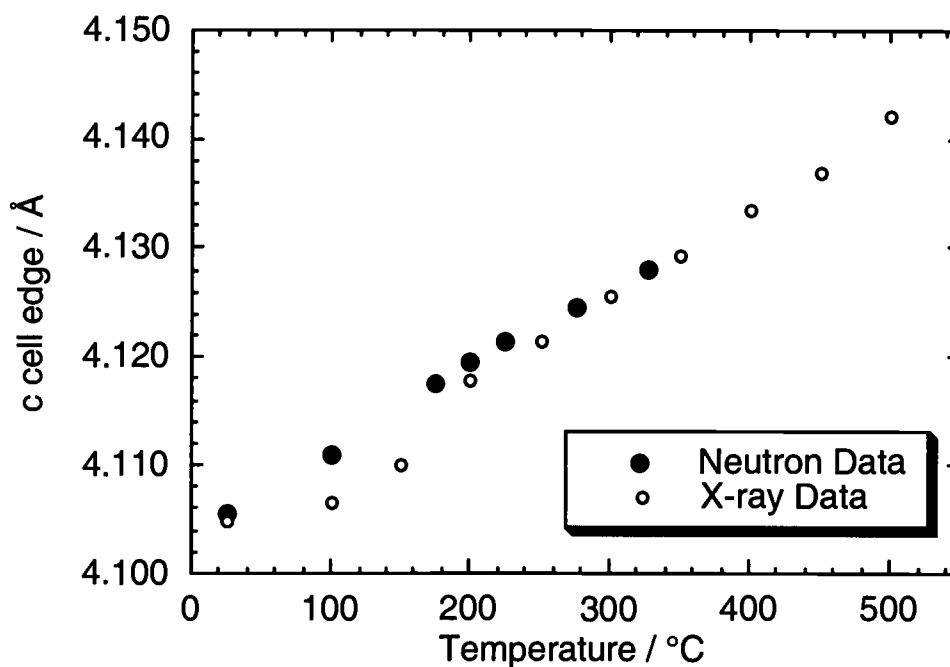
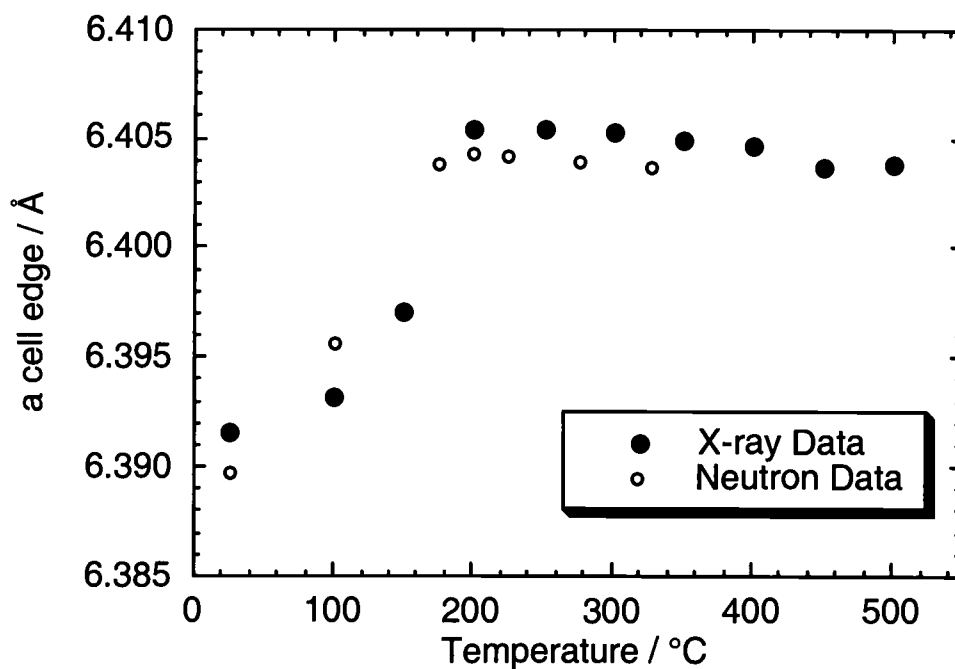


Figure 2.5. Cell dimensions a and c as a function of temperature

The atomic positional changes are listed in Table 2.3. Both $P4/n$ and $P4/nmm$ space groups have a unique phosphorus atom in a $\frac{1}{4}, \frac{3}{4}, \frac{1}{2}$ position and a niobium and an oxygen atom (O1) in a $\frac{1}{4}, \frac{1}{4}, z$ position. The oxygen atoms of the PO_4 tetrahedral group (O2) are in general xyz positions in the $P4/n$ space group and in $\frac{3}{4}, y, z$ positions in the $P4/nmm$ space group. The x parameter of the second unique oxygen (O2) converges to a value of 0.75 at higher temperatures (Figure 2.6). This particular change in atomic position causes the space group to change from $P4/n$ to $P4/nmm$. Since X-ray diffraction data lack sensitivity to a small departure of the x parameter from 0.75, neutron diffraction data were used to distinguish between the two space groups.

Table 2.3. Variation of Atomic Coordinates with Temperature

Temp.(°C)	z (O1)	x (O2)	y (O2)	z (O2)	z (Nb)
25	0.2077(4)	0.7731(2)	0.4446(1)	0.2861(2)	0.7824(3)
100	0.2058(4)	0.7694(2)	0.4443(1)	0.2866(2)	0.7818(3)
175	0.2058(4)	0.7582(2)	0.4445(1)	0.2866(2)	0.7816(3)
200	0.2048(4)	0.75	0.4445(1)	0.2869(2)	0.7815(3)
225	0.2049(4)	0.75	0.4444(1)	0.2875(2)	0.7813(3)
275	0.2036(5)	0.75	0.4446(1)	0.2877(2)	0.7819(4)
327	0.2046(5)	0.75	0.4443(1)	0.2876(2)	0.7815(4)

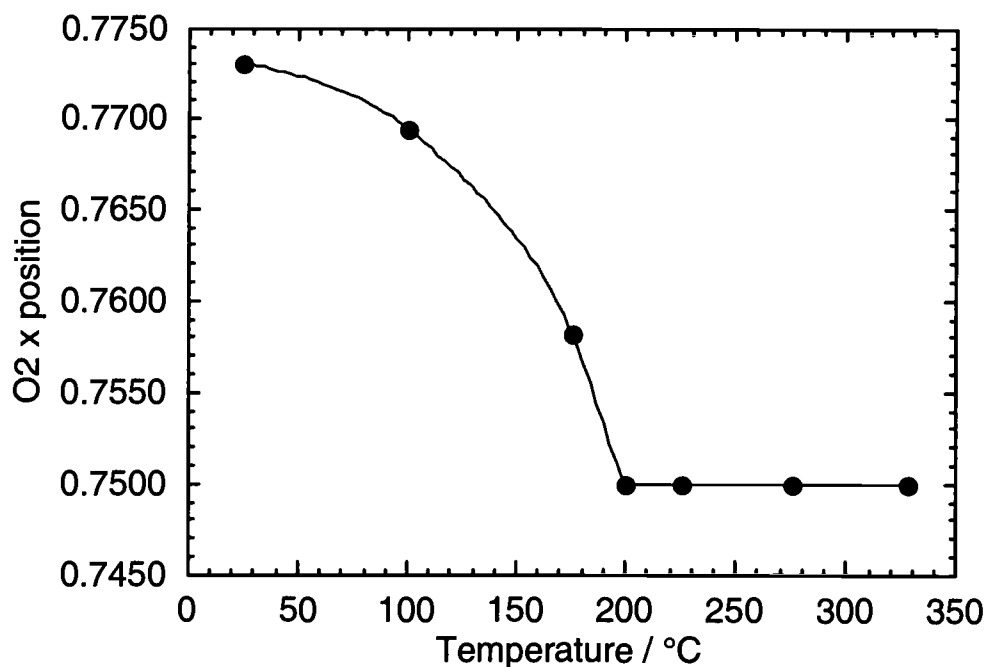


Figure 2.6. Variation of O(2) x parameter with temperature

For the temperatures between 25 and 200 °C, the final parameters were in good agreement with results from previous studies (3) with space group $P4/n$. Attempts to refine these data with $P4/nmm$ setting were unsuccessful. At higher temperatures, refinement of the additional parameter in space group $P4/n$ did not give any improvement in the fit. Therefore, results in space group $P4/nmm$ are presented for the temperatures of 200 °C and above. Figure 2.7 shows the agreement between the observed and calculated intensities for the neutron data refinements obtained at room temperature and 327 °C.

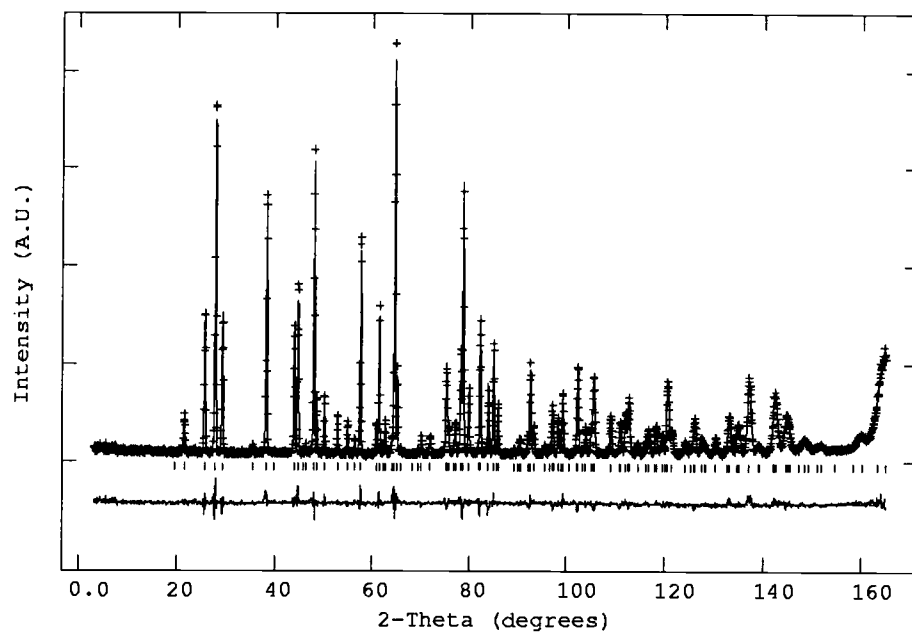


Figure 2.7.a. Observed, calculated, and difference profiles for tetragonal NbOPO₄ at 25 °C

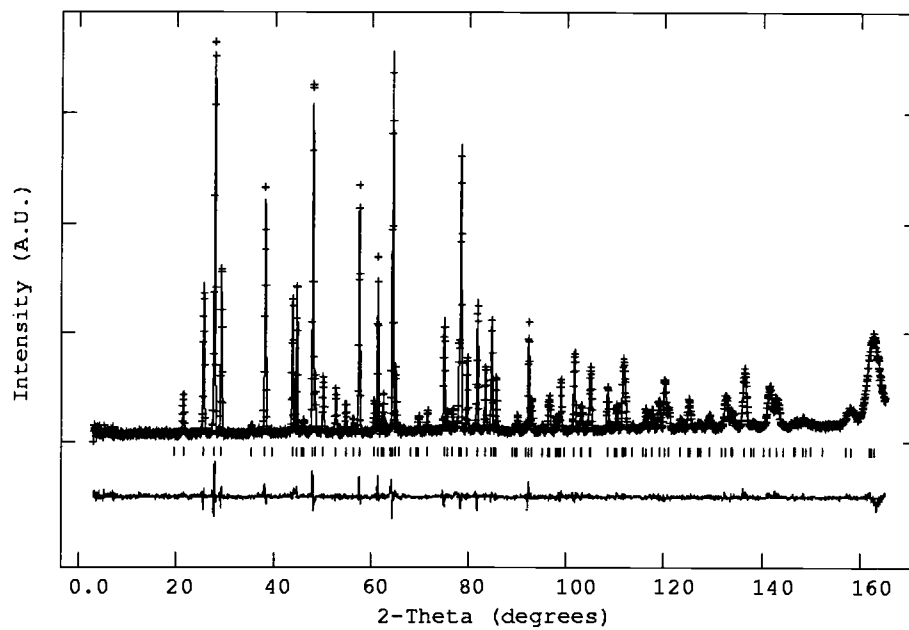


Figure 2.7.b. Observed, calculated, and difference profiles for tetragonal NbOPO₄ at 327 °C

Selected interatomic bond distances and bond angles are listed in Tables 2.4 and 2.5. There is relatively little change in the metal oxygen distances, with the exception of the long Nb-O1 bond. This bond distance increases with increasing temperature, which is consistent with the idea of weaker bonds having greater thermal expansion associated with them. The polyhedra bridging metal-oxygen-metal angle (P-O2-Nb) changes significantly in the range of 25 to 200 °C but shows little deviation from 153 ° at higher temperatures.

Table 2.4. Selected Interatomic Bond Distances (Å)

Temp (°C)	P - O2	Nb - O2	Nb - O1'	Nb - O1
25	1.5275(8)	1.9788(8)	1.746(2)	2.360 (2)
100	1.5263(8)	1.9789(8)	1.743(2)	2.368(2)
175	1.5252(9)	1.9772(9)	1.747(2)	2.371(2)
200	1.524(1)	1.977(1)	1.744(2)	2.376(2)
225	1.522(1)	1.977(1)	1.746(2)	2.376(2)
275	1.523(1)	1.976(1)	1.740(2)	2.385(2)
327	1.522(1)	1.978(1)	1.747(2)	2.382(2)

Table 2.5. Selected Bond Angles (°)

Temp (°C)	O2 - P - O2'	O2 - P - O2	O2 - Nb - O2	P - O2 - Nb
25	109.24(3)	109.93(6)	163.58(9)	151.30(7)
100	109.28(3)	109.85(6)	163.64(9)	151.78(7)
175	109.39(3)	109.64(7)	163.68(10)	152.74(8)
200	109.38(3)	109.650(1)	163.60(9)	153.03(7)
225	109.33(3)	109.746(1)	163.52(9)	153.11(7)
275	109.30(3)	109.822(1)	163.31(9)	153.26(7)
327	109.39(3)	109.640(1)	163.43(9)	153.11(7)

Figure 2.8 and 2.9 depict changes in anisotropic thermal parameters for each unique atom with temperature. The metal atoms show smaller thermal parameters consistent with being heavier than oxygen. All atoms show larger thermal parameters at higher temperatures, indicating larger atomic vibrations as the temperature is increased.

2.7. Distance Least Squares Results

The computer program Distance Least Squares (DLS) was used to determine whether the polyhedra in the tetragonal NbOPO₄ could be formed with no distortions (5). This structure can be formed with perfectly regular octahedra and tetrahedra, without an increase of lattice symmetry above the *P4/nmm* space group. Setting the niobium-oxygen bond and phosphorus-oxygen bond distances to 1.939 and 1.522 Å, respectively, in the *P4/nmm* space group, results in calculated cell dimensions of $a = 6.364$ Å and $c = 3.878$ Å. The rocking motion of these polyhedra is simulated by a change in the O2 x parameter. If this parameter is increased from 0.75 to 0.85 in the *P4/n* space group, the a cell edge decreases to a calculated value of 5.885 Å with no change in the c cell edge length. Figure 2.10 depicts the minimization of the a edge with deviations of the O2 x parameter from a value of 0.75.

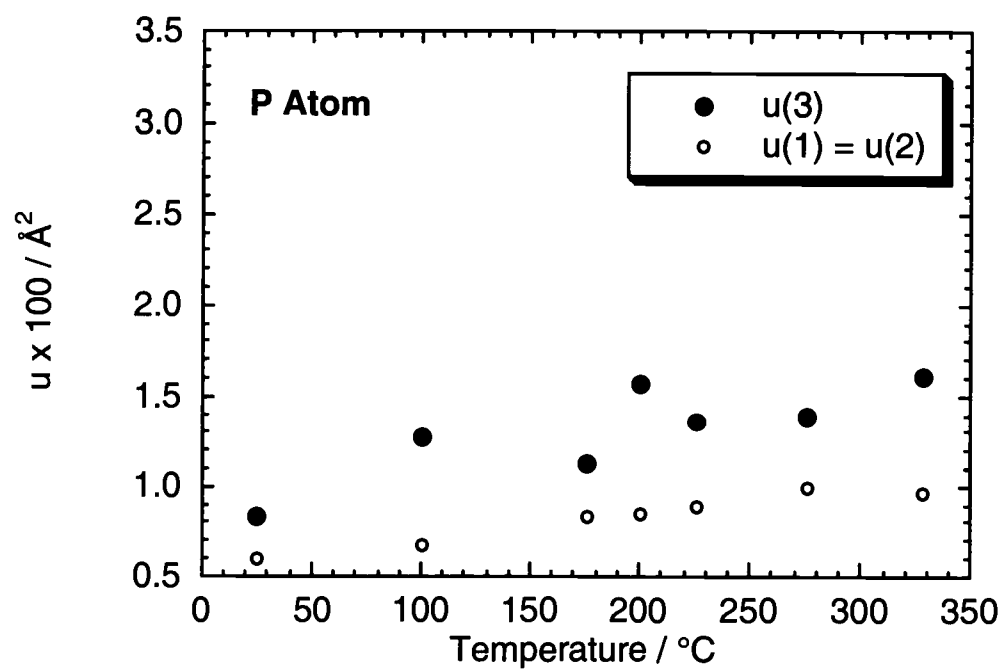
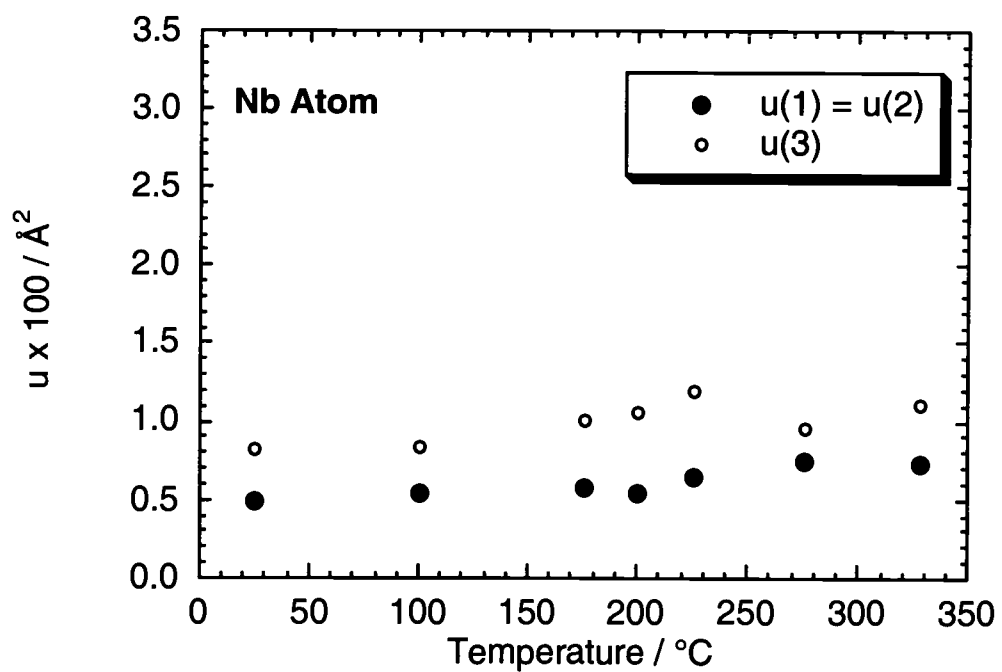


Figure 2.8 Anisotropic thermal parameters for metal atoms

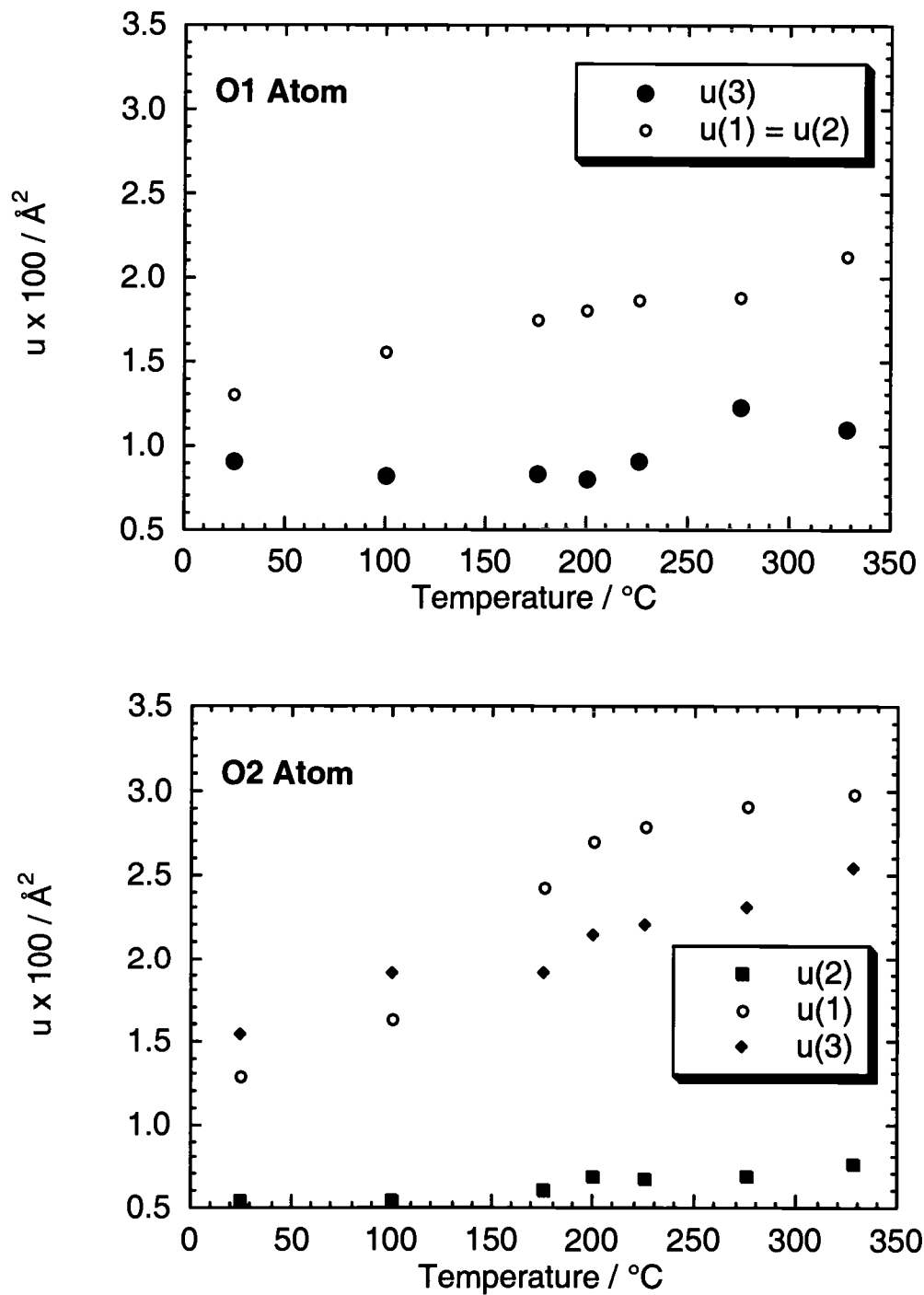


Figure 2.9 Anisotropic thermal parameters for oxygen atoms

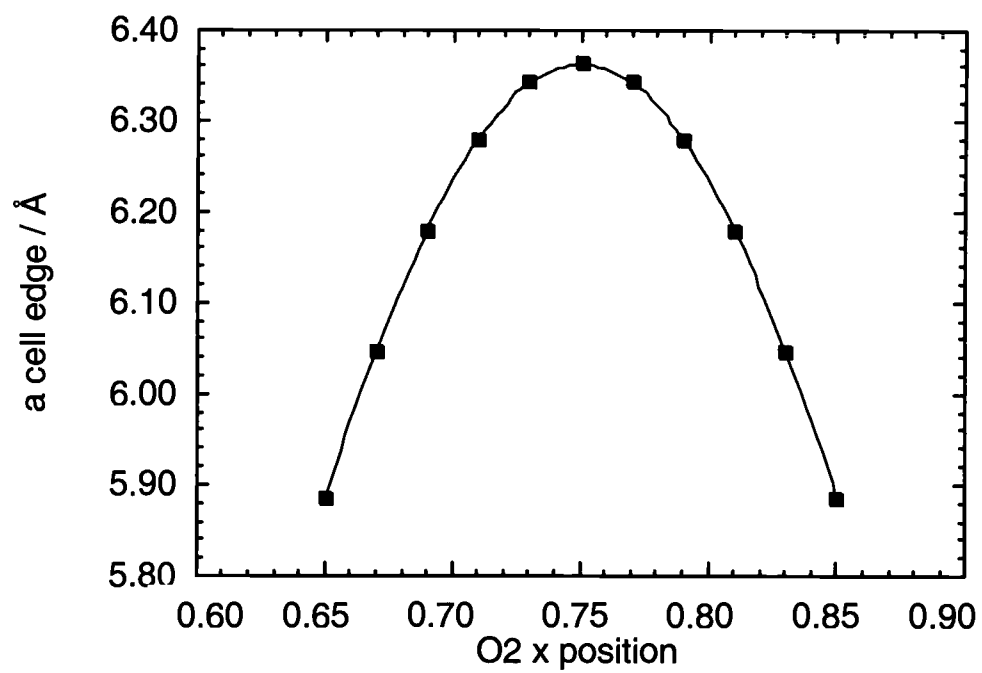


Figure 2.10. Variation of *a* cell edge with O2 *x* position

2.8. Discussion

A computational software program CRUSH (6) was used to determine possible phonon modes in this structure that leave the fundamental polyhedra undistorted. Such rigid-unit modes (RUMs) can be used to interpret the flexibility of polyhedra. These vibrational modes involve distortions of the basic structure framework but do not distort the octahedra or tetrahedra. It was found that the low temperature phase of NbOPO₄ contains one RUM, while the high temperature polymorph contains many RUMs. This corresponds to results found from DLS calculations. This structure contains polyhedra that can be perfectly regular and the tilts of the polyhedra do not result in distortion.

Tilting corner-sharing polyhedra back and forth can lead to negative thermal expansion. This mechanism is depicted in Figure 2.11. The middle structure is the tetragonal NbOPO₄ in the *P4/nmm* space group. Rocking the octahedra and tetrahedra in either direction reduces the symmetry to the *P4/n* space group. As these polyhedra tilt back and forth, the *a* and *b* cell edge lengths decrease without any change in the metal-oxygen bond distances. For this compound, the structure is locked into the lower space group at temperatures below 200 °C. As the temperature increases, this rocking motion increases. At temperatures above 200 °C, this rocking motion contributes to the overall thermal contraction of two cell edges. The length of the *c* cell edge is exactly the sum of the two Nb-O bonds along this axis. The thermal expansion of the elongated Nb-O bond length dominates the thermal expansion seen for the *c* cell edge. At room

temperature the niobium atom is displaced 0.307 \AA from the center of the octahedron towards an apex oxygen in the c -direction. At $327 \text{ }^\circ\text{C}$, this niobium is displaced 0.318 \AA from the octahedron center.

The dilatometer measurement shows negative thermal expansion associated with the temperatures above $200 \text{ }^\circ\text{C}$, where the diffraction data shows positive thermal expansion for the volume at high temperatures. This discrepancy can be explained in terms of the microstructure involved with the pelletized sample in the dilatometer measurement. Since this sample was sintered at high temperature, microcracks in the bulk pellet were introduced. As the temperature decreases, the volume of these microcracks increases. This gives rise to the thermal contraction of the bulk sample seen in the dilatometer data.

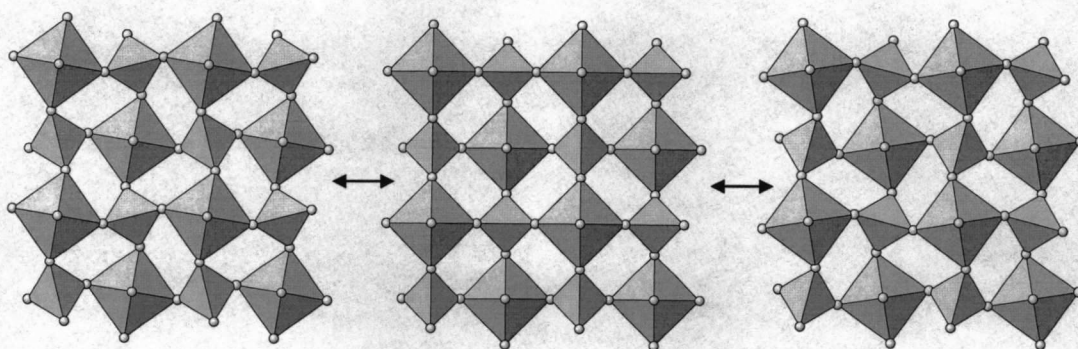


Figure 2.11. Structure of tetragonal NbOPO_4 viewed down the c axis. Central structure is in space group $P4/nmm$. The tilted structures to each side are in space group $P4/n$.

A mechanism for negative thermal expansion has been developed for the high temperature polymorph of tetragonal NbOPO_4 . This mechanism has been

acknowledged in the AM_2O_7 and $A_2M_3O_{12}$ networks (7-9). Remaining chapters in this thesis focus on identifying structural features of $AOMO_4$ compounds and their relation to their thermal expansion behavior.

2.9. References

1. Richard B. Hahn, *J. Am. Chem. Soc.* 73, 5091 (1951)
2. S. Z. Haider, *Proc. Pakis. Acad. Sci.*, 1, 19 (1964)
3. John M. Longo and Peder Kierkegaard, *Acta Chem. Scand.*, 20, 72, (1966)
4. A. C. Larson and R. B. Von Dreele, LANSCE, Los Alamos National Lab, Los Alamos, NM, 1994
5. W. M. Meier and H. Villiger, *Z. Kristallogr.*, 129, 161 (1966)
6. Kenton D. Hammonds, Martin T. Dove, Andrew P. Giddy and Volker Heine, *Am. Mineral.*, 79, 1207 (1994)
7. V. Korthius, N. Khosrovani, A. W. Sleight, N. Roberts, R. Dupree and W. W. Wareen, Jr., *Chem. Mater.* 7, 412 (1995)
8. J. S. O. Evans, T. A. Mary and A. W. Sleight, *J. Solid State Chem.*, 133, 580 (1997)
9. J. S. O. Evans, T. A. Mary and A. W. Sleight, *J. Solid State Chem.*, 137, 148 (1998)

Chapter 3

Phase Transition in Monoclinic NbOPO₄

3.1. Introduction

Monoclinic NbOPO₄ is the second polymorph of niobium orthophosphate investigated. Similar to the tetragonal NbOPO₄ compound, this structure is built up of corner-shared polyhedra, however, the linkage connectivity differs.

Levin and Roth developed a partial phase diagram for the Nb₂O₅-P₂O₅ system (1). They identified the 1:1 compound, NbPO₅, as the major phase and cell dimensions were reported. In 1986, LeClaire et al. successfully synthesized a single crystal of monoclinic NbOPO₄ (2). They established the *P2₁/c* space group and reported atomic positional parameters. The cell dimensions: $a = 13.0969(16)$ Å, $b = 5.2799(6)$ Å, $c = 13.2281(16)$ Å, and $\beta = 120.334(8)^\circ$ were calculated from indexed X-ray diffraction lines.

3.2. Experimental

A fivefold excess of phosphoric acid (85%) was placed with niobium pentoxide (Alfa Aesar, 99.9+%) in a platinum crucible. The slurry was stirred and then heated to 1300 °C at a rate of 300 °C/hour. The sample was maintained at this temperature for 90 minutes and then air quenched from the reaction

temperature. Previous experiments showed that if this sample was not quenched then a mixture of the tetragonal and monoclinic NbOPO₄ polymorphs resulted.

Differential scanning calorimetry measurements were obtained on a TA Instruments Differential Scanning Calorimeter 2920 over the temperature range of 20 to 550 °C. The sample was heated at a rate of 10 °C/minute in an aluminum pan under a flow of nitrogen gas.

Neutron powder diffraction data were collected on the BT-1 diffractometer at the Center for Neutron Research at the National Institute of Standards and Technology, using a Cu(311) monochromator with a λ of 1.5402(2) Å, and an array of 32 He-3 detectors at 5 ° intervals. The sample was loaded in a vanadium sample container of length 50 mm and a diameter of 15.6 mm. Diffraction measurements were collected at four different temperatures: 25, 200, 325, and 400 °C.

X-ray powder diffraction data were collected over the temperature range 20 to 700 °C on an INEL diffractometer with monochromated Cu K α radiation and a position sensitive detector. A small amount of ethanol was mixed with the sample and Si (NIST SRM 640b internal standard). This slurry was dropped onto the sample holder and the solvent was allowed to evaporate. This rotating holder was placed in a resistively heated furnace attachment for the temperature measurements.

3.3. Description of Structure

The monoclinic NbOPO_4 compound crystallizes in the $P2_1/c$ space group (No. 14). The connectivity of this structure consists of corner-shared NbO_6 octahedra and PO_4 tetrahedra. While this structure contains corner-shared polyhedra, the linkages are different from those found in the tetragonal NbOPO_4 compound. One NbO_6 octahedron is connected to two others in a cis configuration (on adjacent corners) that results in a zig-zag chain of alternating octahedra along the b axis (Figure 3.1).

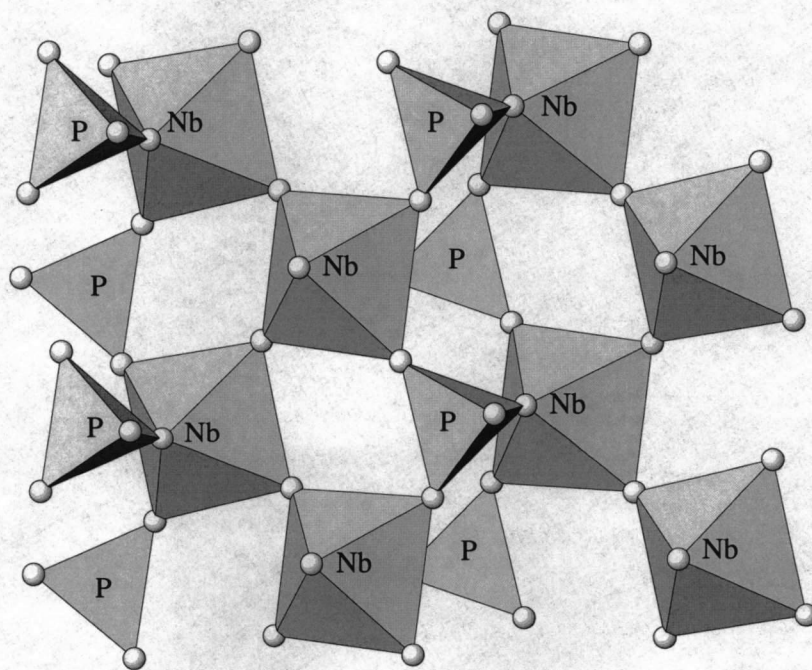


Figure 3.1. Polyhedra connectivity in monoclinic NbOPO_4 looking down the a axis

3.4. Preliminary Thermal Analysis

As one member of the AOMO_4 family, the monoclinic NbOPO_4 structure was evaluated as a candidate for displaying negative thermal expansion. Preliminary studies included the aid of differential scanning calorimetry (DSC). The DSC curve (Figure 3.2) shows a phase transition on heating with an onset temperature of approximately 292 °C. The cooling curve exhibits an onset temperature of 293 °C. Diffraction measurements were taken above and below this temperature to confirm the structural changes as a function of temperature.

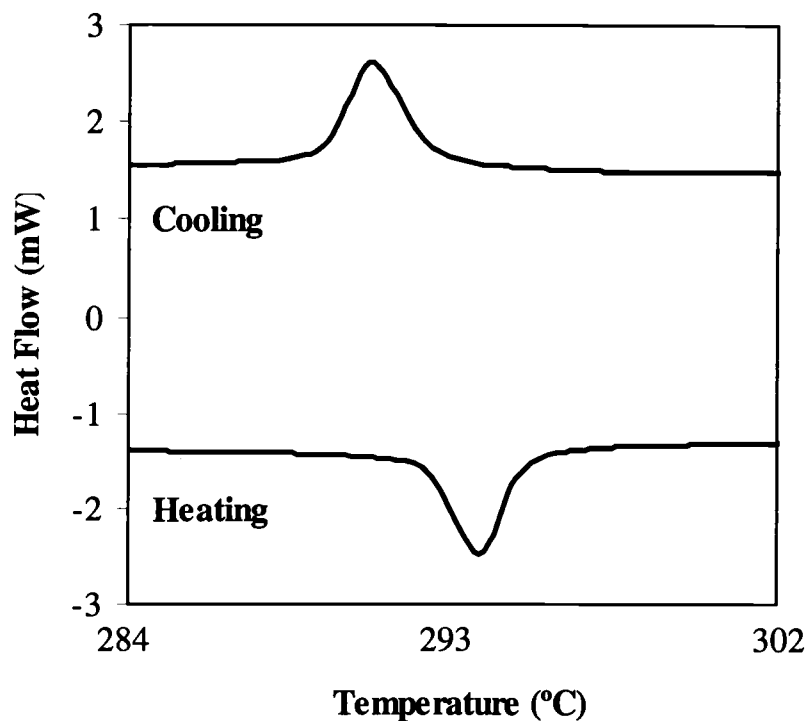


Figure 3.2. Differential scanning calorimetry plot for monoclinic NbOPO_4

3.5. Structural Refinements

All refinements were performed using GSAS software (3). A Si internal standard (NIST SRM 640b) was used to determine the accuracy of cell dimensions and to calibrate the zero point of the instrument at room temperature for the X-ray diffraction measurements. Cell dimensions and atomic positional parameters from single crystal analysis (2) were used as starting parameters in the refinements. Accurate cell dimensions and reasonable profile coefficients were determined by fitting the entire pattern using the Le Bail method (4) within the GSAS software. Rietveld refinements were then performed to elucidate background fitting, scale factor, atomic positions and thermal parameters. Soft constraints were used to limit the Nb-O and P-O distances due to the fact that large shifts in oxygen positional parameters resulted in divergence of the refinement.

A March-Dollase preferred orientation parameter was introduced into the X-ray diffraction refinements for the monoclinic NbOPO₄ phase. The preferred orientation in monoclinic NbOPO₄ patterns seems to correspond to the 010 direction. The best fit was obtained with the choice of the 010 direction leading to a March-Dollase parameter greater than 1.0, indicating in principle, needles along the *b* axis. Preferred orientation arises when there is a stronger tendency for the crystallites to be oriented more one way or one set of ways than all others. This leads to systematic distortions of the reflection intensities. Since no structural information is required to do an initial LeBail fit, it was not obvious

from the plot that a preferred orientation problem existed (Figure 3.3). However, when the Rietveld refinement was introduced, the $k = 0$ calculated intensities were remarkably different from the experimental intensities (Figure 3.4a). The difference plot was more reasonable after the March-dollase parameter was refined (Figure 3.4b).

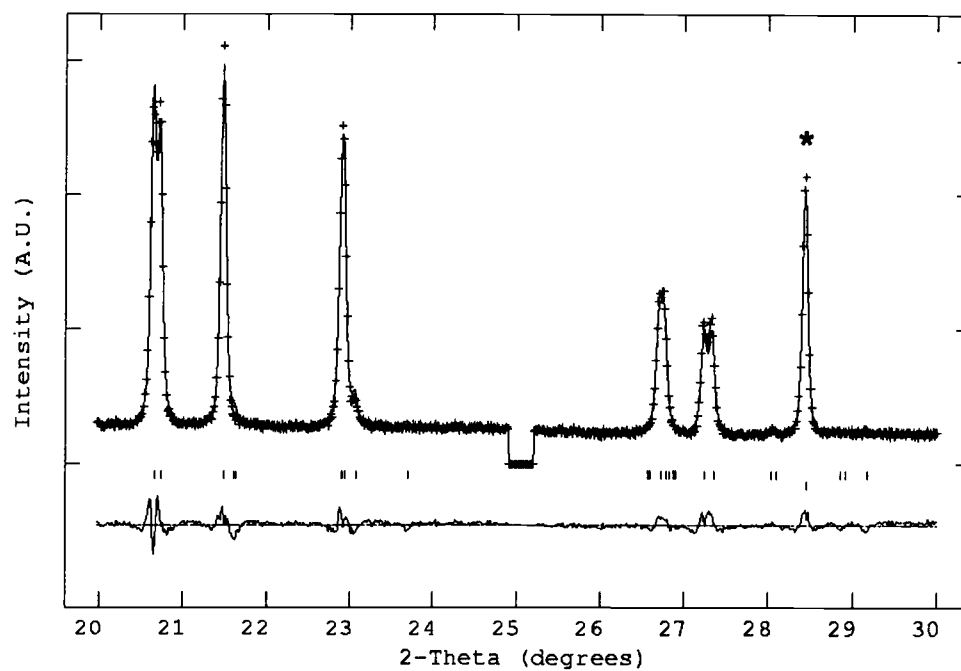


Figure 3.3. Le Bail refinement plot for monoclinic NbOPO₄ at 20 °C. The Si standard is marked with an *

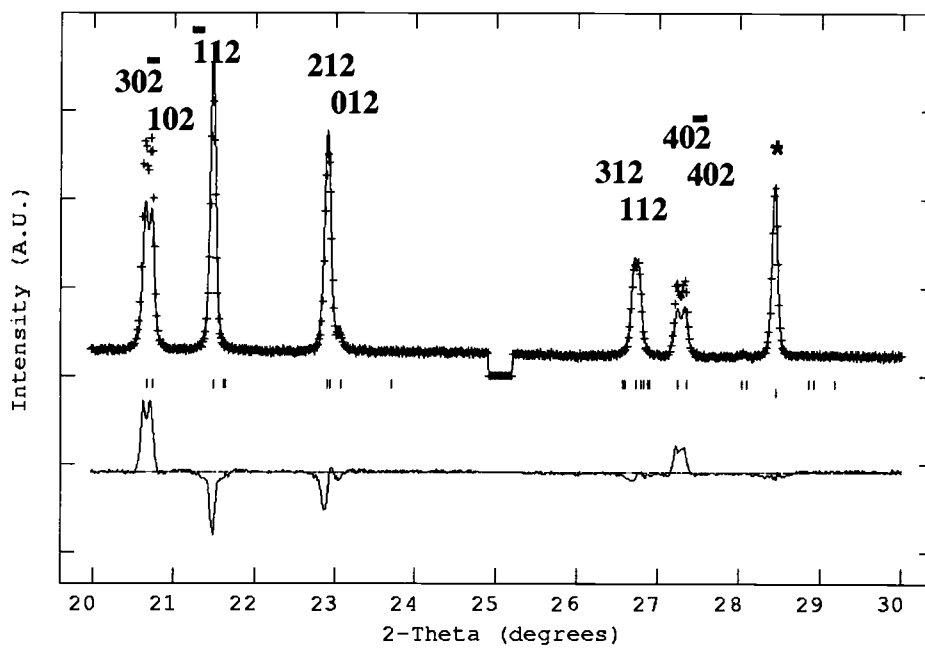


Figure 3.4.a. Rietveld refinement plot with no preferred orientation parameter refined

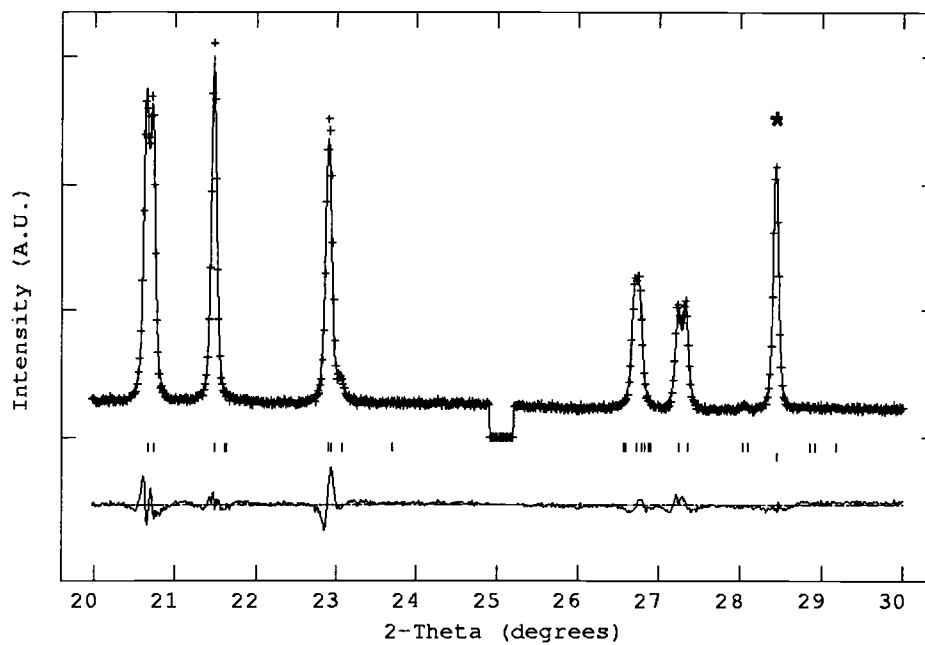


Figure 3.4.b. Rietveld refinement plot after refinement with preferred orientation parameter

At approximately 294 °C, the monoclinic NbOPO₄ structure undergoes a displacive phase transition. X-ray diffraction patterns taken above this transition temperature showed similarities to the pattern for the orthorhombic form, previously reported by Serra and Hwu (6). The monoclinic space group *P2₁/c* was used for temperature measurements between 20 and 260 °C. Above this temperature the structure could no longer be refined in the monoclinic setting and the orthorhombic setting was incorporated. The orthorhombic form crystallizes in the *Pnma* space group (No. 62). Convergence was achieved for the 325 and 400 °C temperature measurements with these settings. Refinement statistics are listed in Table 3.1. A similar refinement strategy was used for each data point. Figure 3.3 displays the final Rietveld plots for the X-ray data refinements at 20 and 340 °C, in the monoclinic and orthorhombic setting, respectively.

Table 3.1. Neutron Diffraction Refinement Statistics for NbOPO₄

Temp. (°C)	χ^2	wRp	Rp
25	2.019	0.0716	0.0561
200	1.858	0.0685	0.0543
325	2.202	0.0942	0.0749
400	1.686	0.0658	0.0528

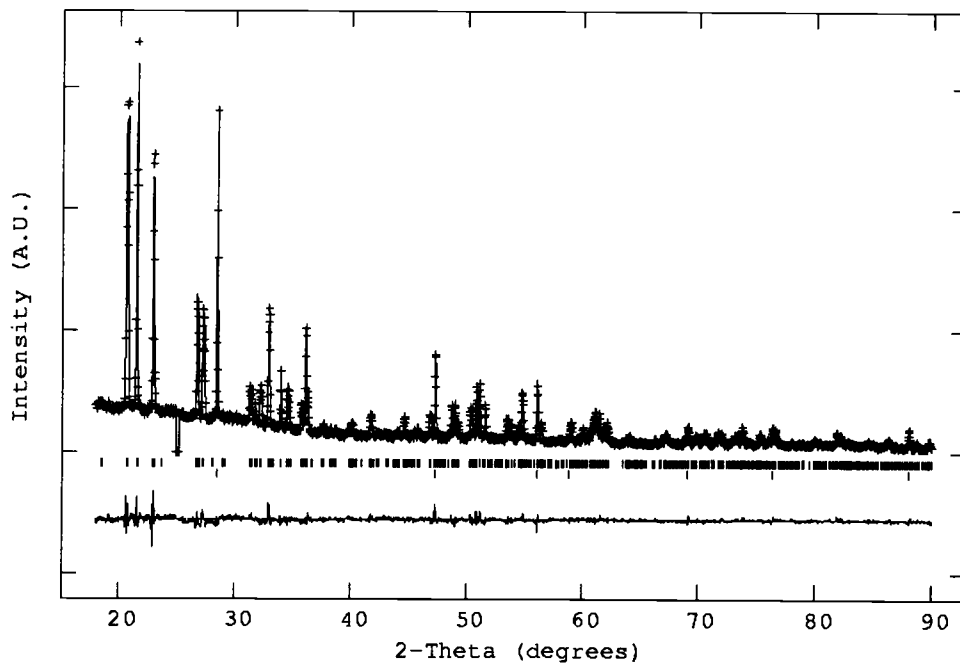


Figure 3.5.a. Observed, calculated, and difference profiles for NbOPO₄ at 25 °C

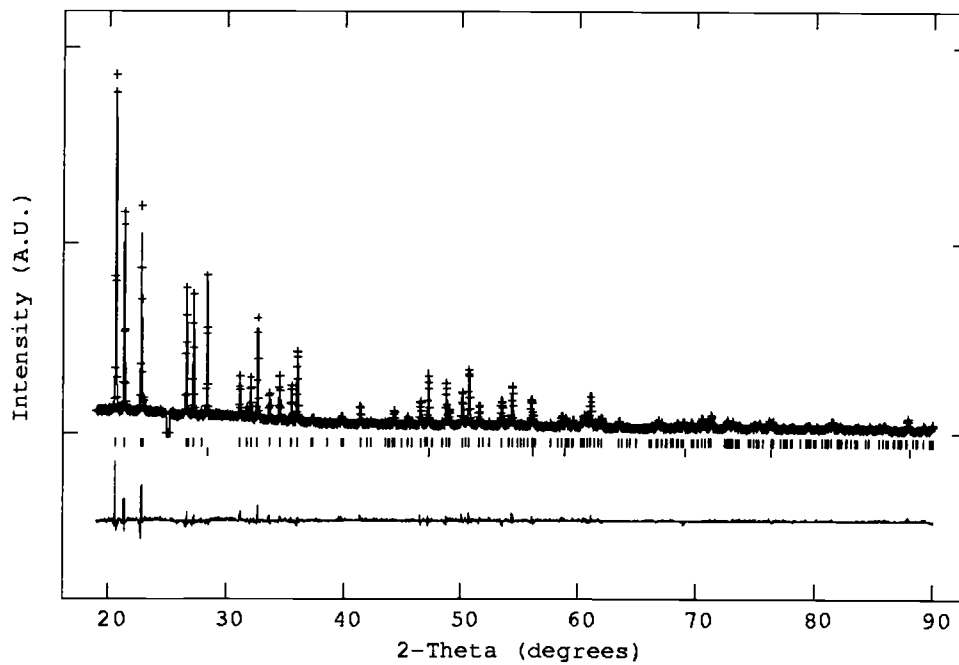


Figure 3.5.b. Observed, calculated, and difference profiles for NbOPO₄ at 340 °C

3.6. High Temperature Phase Transition

The monoclinic NbOPO₄ compound undergoes a phase transition to the orthorhombic polymorph. The orthorhombic structure is closely related to the monoclinic form. The polyhedra are less tilted in the orthorhombic form, which can be seen in the comparison of Figures 3.1 and 3.6. The monoclinic cell is related to the orthorhombic cell through the following 3 × 3 transformation matrix (o = orthorhombic, m = monoclinic):

$$\begin{pmatrix} 1 & 0 & -1 \\ 0 & -1 & 0 \\ 0 & 0 & 2 \end{pmatrix} \begin{pmatrix} a_o \\ b_o \\ c_o \end{pmatrix} = \begin{pmatrix} a_m \\ b_m \\ c_m \end{pmatrix}$$

The original cell dimensions reported by LeClaire et al. (2) ($a = 13.0969 \text{ \AA}$, $b = 5.2799 \text{ \AA}$, $c = 13.2281 \text{ \AA}$, and $\beta = 120.334^\circ$) can be converted to a standard orthorhombic setting with a β angle close to 90° using the above matrix. The resulting cell dimensions in the orthorhombic setting are $a = 11.3039 \text{ \AA}$, $b = 5.2799 \text{ \AA}$, $c = 6.6141 \text{ \AA}$, and $\beta = 90.002^\circ$. The steps involved in converting these dimensions include the following:

- i. Define cell dimensions: $a = 13.0969$, $b = 5.2799$, $c = 13.2281$, $\beta = (120.334 \times \pi/180)$
- ii. Define vectors: $\mathbf{a}_1 = (a, 0, 0)$; $\mathbf{b}_1 = (0, b, 0)$; $\mathbf{c}_1 = (c \times \cos\beta, 0, c \times \sin\beta)$
- iii. Multiply vectors \mathbf{a}_1 , \mathbf{b}_1 , and \mathbf{c}_1 by inverse of the 3 × 3 transformation matrix (since this is the conversion of monoclinic to orthorhombic) to give new vectors \mathbf{a}_2 , \mathbf{b}_2 , and \mathbf{c}_2

- iv. Determine angle between vectors \mathbf{a}_2 and \mathbf{c}_2 to find new β angle

The steps involved in converting atomic positions include the following:

- i. Transpose the 3×3 matrix
- ii. Multiply the transposed 3×3 matrix by the vector of the xyz coordinates

The Maple software program (7) was used to convert all cell dimensions and atomic positions to the orthorhombic setting.

Four neutron diffraction data sets were collected between 25 and 400 °C. These data were used to do complete structural analysis as a function of temperature. X-ray diffraction data collected over the temperature range of 20 to 700 °C were mainly used for cell dimension determination. The variation of the cell dimensions a , b , c , and β are plotted in Figures 3.7 and 3.8. The cell dimensions have been converted to the orthorhombic setting.

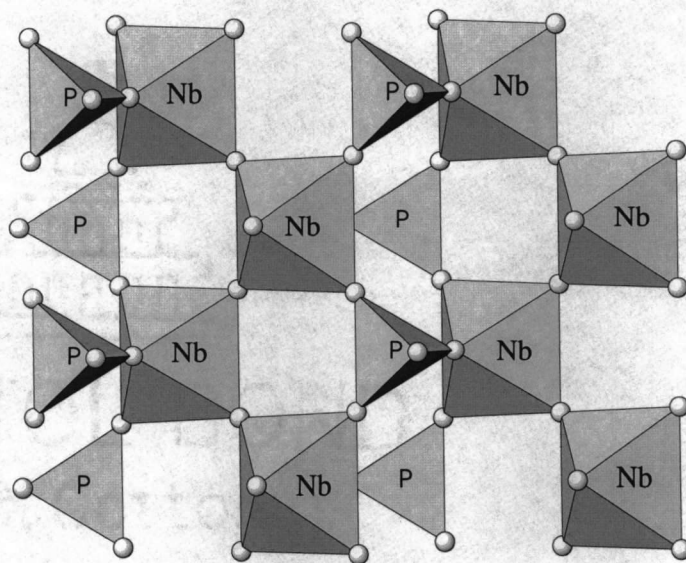


Figure 3.6. Polyhedra connectivity in orthorhombic NbOPO_4 looking down the a axis

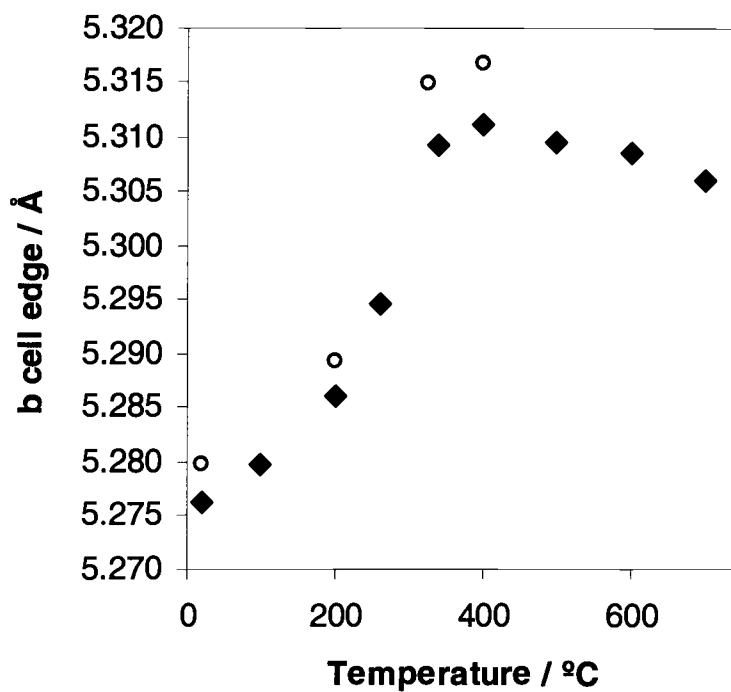
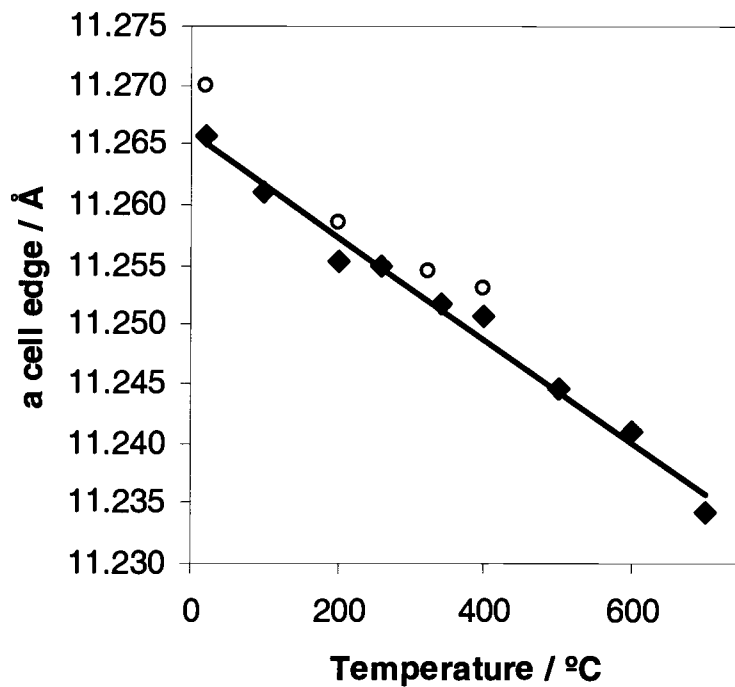


Figure 3.7. Cell dimensions *a* and *b* determined by neutron diffraction (open circles) and X-ray diffraction (closed diamonds) analysis

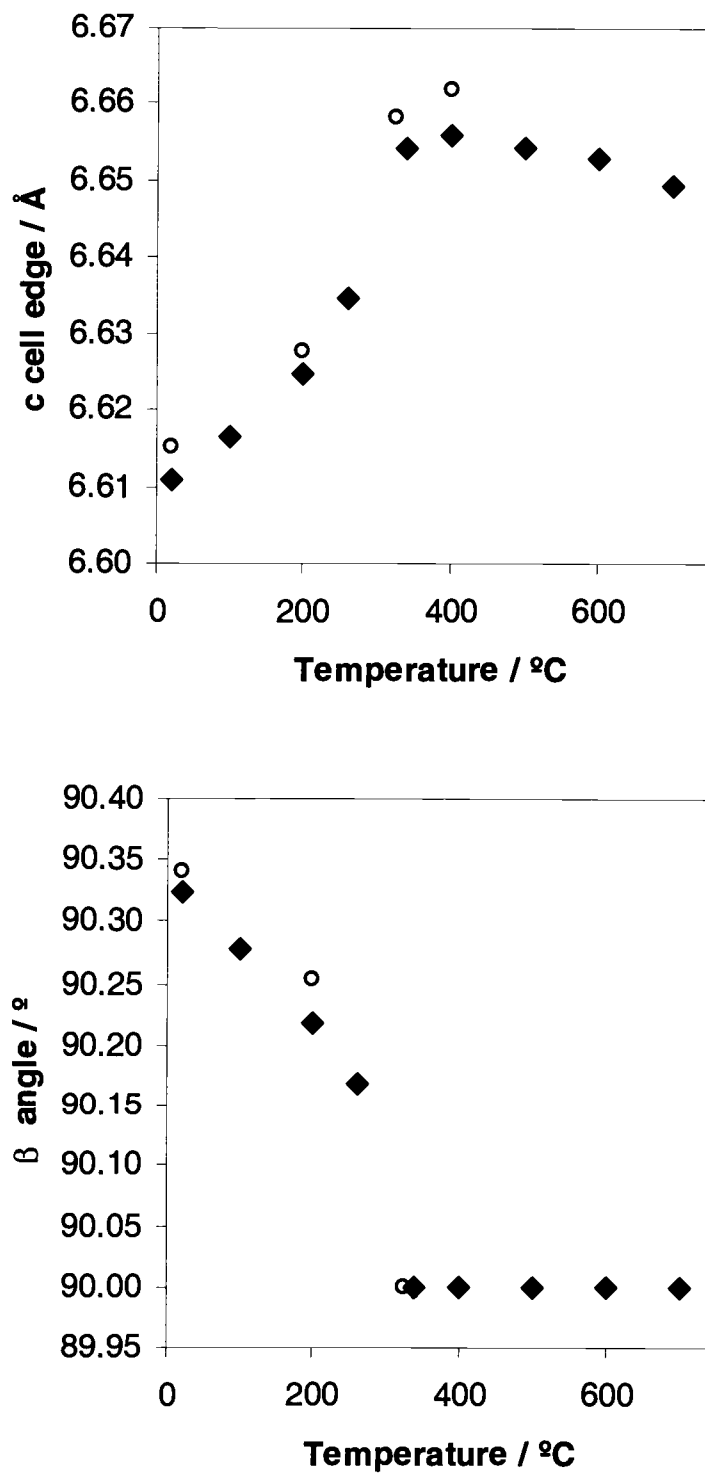


Figure 3.8. Cell dimensions c and β determined by neutron diffraction (open circles) and X-ray diffraction (closed diamonds) analysis

The b and c cell edges and the β angle clearly show a distinct change occurring around 300 °C. The a cell edge decreases over the entire temperature range studied. For the low temperature monoclinic phase both b and c cell dimensions show positive thermal expansion. Above the phase transition all cell dimensions exhibit negative thermal expansion. The volume shows a larger positive thermal expansion below the phase transition and very slight negative thermal expansion above (Figure 3.9). The thermal expansion coefficients are listed in Table 3.2.

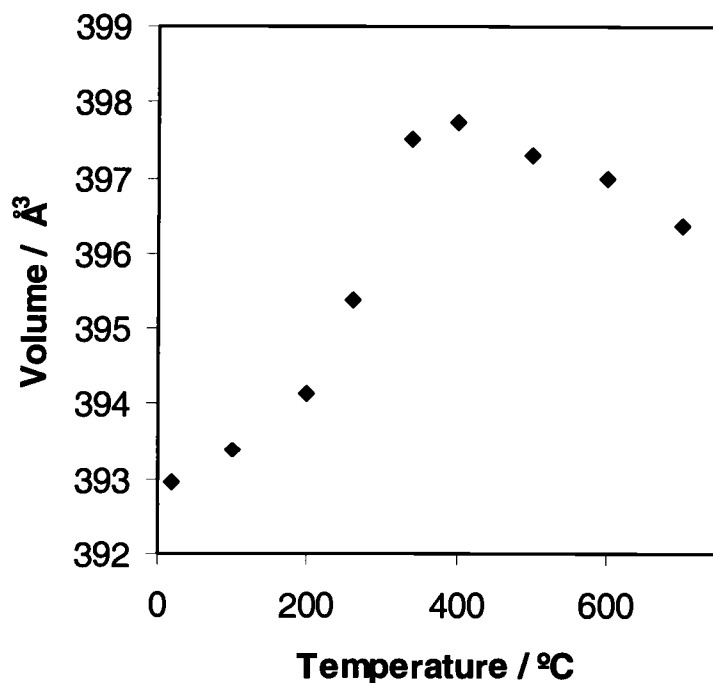


Figure 3.9. Changes in volume with temperature

Table 3.2. Thermal Expansion Coefficients for NbOPO₄

Temperature Range (°C)	Cell Dimension	α (°C ⁻¹)
20 - 340	a	-3.86×10^{-6}
	b	1.89×10^{-5}
	c	1.95×10^{-5}
20 - 340	Volume	3.46×10^{-5}
	α_v	1.15×10^{-5}
400-700	a	-4.76×10^{-6}
	b	-3.11×10^{-6}
	c	-3.13×10^{-6}
	Volume	-1.10×10^{-5}
	α_v	-3.67×10^{-6}

The atomic positional parameters for the monoclinic NbOPO₄ at 25 and 200 °C are listed in Table 3.3. There are two unique niobium and phosphorus atoms and ten oxygen atoms, all on general positions. The same atoms converted to the orthorhombic setting are listed in Table 3.4.

Table 3.3. Atomic Coordinates for Monoclinic NbOPO₄ at 25 and 200 °C

Atom	x/a	y/b	z/c
Nb (1)	0.0628(4)	0.244(1)	0.3658(3)
	0.0629(4)	0.244(1)	0.3662(4)
Nb (2)	0.5641(3)	0.246(1)	0.1985(3)
	0.5640(4)	0.248(1)	0.1985(4)
P (1)	0.3452(4)	0.257(1)	0.4079(4)
	0.3448(5)	0.259(1)	0.4093(5)
P (2)	0.1552(4)	0.770(1)	0.0637(4)
	0.1538(5)	0.765(1)	0.0632(5)
O (1)	0.2154(4)	0.242(1)	0.3708(4)
	0.2148(5)	0.239(1)	0.3708(5)
O (2)	0.9175(4)	0.234(1)	0.3752(4)
	0.9180(5)	0.239(1)	0.3757(5)
O (3)	0.0089(5)	0.5403(9)	0.2689(5)
	0.0077(6)	0.533(1)	0.2651(5)
O (4)	0.1403(5)	0.473(1)	0.5115(5)
	0.1385(5)	0.476(1)	0.5099(6)
O (5)	0.1169(5)	-0.060(1)	0.4698(5)
	0.1181(5)	-0.057(1)	0.4708(5)
O (6)	0.7139(4)	0.232(1)	0.3434(4)
	0.7147(5)	0.239(1)	0.3430(5)
O (7)	0.4189(4)	0.286(1)	0.0403(4)
	0.4178(5)	0.285(1)	0.0400(5)
O (8)	0.4978(5)	0.471(1)	0.2634(4)
	0.4964(6)	0.471(1)	0.2615(5)
O (9)	0.6279(5)	0.024(1)	0.1199(5)
	0.6284(6)	0.020(1)	0.1218(5)
O (10)	0.6279(5)	0.555(1)	0.1569(5)
	0.6283(5)	0.550(1)	0.1548(5)

Table 3.4. Atomic Coordinates for Monoclinic NbOPO₄ Converted to the Orthorhombic Setting at 25 and 200 °C

Atom	x/a	y/b	z/c
Nb (1)	0.0628 0.0629	0.244 0.244	0.6688 0.6695
Nb (2)	0.5641 0.5640	0.246 0.248	-0.1671 -0.1671
P (1)	0.3345 0.3348	0.257 0.259	0.4813 0.4838
P (2)	0.1552 0.1538	0.770 0.765	-0.0278 -0.0274
O (1)	0.2154 0.2148	0.242 0.239	0.5262 0.5268
O (2)	0.9175 0.9180	0.234 0.239	-0.1671 -0.1666
O (3)	0.0089 0.0077	0.540 0.533	0.5289 0.5225
O (4)	0.1403 0.1385	0.473 0.476	0.8827 0.8813
O (5)	0.1169 0.1181	0.940 0.943	0.8227 0.8235
O (6)	0.7139 0.7147	0.231 0.239	-0.0271 0.0287
O (7)	0.4189 0.4178	0.286 0.285	-0.3383 -0.3378
O (8)	0.4978 0.4964	0.471 0.471	0.0290 0.0266
O (9)	0.6279 0.6284	0.024 0.020	-0.3881 -0.3848
O (10)	0.6279 0.6283	0.555 0.550	-0.3141 -0.3187

When the structure transforms to the orthorhombic phase, the metal atoms and six oxygen atoms move onto mirror planes and four oxygen atoms displace slightly but remain on general positions. Table 3.5 indicates which atoms in the monoclinic setting transform to atoms in the orthorhombic setting.

Table 3.5. Atom Transformation from the Monoclinic to the Orthorhombic Setting

Monoclinic (Z = 8)			Orthorhombic (Z = 4)		
Atom(s)	Wyckoff Position	Site Symmetry	Atom	Wyckoff Position	Site Symmetry
Nb(1), Nb(2)	4e	1	Nb	4c	m
P(1), P(2)	4e	1	P	4c	<u>m</u>
O(3), O(8)	4e	1	O(1)	4a	<u>1</u>
O(2), O(7)	4e	1	O(2)	4c	m
O(4), O(5), O(9), O(10)	4e	1	O(3)	8d	1
O(1), O(6)	4e	1	O(4)	4c	m

The atomic positions of the orthorhombic form at 325 and 400 °C are listed in Table 3.6.

Table 3.6. Atomic Coordinates for Orthorhombic NbOPO₄ at 325 and 400 °C

Atom	x/a	y/b	z/c
Nb	0.4384(3)	1/4	0.3291(5)
	0.4377(2)		0.3302(4)
P	0.1539(4)	1/4	0.5285(6)
	0.1534(3)		0.5288(5)
O (1)	0	0	0
O (2)	0.0807(7)	1/4	0.3333(7)
	0.0807(3)		0.3350(5)
O (3)	0.1285(3)	0.0166(7)	0.6448(5)
	0.1278(2)	0.0162(5)	0.6462(4)
O (4)	0.2852(4)	1/4	0.4714(7)
	0.2850(3)		0.4709(5)

The displacement magnitudes are recorded in Table 3.7. The displacements correspond to how far each atom in the monoclinic structure at 25 °C has moved towards the equivalent atom in the orthorhombic structure at 325 °C. The O(3), O(8), O(4), O(5), O(9) and O(10) atoms in the monoclinic structure displace the greatest distance when the structure transforms to the orthorhombic form.

In addition to the determination of the atomic displacements for the monoclinic to the orthorhombic structure, isotropic temperature factors were evaluated in the neutron data refinements. The heavier metal atoms had smaller values compared to those found for the oxygen atoms, consistent with the fact that lighter atoms vibrate more easily with temperature. The values of these thermal parameters as a function of temperature are plotted in Figures 3.10 and 3.11. At temperatures below 300 °C, the monoclinic atoms are depicted and the orthorhombic atoms above this temperature.

Table 3.7. Displacement Distances from Each Monoclinic Atom to the Equivalent Orthorhombic Atom

Monoclinic Atom (25 °C)	Orthorhombic Atom (325 °C)	$\Delta x/\text{\AA}$	$\Delta y/\text{\AA}$	$\Delta z/\text{\AA}$	$d/\text{\AA}$
Nb(1)	Nb	-0.015	-0.030	0.009	0.035
Nb(2)		-0.027	-0.012	0.028	0.041
P(1)	P	0.015	0.039	-0.065	0.077
P(2)		0.015	0.106	-0.005	0.107
O(3)	O(1)	0.100	0.213	0.191	0.303
O(8)		0.025	0.153	0.192	0.247
O(2)	O(2)	0.020	0.087	0.000	0.089
O(7)		0.005	-0.188	0.033	0.191
O(4)	O(3)	0.133	0.231	0.215	0.342
O(5)		-0.131	0.057	-0.182	0.231
O(9)		-0.007	0.041	-0.218	0.222
O(10)		-0.007	0.204	0.272	0.340
O(1)	O(4)	-0.007	-0.041	0.016	0.045
O(8)		0.010	-0.098	0.010	0.099

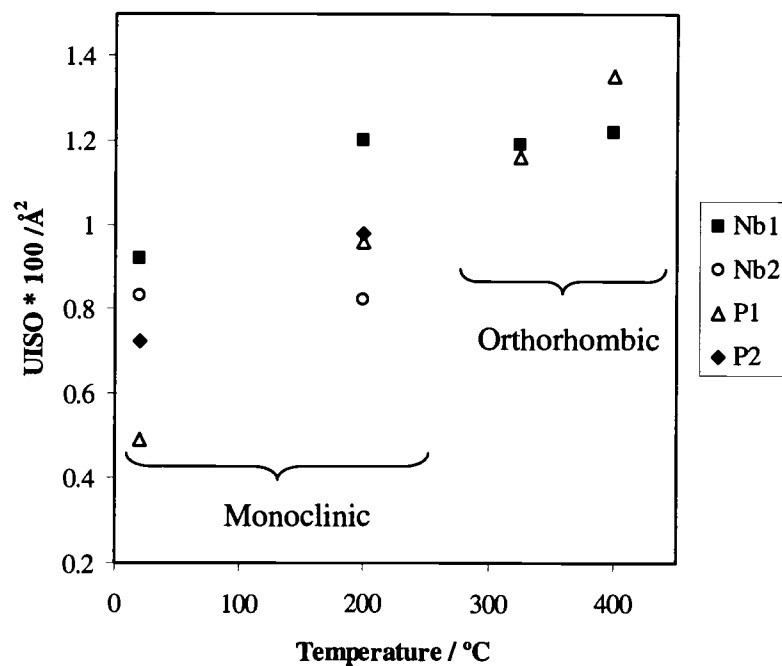


Figure 3.10. Isotropic thermal parameters for niobium and phosphorus atoms

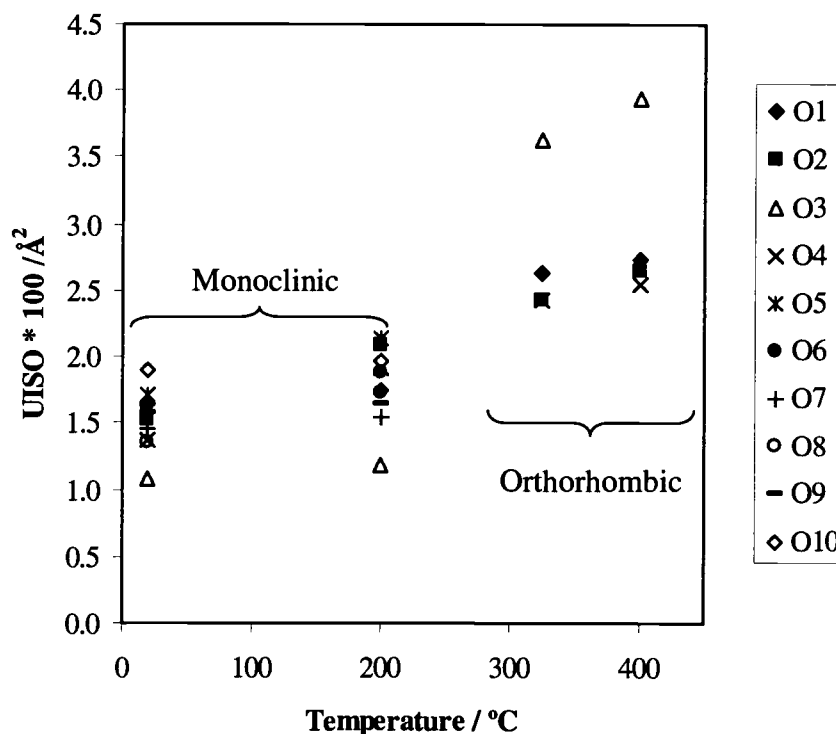


Figure 3.11. Isotropic thermal parameters for oxygen atoms

The largest thermal parameter is that of the O(3) in the orthorhombic structure and is also the atom that has moved the greatest distance from that in the monoclinic structure (Table 3.7). The O(1) moves also moves significantly, however, it has a slightly smaller thermal displacement factor. The refinement of anisotropic thermal parameters was also introduced. A partial view of the orthorhombic structure with anisotropic thermal parameters is shown in Figure 3.12. This emphasizes the difference seen in the metal and oxygen thermal movements as well as the exaggerated movement of the O(3) compared to the other oxygen atoms in the structure.

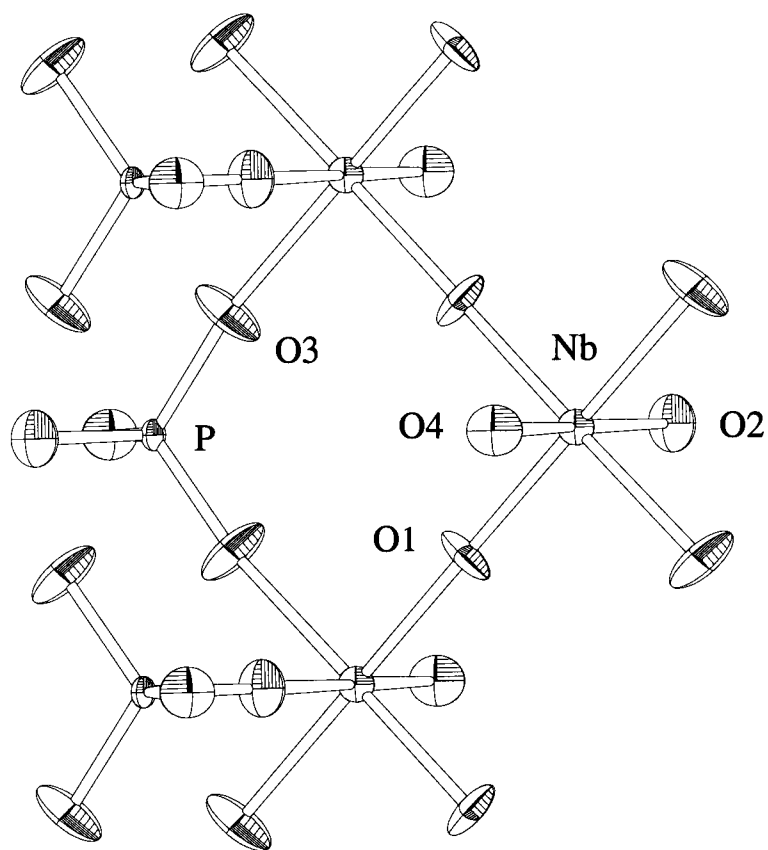


Figure 3.12. Partial view of the anisotropic thermal parameters in the orthorhombic NbOPO₄ structure looking down the *a* axis.

This view of the connectivity becomes significant in the discussion of the facile motion of polyhedra.

The NbO₆ octahedra in the monoclinic structure are somewhat distorted. This is related to the connectivity of each polyhedron. One NbO₆ octahedron is connected to two different octahedra and four phosphate tetrahedra. The phosphate tetrahedra are more covalent which results in stronger P-O bonds. The

shortened Nb-O(1) bond represents the Nb-O bond that bridges another NbO₆ octahedron. These distances are found in Tables 3.8 and 3.9.

Table 3.8. Selected Bond Distances for 25 and 200 °C Data

Nb1 - O1	Nb1 - O2	Nb1 - O3	Nb1 - O3	Nb1 - O4	Nb1 - O5
1.967(6)	1.971(6)	1.914(7)	1.873(7)	2.049(7)	1.997(8)
1.959(7)	1.966(7)	1.914(8)	1.868(8)	2.045(9)	1.992(10)
Nb2 - O6	Nb2 - O7	Nb2 - O8	Nb2 - O8	Nb2 - O9	Nb2 - O10
1.923(6)	1.995(6)	1.915(8)	1.854(8)	2.008(7)	2.034(8)
1.926(7)	2.004(7)	1.904(8)	1.867(8)	2.018(9)	2.023(10)
P1 - O1	P1 - O7	P1 - O9	P1 - O10		
1.512(6)	1.525(7)	1.543(8)	1.519(8)		
1.540(8)	1.541(8)	1.531(9)	1.527(8)		
P2 - O2	P2 - O4	P2 - O5	P2 - O6		
1.543(6)	1.492(8)	1.544(8)	1.530(6)		
1.543(8)	1.539(9)	1.546(8)	1.513(8)		

Table 3.9. Selected Bond Distances for 325 and 400 °C Data

[2] Nb - O1	Nb - O2	[2] Nb - O3	Nb - O4
1.882(2)	1.934(6)	2.020(4)	1.968(6)
1.881(2)	1.950(4)	2.012(3)	1.958(4)
P - O2	[2] P - O3	P - O4	
1.539(6)	1.490(4)	1.526(6)	
1.529(5)	1.497(3)	1.531(4)	

Table 3.10 lists the anisotropic thermal parameters that were determined for temperatures above 200 °C. These parameters are with respect to the arbitrary directions determined by the ellipsoids, not with respect to the crystallographic axes. Busing and Levy developed a correction for bond lengths based on the thermal motion of atoms derived from diffraction measurements (8). An estimation of the corrected distance, R_{corr} , is given by the formula:

$$R_{corr} = R + (w_a - w_b)/(2R)$$

where R is the distance between two atoms found from diffraction measurements and w represents the thermal motion parameter for each atom. This correction was applied for each distance found in the 325 and 400 °C data sets. Corrected distances are listed in Table 3.11.

Table 3.10. Refined Anisotropic Thermal Parameters (\AA^2) for 325 °C and 400 °C Data

Atom	100*U11	100*U22	100*U33
Nb	0.742(113)	1.481(149)	1.503(143)
	0.967(89)	1.503(100)	1.426(104)
P	1.565(192)	1.182(191)	0.557(176)
	1.611(131)	1.153(131)	1.178(138)
O1	2.338(218)	5.325(292)	0.700(180)
	2.779(159)	5.086(187)	0.792(120)
O2	1.143(230)	3.799(265)	3.385(267)
	0.966(153)	4.004(176)	3.812(192)
O3	4.013(184)	0.791(143)	7.348(286)
	4.504(132)	1.109(101)	7.147(186)
O4	1.370(179)	2.965(225)	3.681(260)
	1.466(127)	3.446(161)	3.384(171)

Table 3.11. Corrected Bond Distances for 325 and 400 °C Data

[2] Nb - O1	Nb - O2	[2] Nb - O3	Nb - O4	Avg.
1.888	1.958	2.028	1.970	1.960
1.888	1.973	2.018	1.960	1.958
	↑ 0.77%	↓ 0.49%	↓ 0.51%	↓ 0.10%
P - O2	[2] P - O3	P - O4	Avg.	
1.535	1.515	1.516	1.520	
1.523	1.522	1.525	1.523	
↓ 0.78%	↑ 0.46%	↑ 0.59%	↑ 0.20%	

The arrows represent the increase or decrease in bond length from 325 °C to 400 °C and the corresponding % change. Surprisingly, the long Nb-O bond does not get larger at higher temperatures. These bond distances are gradually going towards more equalized distances as the temperature increases.

Figure 3.13 shows a slice of the *bc* plane for both structures. The intra-polyhedral angles are denoted in the monoclinic form with A' – D'. The most remarkable angle change that demonstrates the tilting angles of the polyhedra is shown in Figure 3.14. The monoclinic structure has very skewed angles in this representation, while the orthorhombic form has angles close to 90 °.

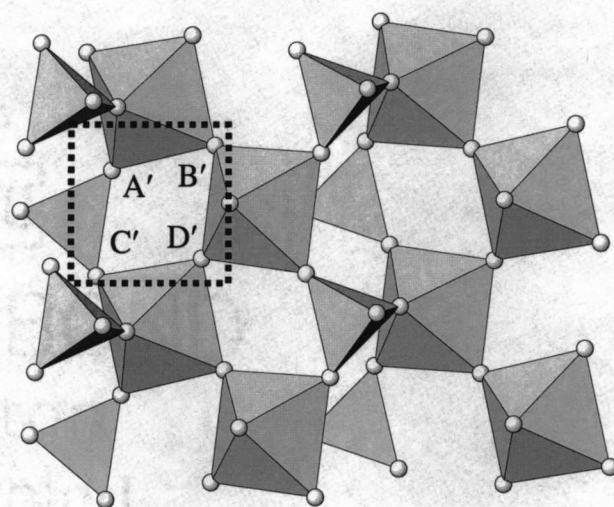


Figure 3.13.a. Tilting angles in the monoclinic NbOPO₄ structure

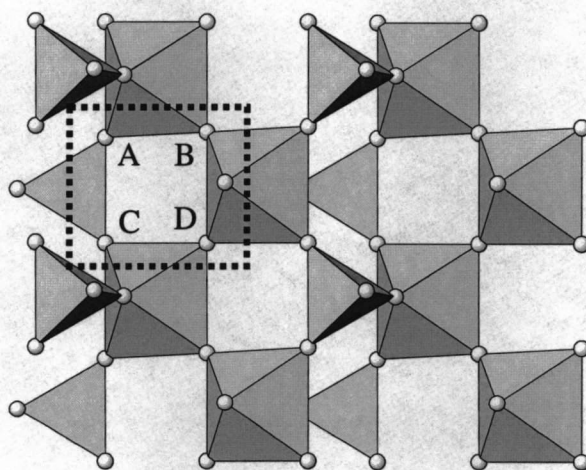


Figure 3.13.b. Tilting angles in the orthorhombic NbOPO₄ structure

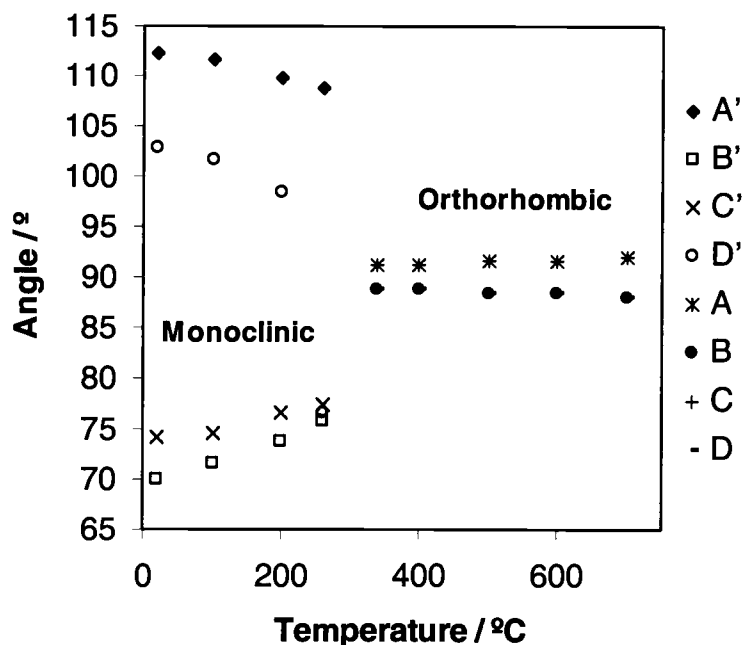


Figure 3.14. Polyhedra tilt angles as a function of temperature

3.7. Discussion

Distance Least Squares (DLS) calculations indicate that the monoclinic NbOPO_4 structure can be built of perfectly regular polyhedra, however the orthorhombic structure cannot. In the monoclinic structure by setting Nb-O distances equal to 1.99 Å and the P-O distances set to 1.52 Å, the cell dimensions refine to the following: $a = 11.23$ Å, $b = 5.39$ Å, $c = 6.62$ Å, and $\beta = 92.2^\circ$ and the residual is minimized. However, when the same distances are set in the orthorhombic structure, the residual increases and the following cell dimensions are obtained: $a = 11.31$ Å, $b = 5.32$ Å, and $c = 6.66$ Å. The distortion of the polyhedra seems to be related to the A-C and B-D lengths in Figure 3.13. The

tetrahedron edge is smaller than the octahedron edge and this distorts the polyhedra and makes these lengths unequal. If the distances are adjusted in the DLS program so that the A-C and B-D lengths are equal, the residual is minimized, indicating that this type of regularity is optimal for the orthorhombic form. To account for this large change in polyhedral lengths, the cell dimensions increased dramatically to values of $a = 11.78 \text{ \AA}$, $b = 5.35 \text{ \AA}$, and $c = 6.92 \text{ \AA}$.

CRUSH calculations find one rigid unit mode in the orthorhombic structure and none in the monoclinic structure. Presumably this relates to the phase transformation, the polyhedra in the monoclinic structure must distort if they are to rock into the high temperature polymorph. The RUM found in the orthorhombic form does not correspond to a vibration in the bc direction. The dynamic tilting is not as great in the ac plane (Figure 3.15) compared to the bc plane (Figure 3.12).

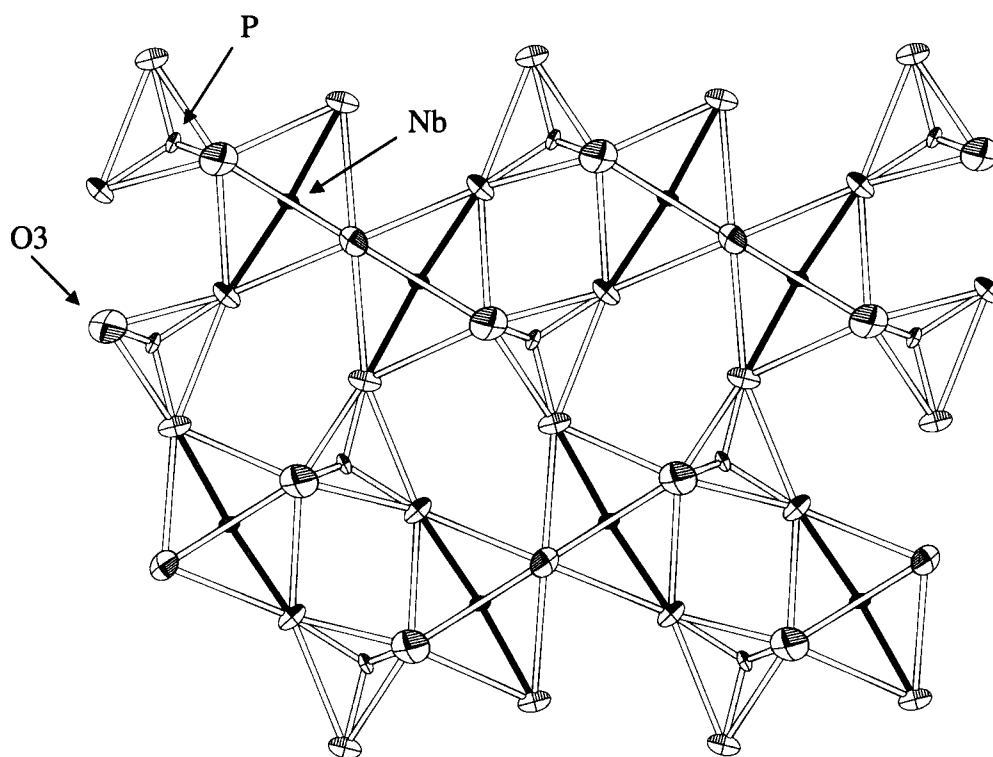


Figure 3.15. Partial view of the anisotropic thermal parameters in the orthorhombic NbOPO₄ structure looking down the *b* axis

The negative thermal expansion seen in this compound can be visualized in one or two ways, either a shortening of a particular bond length or a decrease in the metal-oxygen-metal angle. Figure 3.16 shows a schematic of the metal-oxygen-metal bond and the metal-metal bond distance will decrease if 1) the angle a decreases or 2) the length b decreases.

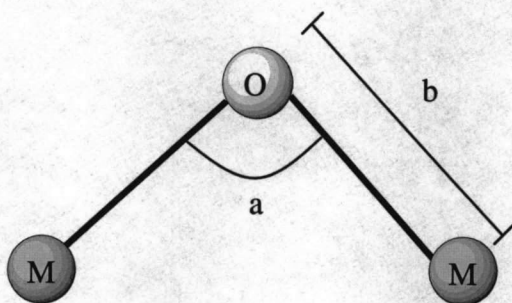


Figure 3.16. Schematic of decreasing metal-metal bonds

Figure 3.17 shows the change in metal-oxygen-metal bonds over the temperature range studied. The Nb-O-Nb angle shows no change in the monoclinic form or the orthorhombic form, while the Nb-O-P angle increases over the entire temperature range. Examination of Figure 3.18 shows no change in the apparent average P-O bond in the monoclinic polymorph, but this decreases over the temperatures involving the orthorhombic polymorph.

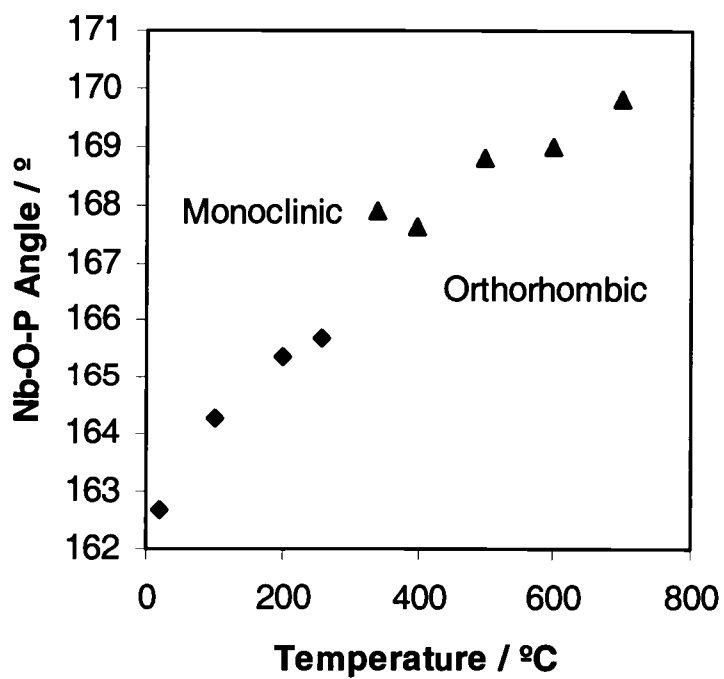
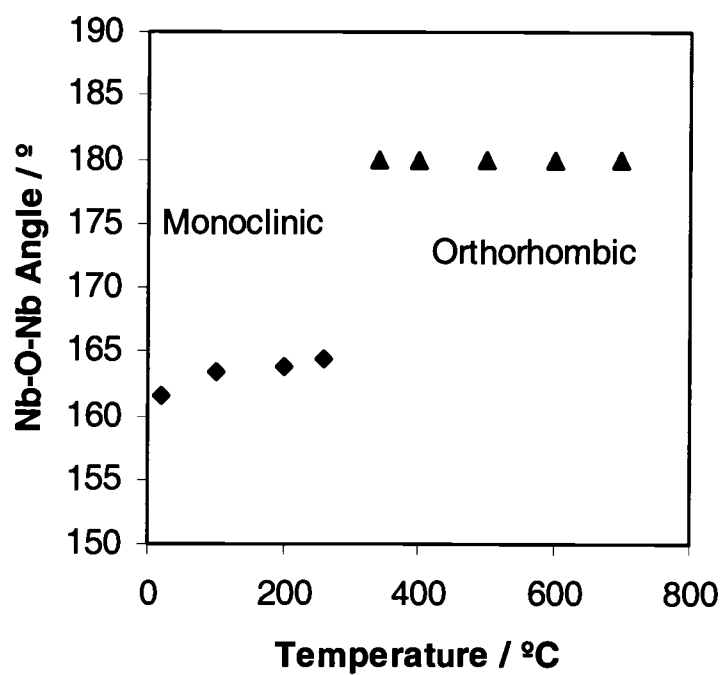


Figure 3.17. Changes in metal-oxygen-metal angles with temperature

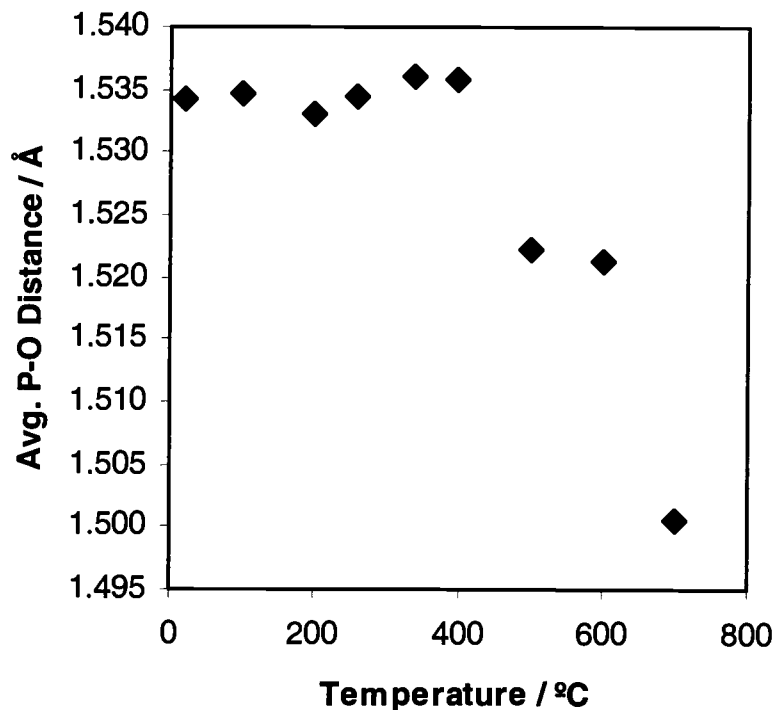


Figure 3.18. Changes in average P-O bond distance with temperature

The orthorhombic polymorph exhibits negative thermal expansion. This property can be explained in terms of the flexibility of the octahedra and tetrahedra. Tilting of the bridging angles between polyhedra allows this structure to rock back and forth. One possible rocking motion is depicted in Figure 3.19. The O(3) and O(1) atoms in the orthorhombic structure are the bridging oxygen atoms that demonstrate the greatest thermal motion. This is consistent with the rocking angles of the polyhedra seen in Figure 3.13. As the temperature is decreased, the structure is locked into the monoclinic polymorph.

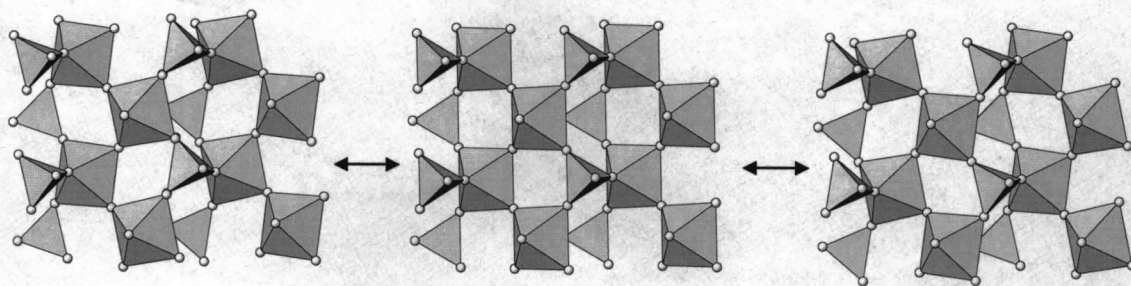


Figure 3.19. Possible rocking motion for NbOPO₄ looking down the *a* axis

Orthorhombic NbOPO₄ represents another structure that displays negative thermal expansion based on the facile tilting motion of the corner-shared polyhedra. As this compound is cooled a phase transition occurs; one tilted picture of the structure is “frozen” in and this structure is the monoclinic NbOPO₄ form.

3.8. References

1. Enerst M. Levin and Robert S. Roth, *J. Solid State Chem.*, 2, 250 (1970)
2. A. LeClaire, H. Chahboun, D. Groult and B. Raveau, *Z. fur Krist.*, 177, 277 (1986)
3. A. C. Larson and R. B. von Dreele, LANSCE, Los Alamos National Laboratory, Los Alamos, N.M., 1994
4. A. LeBail, H. Duroy and J. L. Fourquet, *Mat. Res. Bull.*, 23, 447 (1988)
5. W. A. Dollase, *J. Appl. Cryst.*, 19, 267 (1986)
6. Deborah L. Serra and Shiou-Jyh Hwu, *Acta Cryst.*, C48, 733 (1992)
7. Maple Software, Waterloo Maple Inc., 1996
8. William R. Busing and Henri A. Levy, *Acta Cryst.*, 17, 142 (1964)

Chapter 4

Negative Thermal Expansion in the High Temperature Polymorph of Tetragonal TaOPO₄

4.1. Introduction

In 1971, Longo and co-workers reported the preparation of tetragonal TaOPO₄ using high-pressure synthesis methods (1). This compound was found to be isostructural with tetragonal NbOPO₄ (2). Their synthesis used the monoclinic form of TaOPO₄ (3) as a starting material for high-pressure studies. At pressures greater than 25 kbar and over the temperature range of 500 to 1500 °C synthesis conditions, the monoclinic form transformed to the tetragonal structure and could be retained at atmospheric pressure by quenching. A comparison of the X-ray densities of tetragonal NbOPO₄ (4.044 g/cm³) (2) and the monoclinic structure (3.452 g/cm³) (3) showed a decrease of 15% on transformation to the monoclinic form, indicating that the monoclinic TaOPO₄ should transform to the tetragonal polymorph with pressure.

4.2. Experimental

A polycrystalline sample of monoclinic TaOPO₄ was prepared and used in a subsequent high-pressure experiment. Attempts to prepare tetragonal TaOPO₄ by direct solid-state methods at atmospheric pressure were unsuccessful. Stoichiometric quantities of Ta₂O₅ (Alfa Aesar, 99%) and (NH₄)₂HPO₄

(Mallinckrodt) were thoroughly ground in an agate mortar and placed in an alumina crucible. This was heated for 15 hours at 1250 °C and allowed to cool to room temperature. A white colored product was obtained. The X-ray diffraction pattern matched that of monoclinic TaOPO₄ (PDF # 84-1096).

A sample of monoclinic TaOPO₄ was sent to the DuPont Central Research & Development Section in Wilmington, DE. The sample was sealed in a gold ampoule and placed in the center of a tetrahedral anvil press. A pressure of 58 kbar was uniformly applied using a hydraulic piston arrangement. This was heated to 800 °C and maintained at this temperature for 2 hours. The pressure was released after cooling the sample to room temperature.

A differential scanning calorimetry measurement was taken with a TA Instruments DSC 2920. The sample was heated at a rate of 10 °C/minute from room temperature to 550 °C under a flow of nitrogen.

X-ray powder diffraction data were obtained with an INEL diffractometer using monochromated Cu K α radiation. A small amount of sample, an internal standard (NIST SRM Si 640b) and ethanol were mixed and dropped onto a sample holder and the solvent was allowed to evaporate. Diffraction patterns were collected over the temperature range from 25 to 500 °C.

4.3. Description of Structure

Tetragonal TaOPO₄ crystallizes in space group $P4/n$ (No. 85). There are two molecular units per unit cell and four types of crystallographically unique sites. This compound is isostructural with the tetragonal form of NbOPO₄ and similarly its connectivity consists of a three-dimensional network built of corner-sharing TaO₆ octahedra and PO₄ tetrahedra (Figure 4.1). One layer of polyhedra has been removed for clarity.

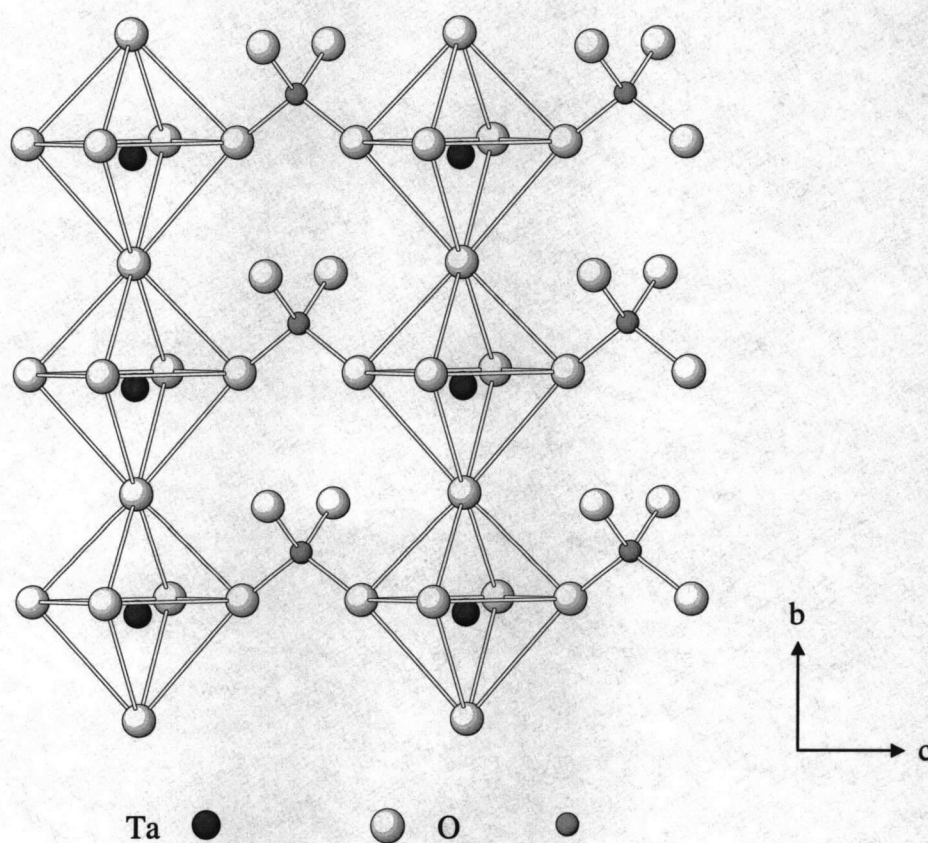


Figure 4.1. Polyhedra connectivity in tetragonal TaOPO₄

The TaO_6 octahedra exhibit a ferroelectric-type distortion. Each tantalum atom is displaced along the c axis away from the center of the polyhedron. This results in chains of alternating short and long Ta-O bonds. Figure 4.2 shows a schematic of this distortion along the c axis. Adjacent chains of TaO_6 octahedra have opposite polarities and therefore no net moment occurs over the entire structure.

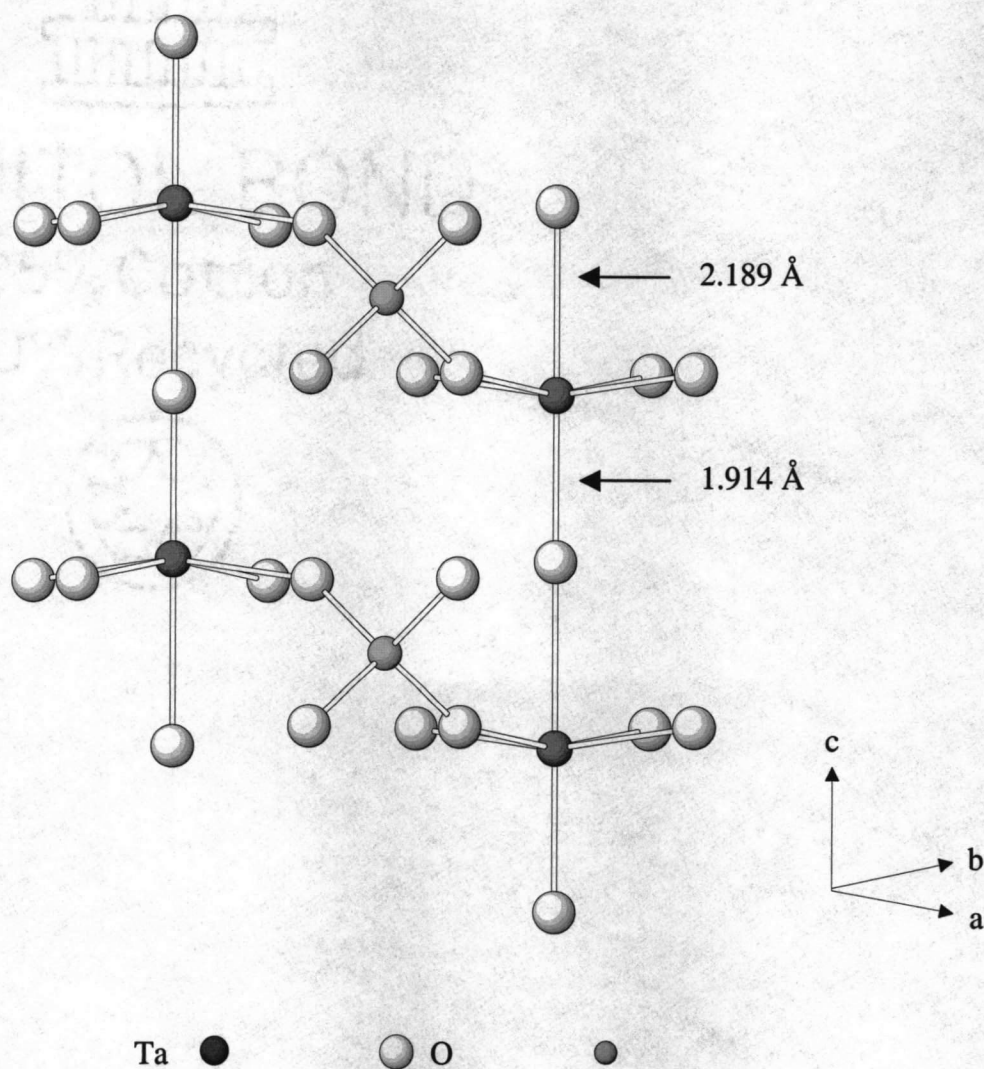


Figure 4.2. Ferroelectric-type distortion along the TaO_6 octahedral chains

This distortion is slightly smaller for the tetragonal TaOPO₄ structure compared to the niobium analog. The short and long metal-oxygen bonds (Ta-O: 1.914, 2.189 Å; Nb-O: 1.746, 2.360 Å) differ despite similar radii for the tantalum and niobium ions. Shannon reports an ionic radius value of 0.64 Å for both Ta⁵⁺ and Nb⁵⁺ in octahedral coordination (4). The difference in the amount of distortion can be attributed to the greater covalency in the Nb-O bond compared to that in the Ta-O bond.

4.4. Structural Refinements

All refinements were performed using the GSAS software package (5). The refinement of Si as a second phase was introduced to calibrate the instrumental zero point. The structure presented by Longo et al. (1) was used as the initial model for tetragonal TaOPO₄ phase. Cell dimensions, background coefficients, and profile coefficients were determined by fitting the entire pattern using the Le Bail method (6) within the GSAS software. These values were then fixed and the Rietveld method was employed to ascertain the scale factor, atomic positions and the metal atom thermal parameters. A March-Dollase preferred orientation variable (7) was introduced into the TaOPO₄ phase refinement. The best fit was obtained with the choice of the 001 direction leading to a March-Dollase parameter greater than 1.0. For temperatures greater than 25 °C, the zero point was fixed at 0.05 centi-degrees (found from the room temperature refinement) and a parameter for sample height correction was refined. Results

from a particular data set were used for the subsequent refinement input. A systematic refinement guideline was used for each temperature data point. Refinement statistics are listed in Table 4.1. Rietveld plots at 25 and 600 °C are shown in Figure 4.3.

Table 4.1. X-ray Diffraction Refinement Statistics for Tetragonal TaOPO₄

Temp. (°C)	χ^2	wRp	Rp
20	3.496	0.0970	0.0756
100	3.692	0.0889	0.0686
150	3.677	0.0916	0.0706
200	3.657	0.0933	0.0715
250	3.810	0.0956	0.0745
300	3.676	0.0949	0.0725
350	3.997	0.0996	0.0769
400	3.548	0.0933	0.0723
450	3.836	0.0986	0.0756
500	4.101	0.0988	0.0755
600	4.400	0.1081	0.0787

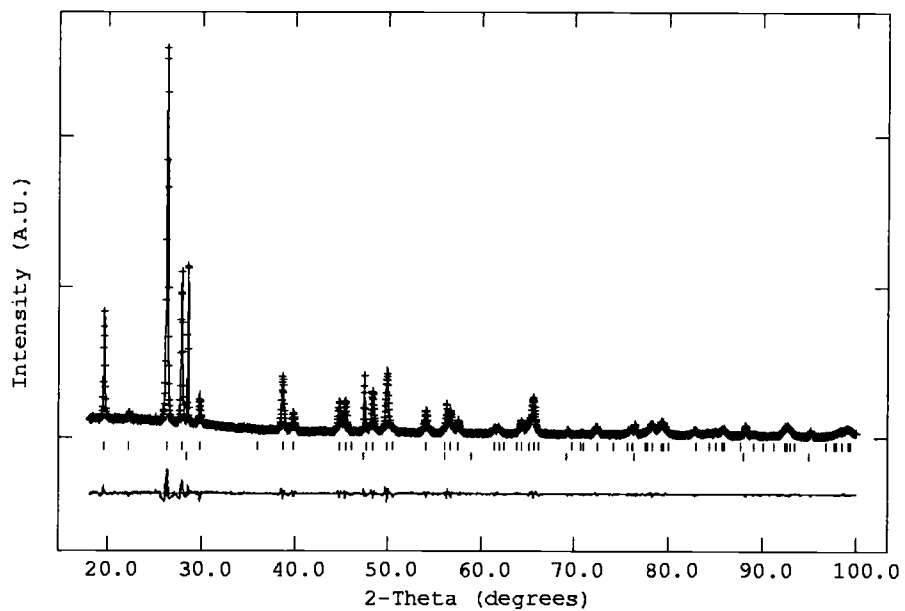


Figure 4.3.a. Observed, calculated, and difference profiles for tetragonal TaOPO₄ at 25 °C

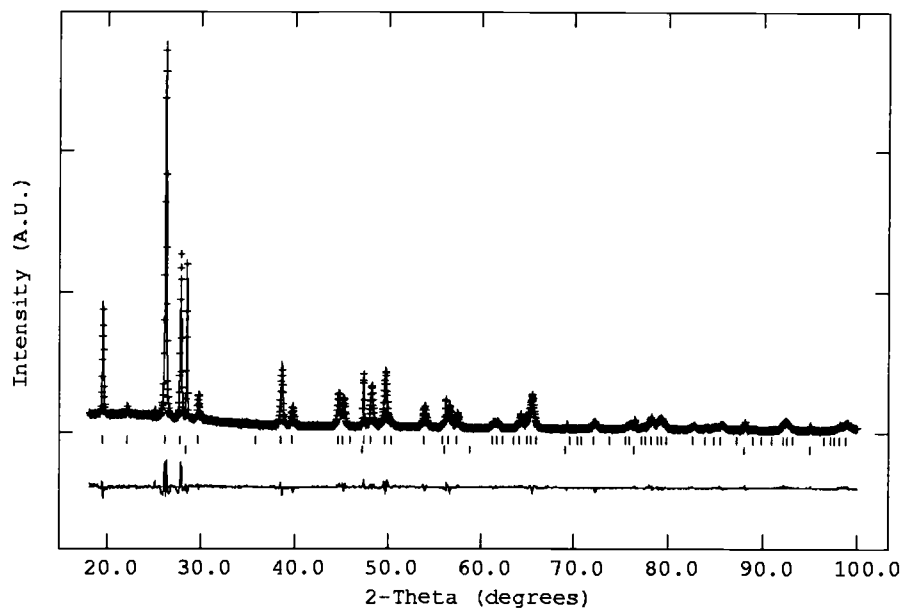


Figure 4.3.b. Observed, calculated, and difference profiles for tetragonal TaOPO₄ at 600 °C

Preparation of the tetragonal TaOPO_4 under high pressure introduces strain into the compound. This results in peak broadening which can be seen in Figure 4.4. The TaOPO_4 peaks are significantly broadened compared to the Si 111 reflection.

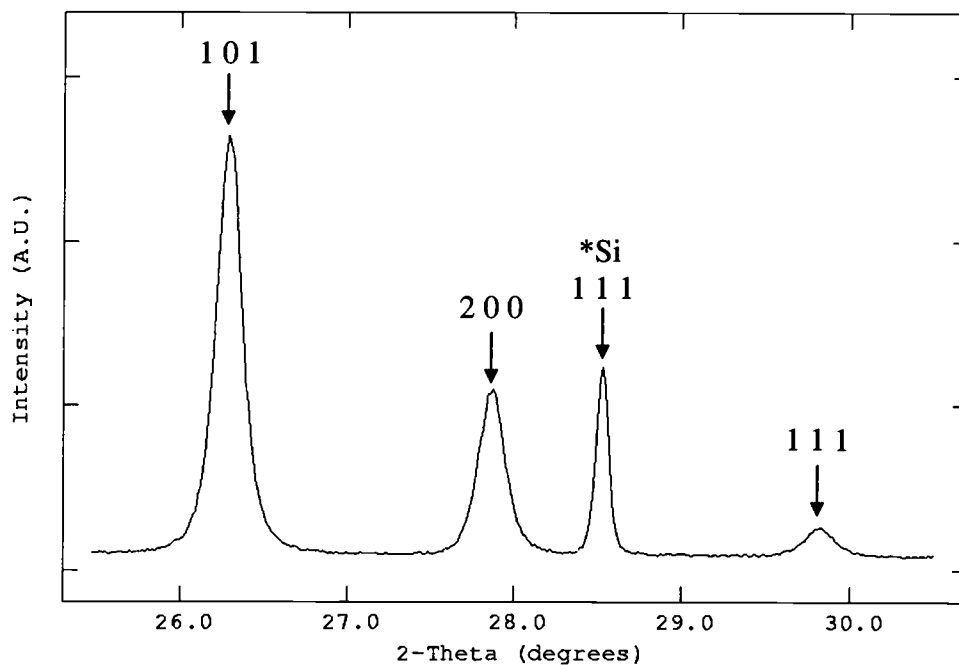


Figure 4.4. Peak broadening in the tetragonal TaOPO_4 sample

The profile coefficients from a constant wavelength powder profile function can be interpreted to give strain information (5). The Lorentzian component of a constant wavelength peak shape yields a strain term that is defined by Equation 4.1. The Y and Y_i components are the refined profile

coefficients for the TaOPO₄ and Si phases, respectively. Y_i represents any instrumental or spectral broadening contribution.

$$S = \frac{\pi}{18000}(Y - Y_i) \times 100\% \quad \text{Equation 4.1}$$

Table 4.2 lists the values of Y and Y_i obtained for each temperature measurement and the strain term calculated from these values.

Table 4.2. Strain Values for Tetragonal TaOPO₄

Temp. (°C)	Y_i (Si)	Y (TaOPO ₄)	Strain % (centi-°)
20	10.95	48.92	0.6627
100	8.483	46.65	0.6661
150	8.612	46.89	0.6681
200	10.85	47.05	0.6318
250	13.09	47.02	0.5922
300	8.547	46.31	0.6591
350	10.68	45.25	0.6034
400	8.293	46.43	0.6656
450	7.705	47.42	0.6932
500	10.35	46.96	0.6390
600	8.141	44.93	0.6421

One Lorentzian profile coefficient, X , can be used to define the particle size of the TaOPO_4 phase (5). The particle size, p , is defined in Equation 4.2, where K is the Scherrer constant.

$$p = \frac{18000 K \lambda}{\pi X} \quad \text{Equation 4.2}$$

The TaOPO_4 particle sizes as a function of temperature are listed in Table 4.3. Since these exceed 1000 \AA there is negligible peak broadening due to particle size (8), indicating that strain is the main contributor to the peak broadening in this sample.

Table 4.3. Particle Sizes for Tetragonal TaOPO_4

Temp. ($^{\circ}\text{C}$)	TaOPO_4 X	TaOPO_4 Particle Size (\AA)
20	1.435	5536
100	1.720	4619
150	1.381	5753
200	1.346	5902
250	1.607	4944
300	1.381	5753
350	2.095	3792
400	1.353	5872
450	1.280	6206
500	1.303	6097
600	1.463	5430

The observed diffraction pattern was indexed with a tetragonal unit cell. Refinement of cell dimensions at room temperature gave the following values: $a = 6.4156(1) \text{ \AA}$ and $c = 4.0037(1) \text{ \AA}$. This gives a calculated density of 5.88 g/cm^3 , which corresponds to a 16 % increase in density from the monoclinic TaOPO₄ density of 4.921 g/cm^3 (3).

For the temperatures between 25 and 200 °C, the final parameters were in good agreement with results from previous studies (13) with space group $P4/n$ (No. 85). Attempts to refine these data in the $P4/nmm$ space group (No. 129) setting were unsuccessful. At higher temperatures, refinement in the $P4/n$ space group resulted in divergence and the $P4/nmm$ space group was adopted.

4.5. High Temperature Phase Transition

Similar to the isostructural NbOPO₄ compound, the tetragonal TaOPO₄ undergoes a phase transition at higher temperatures. However, this phase transition was not seen in the differential scanning calorimetry measurement, typical of a second order type transition. The first indication of this transformation is in the change in a and b cell dimensions as a function of temperature (Figure 4.5). Between 25 and 200 °C the a and b cell edges increase as the temperature is raised. Above this temperature, negative thermal expansion is seen for these same cell edges. The c cell edge increases over the entire temperature range. Table 4.4 lists the coefficients of thermal expansion associated with each cell dimension. The negative thermal expansion of the a and

b cell edges dominate the overall volume contraction at temperatures above 200 °C (Figure 4.6).

Table 4.4. Thermal Expansion Coefficients for Tetragonal TaOPO₄

Temperature Range (°C)	Cell Dimension	α (°C ⁻¹)
20 - 150	a, b	5.45×10^{-6}
200 - 600	a, b	-2.78×10^{-6}
20 - 150	c	6.07×10^{-6}
200-600		3.87×10^{-6}
20 - 150	Volume	1.70×10^{-5}
200 - 600		-1.70×10^{-6}
20 - 150	α_1	5.67×10^{-6}
200 - 600		-5.67×10^{-7}

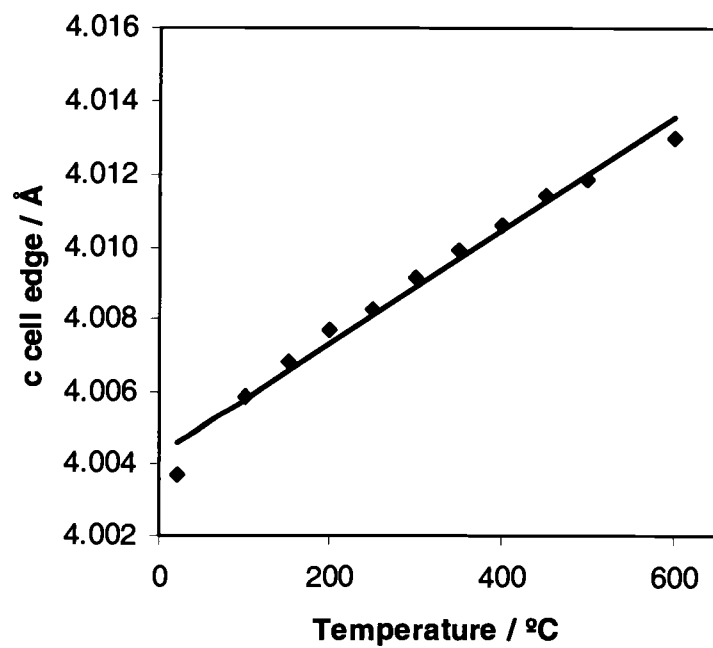
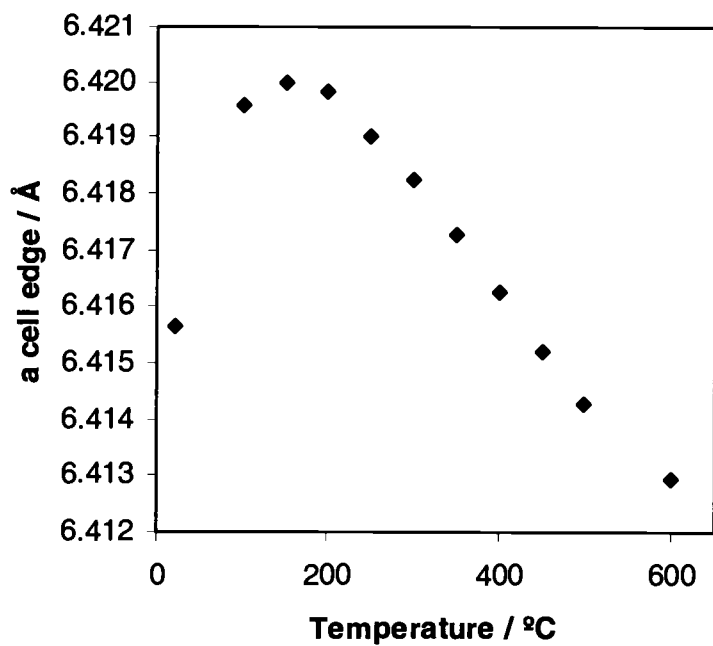


Figure 4.5. Variation of cell edge lengths with temperature

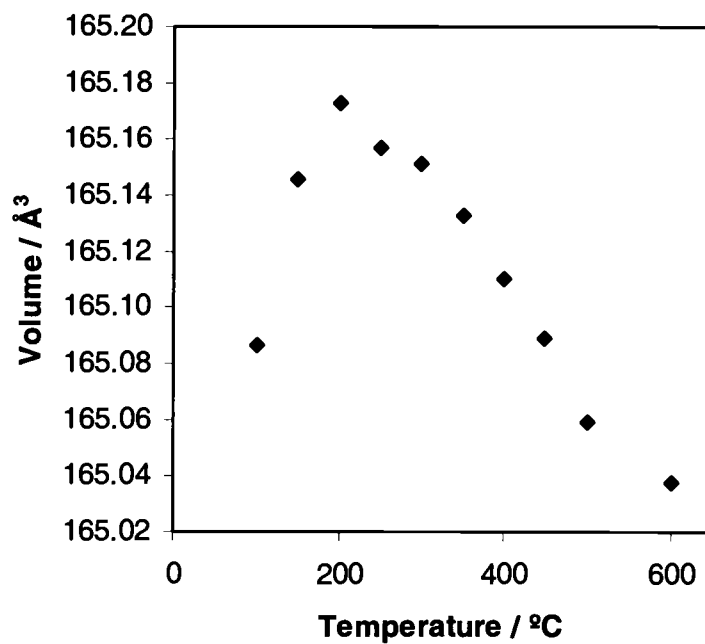


Figure 4.6. Variation of volume with temperature

The relationship between the structures of TaOPO_4 in space groups $P4/n$ and $P4/nmm$ is shown in Figure 4.7.

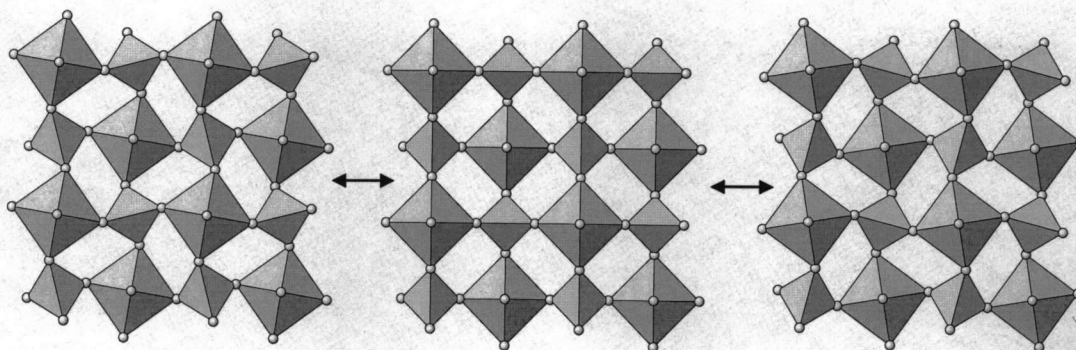


Figure 4.7. Structure of tetragonal TaOPO_4 looking down the c axis. Central structure represents the $P4/nmm$ setting and the tilted versions on each side are in space group $P4/n$.

Both space groups have a phosphorus atom in a $\frac{1}{4}, \frac{3}{4}, \frac{1}{2}$ special position, and a tantalum and oxygen atom in a $\frac{1}{4}, \frac{1}{4}, z$ position. The second crystallographically unique oxygen (corresponding to the oxygen of the phosphate tetrahedron) is in a xyz position in the $P4/n$ space group but moves onto a $\frac{3}{4}, y, z$ position in $P4/nmm$. The variations in atomic coordinates are listed in Table 4.5.

Table 4.5. Variation of Atomic Coordinates with Temperature

Temp. (°C)	z (Ta)	z (O1)	x (O2)	y (O2)	z (O2)
25	0.7701(3)	0.236(4)	0.774(4)	0.4416(8)	0.288(2)
100	0.7694(3)	0.229(4)	0.764(3)	0.4448(8)	0.289(2)
150	0.7668(4)	0.226(4)	0.761(4)	0.4423(9)	0.286(2)
200	0.7685(3)	0.232(4)	3/4	0.4401(7)	0.285(2)
250	0.7686(4)	0.225(4)	3/4	0.4417(7)	0.286(2)
300	0.7683(4)	0.233(4)	3/4	0.4406(8)	0.287(2)
350	0.7681(4)	0.226(4)	3/4	0.4411(8)	0.289(2)
400	0.7687(4)	0.227(4)	3/4	0.4401(8)	0.289(2)
450	0.7686(4)	0.231(4)	3/4	0.4399(8)	0.289(2)
500	0.7683(4)	0.229(4)	3/4	0.4424(8)	0.289(2)
600	0.7689(4)	0.227(4)	3/4	0.4410(9)	0.291(2)

The $P4/nmm$ structure is mainly characterized by the change of the O2 x parameter from a general position to a value of $\frac{3}{4}$. This change is depicted graphically in Figure 4.8.

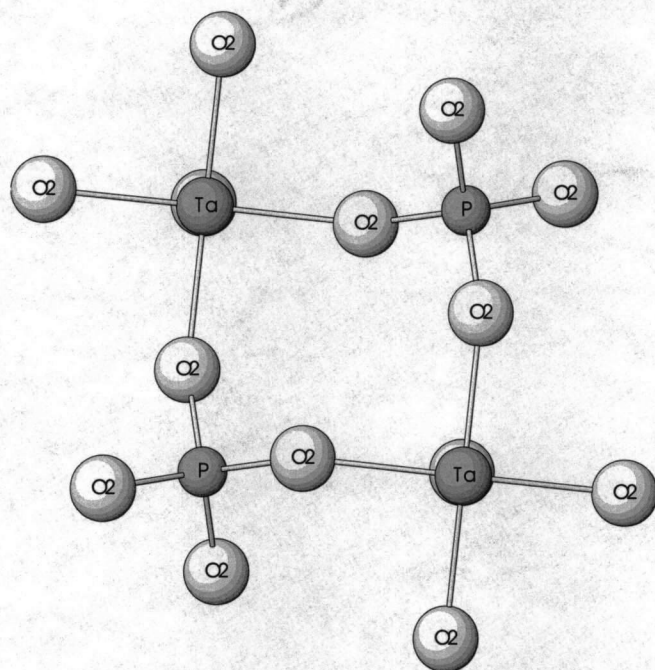


Figure 4.8.a. Partial view of the tetragonal TaOPO₄ structure in the $P4/n$ space group

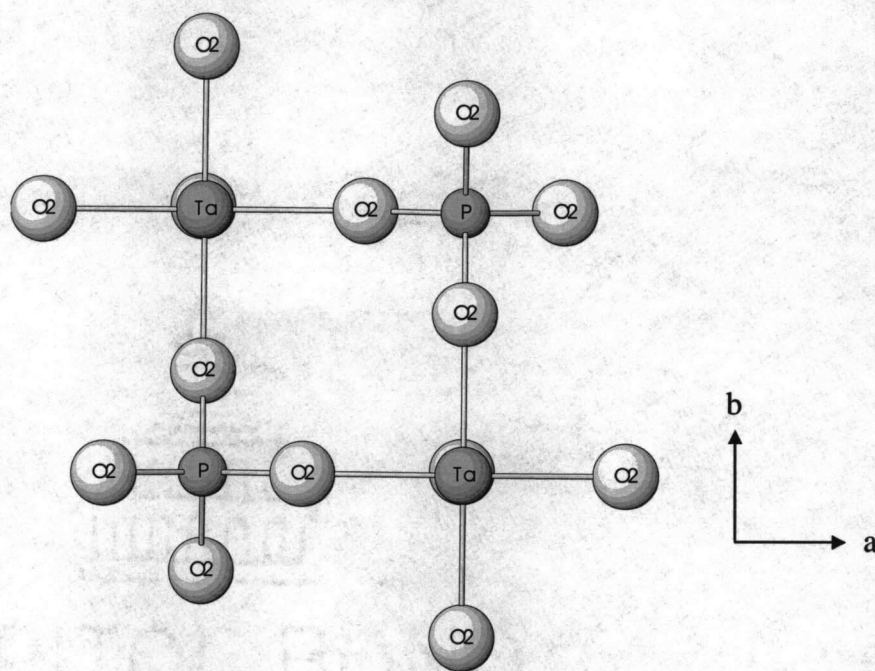


Figure 4.8.b. Partial view of the tetragonal TaOPO₄ structure in the $P4/nmm$ space group

4.6. Discussion

It is difficult to make very conclusive remarks on the trends of metal-oxygen bond lengths due to the uncertainty in determining very accurate oxygen positions with X-ray diffraction. However, this compound undergoes a similar phase transition to the $P4/nmm$ space group like the tetragonal NbOPO₄ analog. The rocking motion of the polyhedra (Figure 4.7) is one possible tilting motion that gives rise to negative thermal expansion in the a and b directions. The positive thermal expansion seen in the c cell edge is most likely dominated by the lengthening of the long (weak) Ta-O bond at higher temperatures. The librations of the bridging oxygen atoms in the high temperature polymorph are most likely slightly larger than in the tetragonal NbOPO₄ since there is more contraction of the a and b cell edges as the temperature is increased.

4.7. References

1. J. M. Longo, J. W. Pierce and J. A. Kafalas, *Mat. Res. Bull.*, 6, 1157 (1971)
2. John M. Longo and Peder Kierkegaard, *Acta Chem. Scand.*, 20, 72, (1966)
3. Ernest M. Levin and Robert S. Roth, *J. Solid State Chem.*, 2, 250 (1970)
4. R. D. Shannon, *Acta Cryst.*, A32, 751 (1976)
5. A. C. Larson and R. B. von Dreele, LANSCE, Los Alamos National Laboratory, Los Alamos, N.M., 1994
6. A. LeBail, H. Duroy and J. L. Fourquet, *Mat. Res. Bull.*, 23, 447 (1988)
7. W. A. Dollase, *J. Appl. Cryst.*, 19, 267 (1986)
8. B. D. Cullity *Elements of X-ray Diffraction*; Addison-Wesley Publishing: Reading, MA, 1978; p. 284

Chapter 5

Negative Thermal Expansion in Orthorhombic TaOVO₄

5.1. Introduction

In a study of the ZnO-Ta₂O₅-V₂O₅ system, Brown reported the formation of the TaVO₅ compound (1, 2). This compound was prepared with ammonium metavanadate and tantalum pentoxide starting materials, however, no further synthesis conditions were given. No structural information was detailed, however, they present thermal expansion data determined by dilatometry. A thermal expansion coefficient (α) of $-4.4 \times 10^{-7} \text{ }^\circ\text{C}^{-1}$ was reported over a temperature range of 25 to 700 $^\circ\text{C}$. In 1986, this material was studied between 150 and 300 K for possible space applications (3). This work was also based on dilatometer data. The thermal expansion data suggested a phase transition near 260 K that was accompanied by a change in α from $-4.0 \times 10^{-6} \text{ K}^{-1}$ above 260 K to a positive α of $50 \times 10^{-6} \text{ K}^{-1}$ below.

In 1988, Chahboun, Groult, and Raveau (4) refined the structure of a powder sample of orthorhombic TaOVO₄. They found it to be isomorphous with orthorhombic NbOPO₄ (5). X-ray powder analysis yielded the following cell dimensions: $a = 11.860(3) \text{ \AA}$, $b = 5.516(1) \text{ \AA}$, and $c = 6.928(1) \text{ \AA}$ and crystallization in the *Pnma* space group.

Since this structure is not cubic, previous reports of thermal expansion data based on dilatometry are not very conclusive. Diffraction analysis and dilatometry often yield different thermal expansion coefficients for an anisotropic material. This thesis work attempts to elucidate the structural changes that occur at elevated temperatures and give detailed information about the negative thermal expansion exhibited by this compound.

5.2. Experimental

A yellow colored polycrystalline sample of TaOVO₄ was synthesized by heating an intimately ground mixture of Ta₂O₅ (Alfa Aesar, 99 %) and NH₄VO₃ (Alfa Aesar, 99 %) in an alumina crucible for 24 hours at 700 °C. The sample was then thoroughly ground and heated again at 700 °C for 1 day.

Dilatometer measurements were made using a Netzsch STA 409 system. A 25 cm × 5 cm × 5 cm pellet was pressed and annealed at 750 °C for two hours before being used on the dilatometer. In the dilatometer experiment the pellet was heated at a rate of 5 °C/minute from room temperature to 800 °C.

Differential scanning calorimetry was carried out on a TA Instruments DSC 2920 with liquid nitrogen cooling. The sample was placed in an aluminum pan and heated from room temperature to -120 °C at a rate of 5 °C/minute.

Variable temperature X-ray diffraction data were obtained on an INEL diffractometer with Cu K α radiation using Si (NIST SRM 640b) as an internal standard. The sample, internal standard, and a small amount of chloroform were

mixed and the slurry was dropped onto the sample holder. The solvent was allowed to evaporate and the holder was placed in a resistively heated furnace attachment. Data collections were performed at room temperature up to 600 °C in 100 °C increments.

5.3. Description of Structure

The orthorhombic TaOVO₄ structure crystallizes in the *Pnma* space group (No. 62). The unit cell contains six crystallographically unique atoms (Table 5.1) and four molecular units.

Table 5.1. Atomic Coordinates for Orthorhombic TaOVO₄

Atom	Site	Symmetry	x/a	y/b	z/c
Ta	4c	m	0.0610(8)	1/4	0.343(2)
V	4c	m	0.339(2)	1/4	0.543(3)
O (1)	4b	1	0	0	1/2
O (2)	8d	1	0.119(4)	-0.010(9)	0.132(6)
O (3)	4c	m	0.203(4)	1/4	0.464(6)
O (4)	4c	m	0.418(4)	1/4	0.338(7)

Each tantalum atom is connected to six oxygen atoms and every phosphorus atom is tetrahedrally coordinated to four oxygen atoms. The connectivity is such that each TaO₆ octahedron is connected to two other

octahedra on adjacent oxygen atoms. The other apex oxygen atoms are linked to PO_4 tetrahedra. Figure 5.1 depicts the bc plane of this structure.

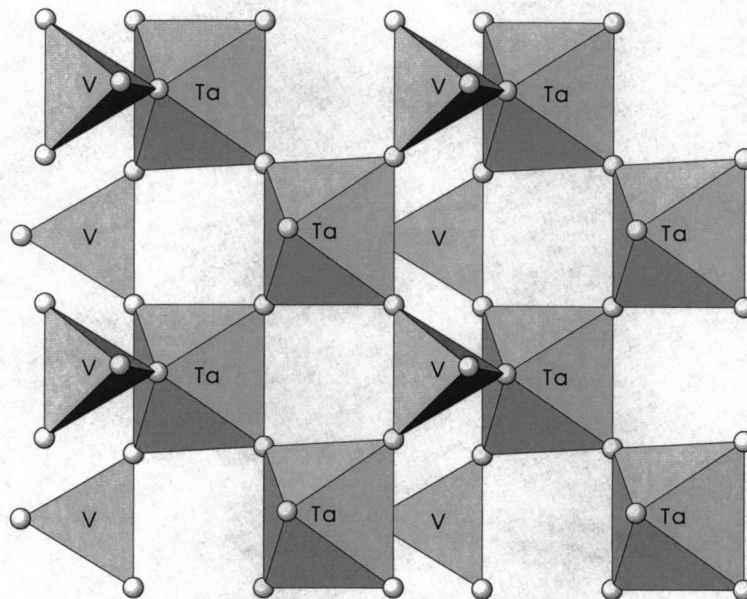


Figure 5.1. Polyhedra connectivity in orthorhombic TaOVO_4 along the bc plane

5.4. Preliminary Thermal Analysis

In a preliminary study of the thermal expansion behavior, this compound was studied using dilatometry. The relative thermal expansion as a function of temperature is shown in Figure 5.2. This material exhibits negative thermal expansion over the entire temperature range of 25 to 800 °C. The slight curvature seen at temperatures below 100 °C is typical of dilatometer measurements but does not indicate that the thermal expansion is non-linear over this temperature

range. The thermal expansion coefficient was calculated to have a value of $-4.11 \times 10^{-6} \text{ }^\circ\text{C}$. This is similar to the value found by Chu and co-workers (3). This compound was used for subsequent X-ray diffraction measurements.

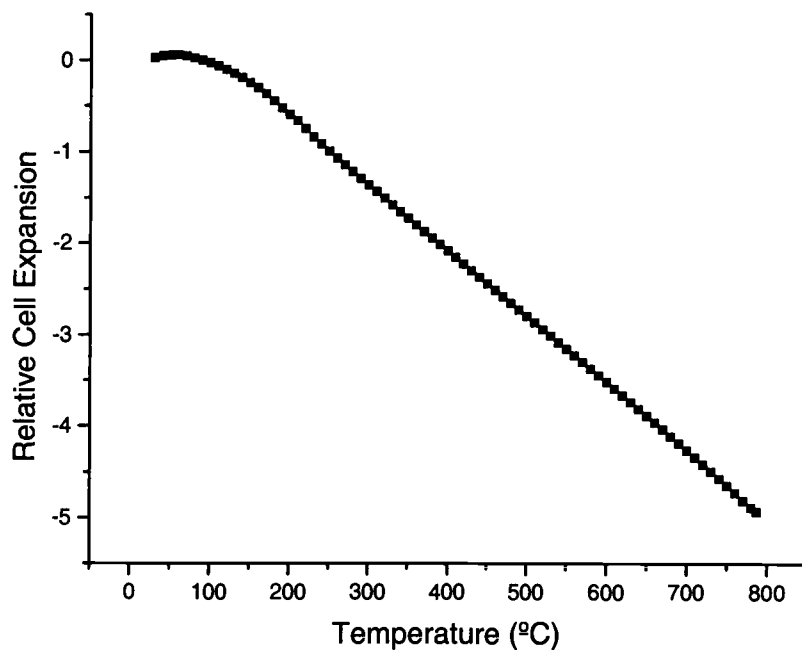


Figure 5.2. Dilatometer plot for orthorhombic TaOVO₄

Since this TaOVO₄ compound is isomorphous with the high temperature orthorhombic form of NbOPO₄, differential scanning calorimetry was employed to determine whether a phase transition could be seen at lower temperatures. Figure 5.3 shows the DSC curve at lower temperatures. The onset temperature for the heating and cooling curves are approximately equal. This temperature is

also consistent with the phase transition temperature determined by the dilatometer experiment done by Chu and co-workers (3).

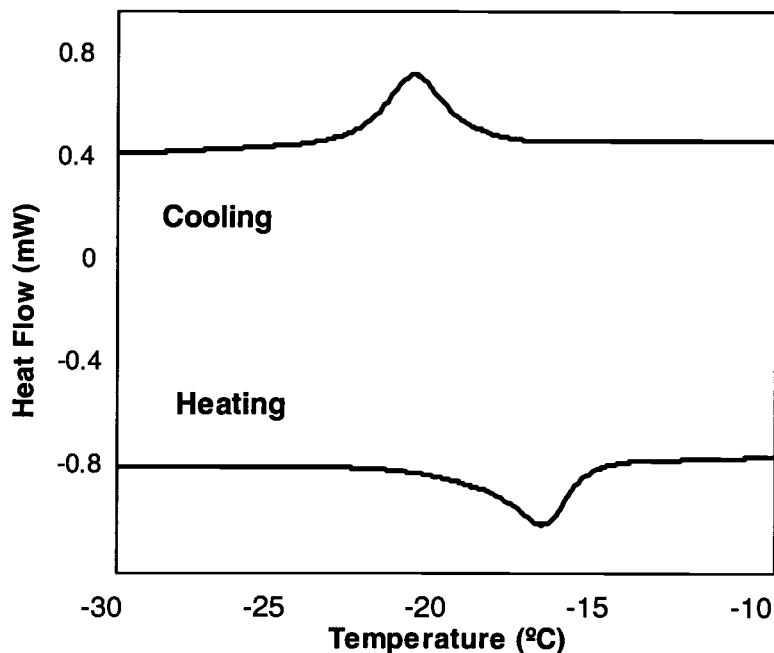


Figure 5.3. Differential scanning calorimetry plot for orthorhombic TaOVO₄

5.5. Structural Refinements

The structure was refined with the GSAS software suite (6). Each refinement involved two phases, one of the orthorhombic TaOVO₄ and the other from the Si internal standard. The Si refinement allowed for the independent determination of the instrumental zero offset. A zero point value of -0.11 degrees was obtained from the room temperature measurement. This value was fixed for temperatures above room temperature. A consistent refinement strategy was used for each temperature data point. The Le Bail method (7) was employed to

determine lattice parameters, background coefficients, and profile parameters. After these were established, the Rietveld refinement was incorporated to fit variables such as scale, phase fractions, atomic coordinates, and metal atom isotropic thermal parameters. A typical refinement involved fitting 9 background coefficients, cell dimensions, 5 profile coefficients, 2 phase fractions, 11 atomic positions, and 2 isotropic thermal parameters. There were 5467 observations over the 2-theta range of 18 to 100 °. The observed and calculated diffraction profiles for the 25 °C and 600 °C refinements are shown in Figure 5.4. Refinement statistics are listed in Table 5.2.

Table 5.2. Refinement Statistics for Orthorhombic TaOVO₄

Temp. (°C)	χ^2	wRp	Rp
20	5.228	0.1085	0.0835
100	5.187	0.1082	0.0837
200	5.935	0.1108	0.0852
300	5.616	0.1115	0.0867
400	6.200	0.1205	0.0929
500	6.695	0.1218	0.0939
600	7.158	0.1256	0.0967

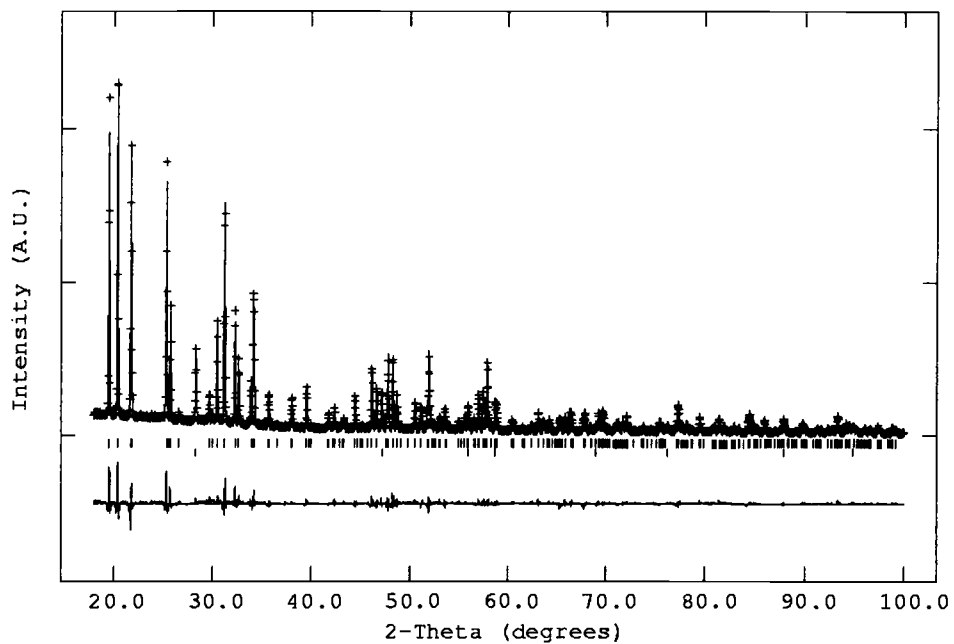


Figure 5.4.a. Observed, calculated, and difference profiles for orthorhombic TaOVO₄ at 25 °C

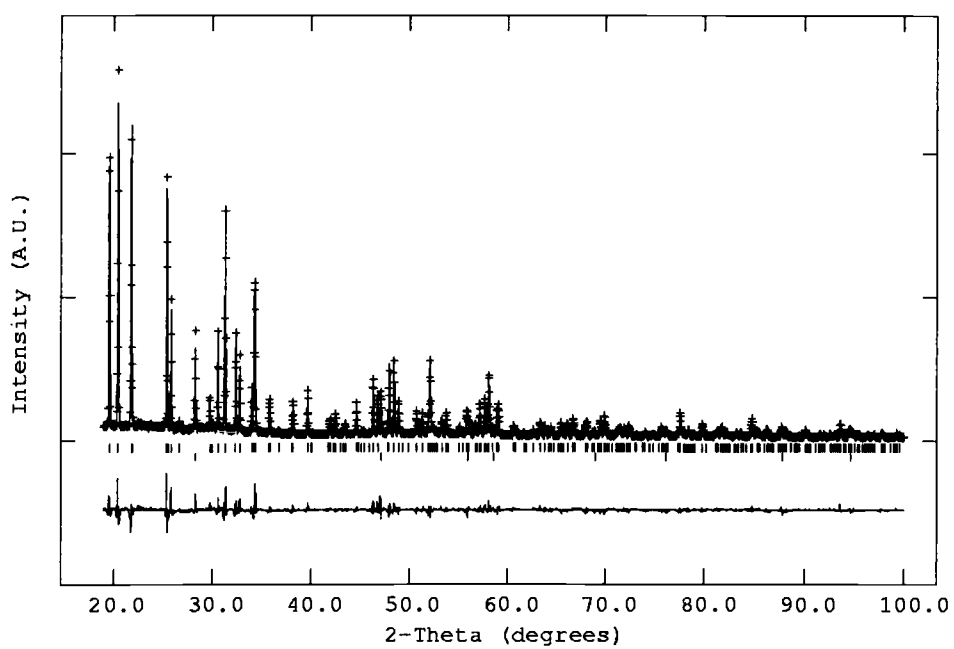


Figure 5.4.b. Observed, calculated, and difference profiles for orthorhombic TaOVO₄ at 600 °C

5.6. Discussion

The orthorhombic TaOVO₄ compound exhibits negative thermal expansion for all cell dimensions over the entire temperature range studied. The variations of each cell edge length with temperature are shown in Figures 5.5 and 5.6. The thermal expansion coefficients are given in Table 5.3.

Table 5.3. Thermal Expansion Coefficients for Orthorhombic TaOVO₄

Parameter	α ($^{\circ}\text{C}^{-1}$)
a	-6.22×10^{-6}
b	-4.69×10^{-6}
c	-4.49×10^{-6}
Volume	-1.54×10^{-5}
α_1	-5.13×10^{-6}

The negative thermal expansion seen in this material can be attributed to the rotations of the corner-shared octahedra and tetrahedra. Since all cell dimensions decrease with increasing temperature, it is possible that rocking motions occur in all dimensions. Figure 5.7 depicts the polyhedra viewed along the *ab* and *ac* planes. The atomic positions as a function of temperature are listed in Tables 5.4 - 5.6.

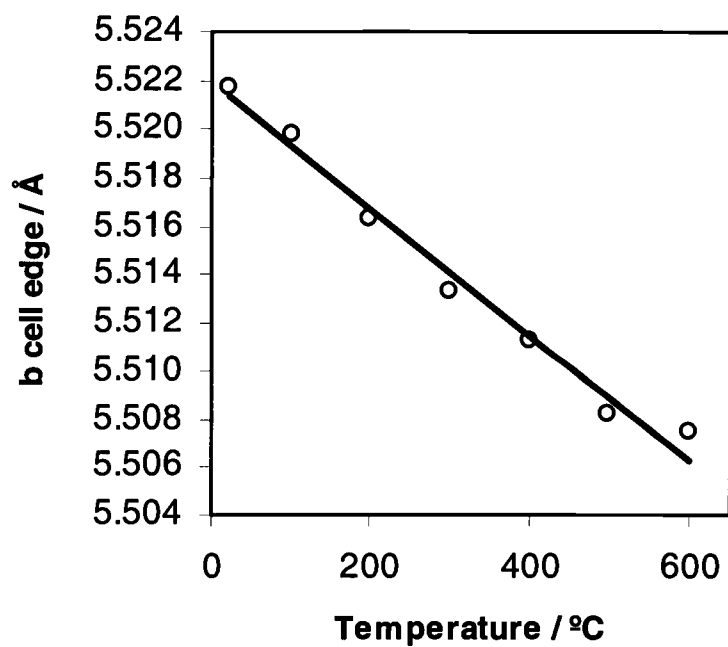
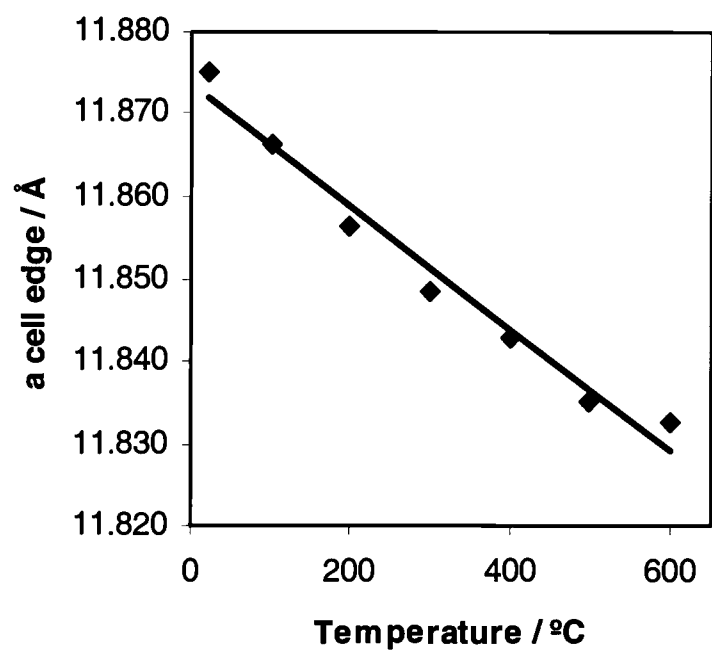


Figure 5.5. Changes in *a* and *b* cell edges as a function of temperature

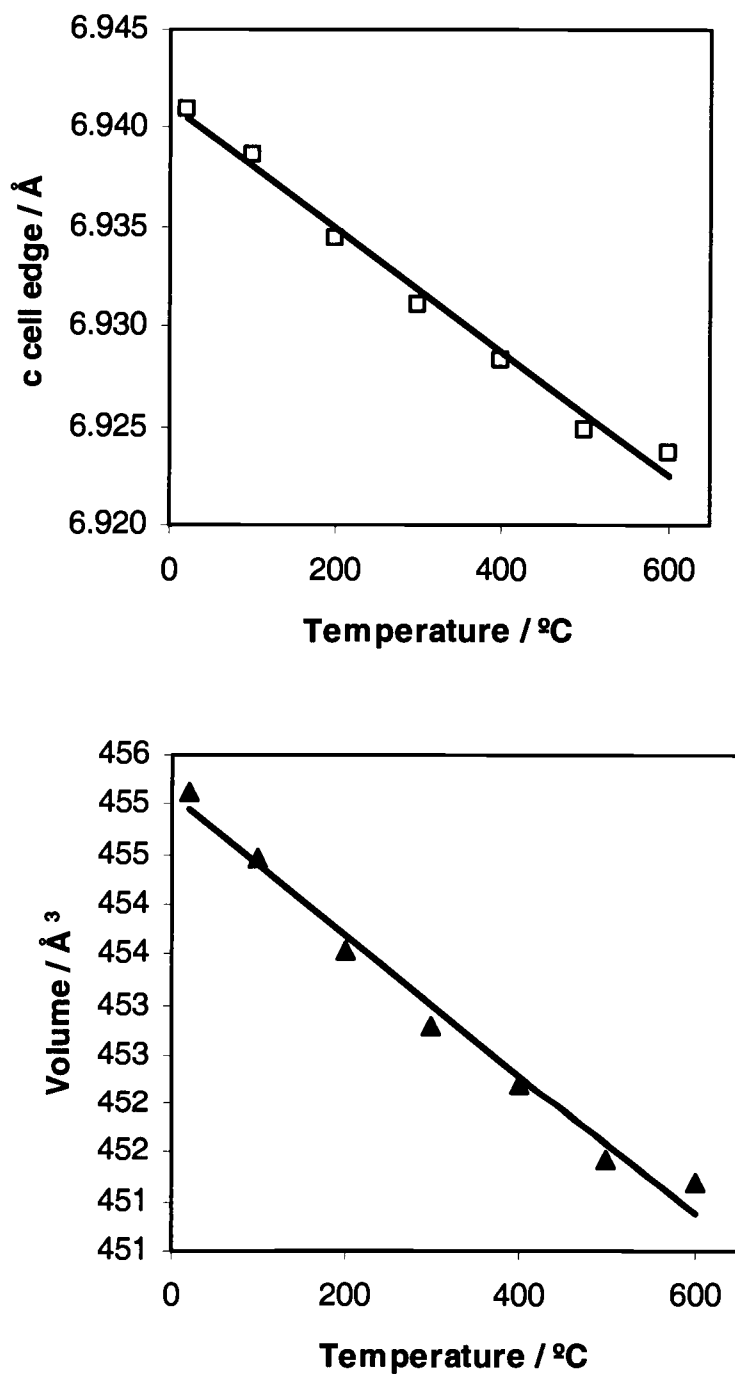


Figure 5.6. Changes in c and volume as a function of temperature

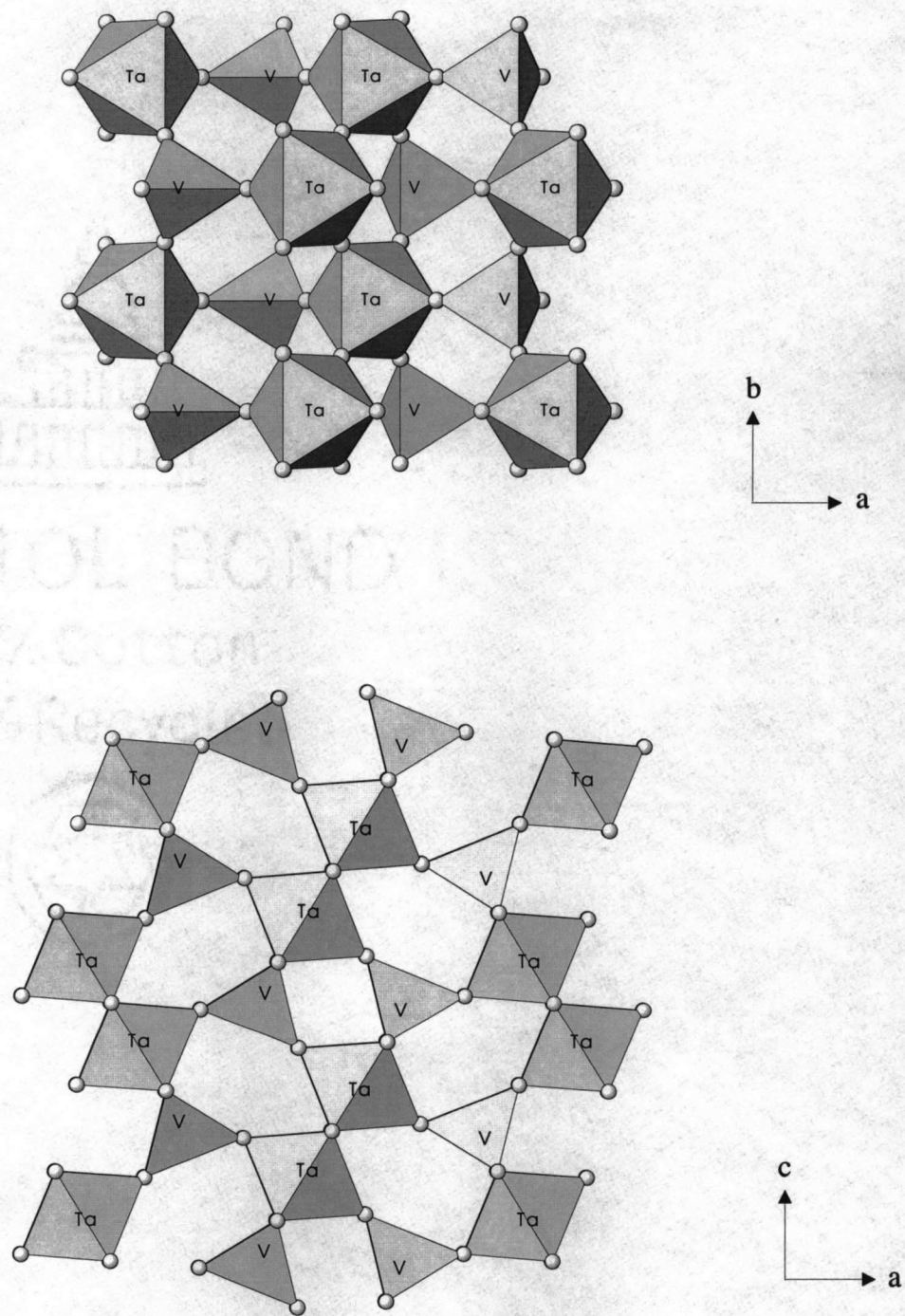


Figure 5.7. Polyhedra connectivity along the ab and ac planes

Table 5.4. Variation of Metal Atom Positions with Temperature

Temp (°C)	x (Ta)	z (Ta)	x (V)	z (V)
20	0.0593(1)	0.3437(2)	0.3467(4)	0.5320(7)
100	0.0593(1)	0.3442(2)	0.3470(4)	0.5296(6)
200	0.0590(1)	0.3438(2)	0.3478(4)	0.5297(7)
300	0.0590(1)	0.3435(2)	0.3475(4)	0.5317(7)
400	0.0591(1)	0.3436(2)	0.3460(4)	0.5322(7)
500	0.0588(1)	0.3436(2)	0.3467(4)	0.5322(7)
600	0.0589(1)	0.3437(2)	0.3459(4)	0.5309(7)

Table 5.5. Variation of O(2) Atom Positions with Temperature

Temp (°C)	x (O2)	y (O2)	z (O2)
20	0.1249(8)	-0.013(2)	0.152(2)
100	0.1256(8)	-0.012(2)	0.148(2)
200	0.1226(9)	-0.015 (2)	0.151(2)
300	0.1262(9)	-0.008(2)	0.148(2)
400	0.1235(9)	-0.016(2)	0.149(2)
500	0.1246(9)	-0.010(2)	0.154(2)
600	0.1244(9)	-0.006(2)	0.155(2)

Table 5.6. Variation of O(3) and O(4) Atom Positions with Temperature

Temp (°C)	x (O3)	z (O3)	x (O4)	z (O4)
20	0.200(1)	0.473(2)	0.423(1)	0.321(2)
100	0.203(1)	0.486(2)	0.419(1)	0.319(2)
200	0.201(1)	0.479(2)	0.417(1)	0.319(2)
300	0.204(1)	0.484(2)	0.416(1)	0.321(2)
400	0.204(1)	0.487(2)	0.418(1)	0.324(2)
500	0.207(1)	0.485(2)	0.421(1)	0.323(3)
600	0.211(1)	0.486(2)	0.416(1)	0.329(3)

The isotropic thermal vibrations were determined for the metal atoms only. The oxygen UISO values were fixed at 0.025 \AA^2 . The UISO values for the tantalum atoms are lower than that of the vanadium atom, consistent with the idea that heavier atoms do not vibrate as much as lighter ones (Figure 5.8). As would be expected, the thermal vibration values increase with increasing temperature.

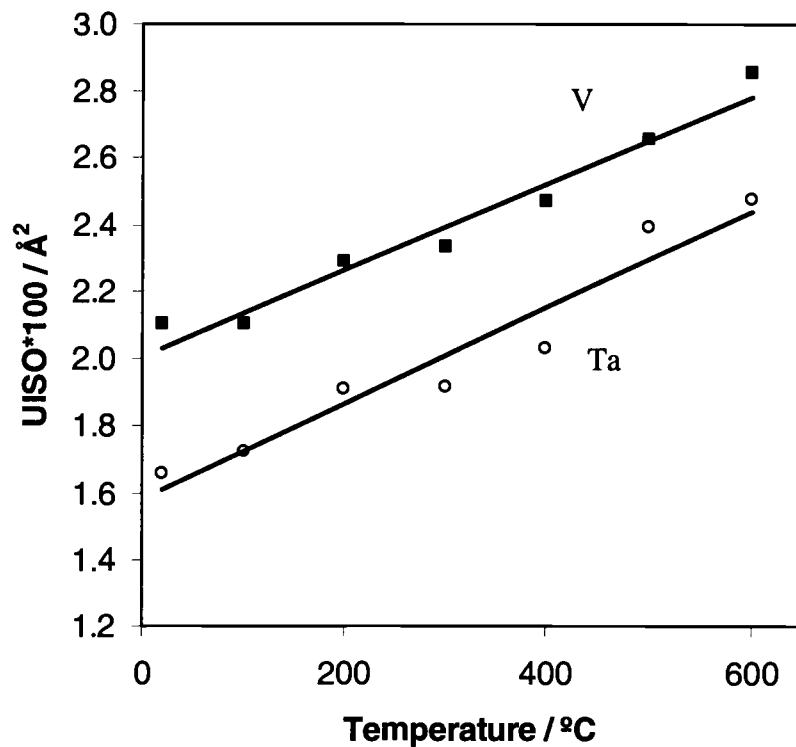


Figure 5.8. Variation of isotropic thermal parameters with temperature

Inspection of the changes in bond length with temperature shows that the V-O bonds are converging to an approximate value of 1.63 Å as the temperature is increased (Figure 5.9 a). This is smaller than the sum of the Shannon radii which would give a V-O bond distance of 1.705 Å. Similarly, three of the four unique Ta-O bond lengths are converging to a value close to 2.05 Å (Figure 5.9 b). This indicates that the polyhedra are becoming more regular as the temperature increases. Distance least squares calculations show an increase in

cell dimensions when no rocking motion is accounted for. If the Ta-O bond distances are set to 1.99 Å and the V-O bond distances equal to 1.705 Å, minimization of the residual leads to cell dimensions that increase to values of $a = 11.91$ Å, $b = 5.60$ Å, and $c = 6.99$ Å (compared to $a = 11.87$ Å, $b = 5.52$ Å, and $c = 6.94$ Å found at room temperature).

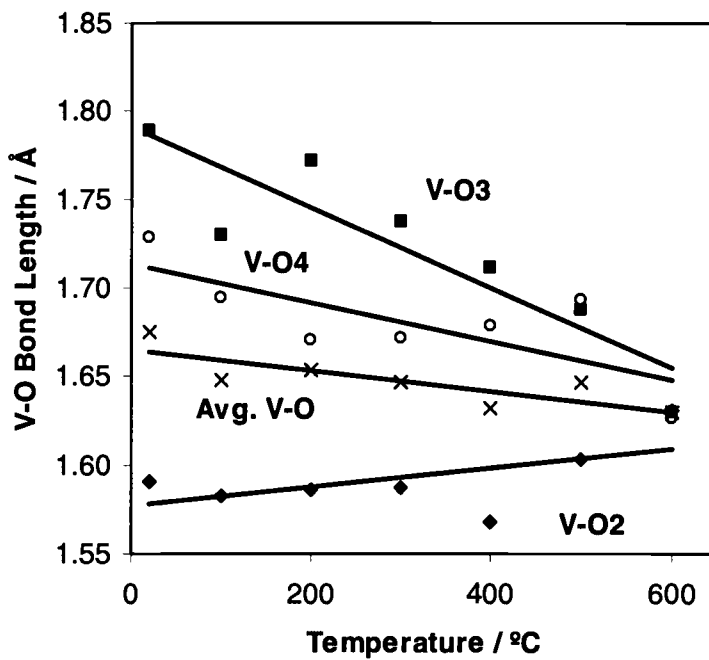


Figure 5.9.a. Variation of V-O bond lengths with temperature

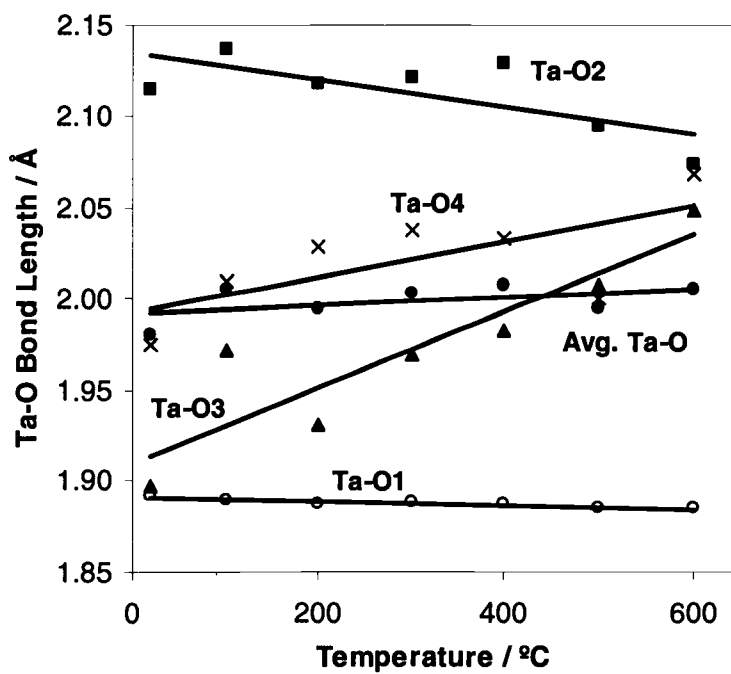


Figure 5.9.b. Variation of Ta-O bond lengths with temperature

The changes in the Ta-O bonds (with the exception of the Ta-O(1) bond) have oxygen atoms connected to VO_4 tetrahedra. The O(1) atom connects adjacent TaO_6 octahedra together. The Ta-O(1) bond length shows relatively little change over the temperature range. Therefore, it seems reasonable to conclude that the changes seen in the Ta-O bond lengths are dominated by the VO_4 tetrahedra becoming more regular. Figure 5.10 shows the bridging oxygen atoms for the polyhedral linkages.

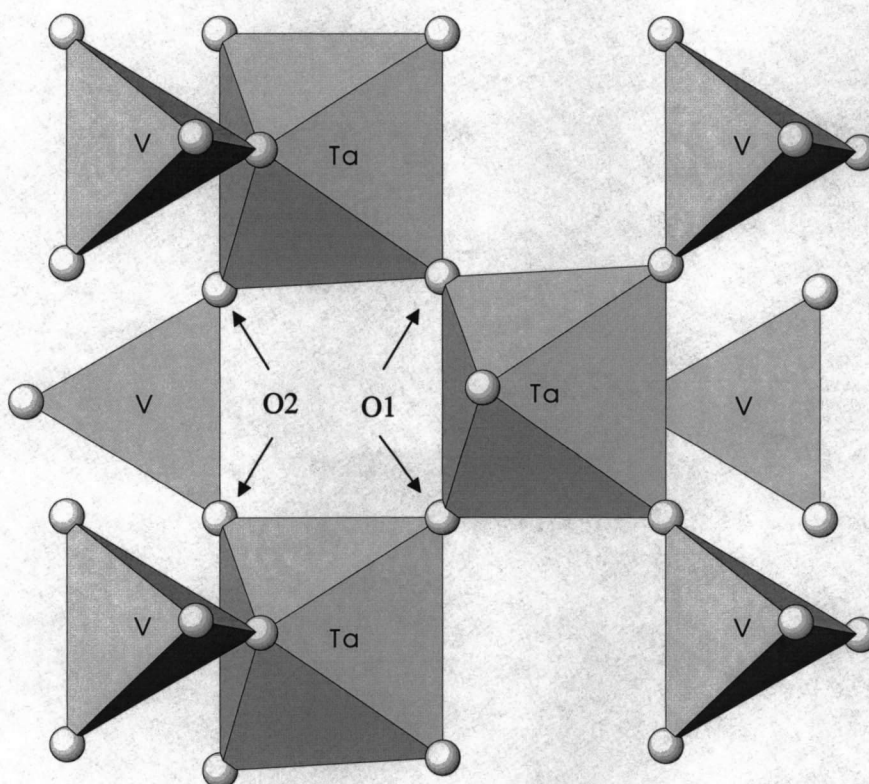


Figure 5.10. Bridging oxygen atoms in the polyhedra linkages

In a review of compounds that contract on heating (8), Sleight reported on mechanisms for negative thermal expansion. The PbTiO_3 compound exhibits negative thermal expansion and it has been suggested that the mechanism involves the polyhedra becoming more regular. This compound has distorted TiO_6 octahedra with short and long Ti-O bonds. These become more equal as the temperature is increased. While the orthorhombic TaOVO_4 compound has VO_4 polyhedra becoming more regular, the distortion seen in the TaO_6 octahedra becomes greater. This can be seen by inspection of Table 5.7. The long Ta-O bonds elongate and the short Ta-O bonds become slightly smaller at elevated temperatures. This is consistent with the idea that weaker bonds show more thermal expansion than stronger ones.

Table 5.7. Variation of Selected Bond Distances (\AA) with Temperature

Temp. ($^{\circ}\text{C}$)	[2] Ta-O1	[2] Ta-O2	Ta-O3	Ta-O4
20	1.892(1)	2.115(1)	1.897(2)	1.975(2)
100	1.889(1)	2.137(1)	1.972(2)	2.010(2)
200	1.888(1)	2.118(1)	1.931(2)	2.029(2)
300	1.888(1)	2.121(1)	1.970(2)	2.038(2)
400	1.887(1)	2.129(1)	1.983(2)	2.033(2)
500	1.885(1)	2.095(1)	2.008(2)	2.001(2)
600	1.885(1)	2.074(1)	2.049(2)	2.069(2)

This orthorhombic structure still represents a three-dimensional network structure that exhibits negative thermal expansion and this can be attributed to the tilting motions of the corner-shared polyhedra. Figure 5.11 depicts one rocking motion in the bc plane that would result in a decrease of the b and c cell edges.

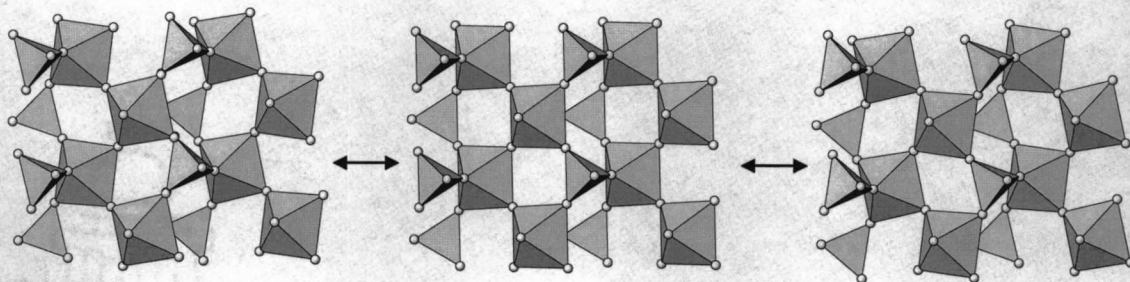


Figure 5.11. Possible polyhedral tilt that results in negative thermal expansion

5.7. TaAs_xV_{1-x}O₅ Solid Solutions

5.7.1. Experimental

Ternary oxides of the general formula TaAs_xV_{1-x}O₅ ($0 < x < 0.5$) have been synthesized by solid state reaction with tantalum oxide (Alfa-Aesar, 99%), ammonium vanadate (Alfa-Aesar, 99%), and ammonium arsenate (Alfa-Aesar, 98%) as starting materials. These are isomorphous with the binary orthorhombic TaOVO₄ and TaOAsO₄ compounds. Synthesis above this substitution range resulted in a mixture of As₂O₅ and TaOVO₄ phases. No previous studies have reported this solid solution. Stoichiometric amounts of the starting materials were ground in an agate mortar and pestle and then transferred to an alumina crucible. This mixture was heated at 300 °C for 4 hours to decompose the ammonium salts and subsequently heated at a final reaction temperature of 800 °C for 12 hours.

Powder diffraction measurements were collected on a Siemens D5000 diffractometer with vertical Soller slits and an energy dispersive Kevex detector, using Cu K α radiation. The observed diffraction patterns were indexed on an orthorhombic unit cell.

LeBail refinements were carried out to determine accurate cell dimensions. A total of 12 variables were refined: 6 background coefficients, zero point, 2 profile coefficients, and cell dimensions.

5.7.2. Results and Discussion

The cell dimensions as a function of arsenic composition are plotted in Figure 5.12. There is a 2.4 % decrease in the a cell dimension between the two end members, orthorhombic TaOVO₄ and TaOAsO₄. The b and c cell dimensions decrease by 3.0 and 3.2 %, respectively. The tetrahedrally coordinated V⁵⁺ and As⁵⁺ ions have crystal radii of 0.355 and 0.335 Å (9). The decrease in the overall cell dimensions can be accredited to the slight decrease in the As⁵⁺ radius as it substitutes into the lattice.

5.7.3. Thermal Expansion Properties of TaAs_{0.1}V_{0.9}O₅

This solid solution member of the Ta-As-V-O system was prepared and the structural changes as a function of temperature were measured with X-ray diffraction. Diffraction data were collected with a Si internal standard (NIST SRM 640b) on an INEL diffractometer. Measurements were collected in 100 °C increments from room temperature to 500 °C.

Rietveld refinements were carried out for each temperature. At 25 °C, the scale, zero point, background coefficients, phase fractions, atom coordinates, and metal atom thermal parameters were refined. A preferred orientation variable was also introduced corresponding to the (010) direction for the TaAs_{0.1}V_{0.9}O₅ phase. Linear restraints were incorporated to correlate the atomic coordinates, thermal parameters, and fractions of the As and V atoms. Fractions of 0.918 for V and 0.082 for As atoms were determined at room temperature and were fixed for

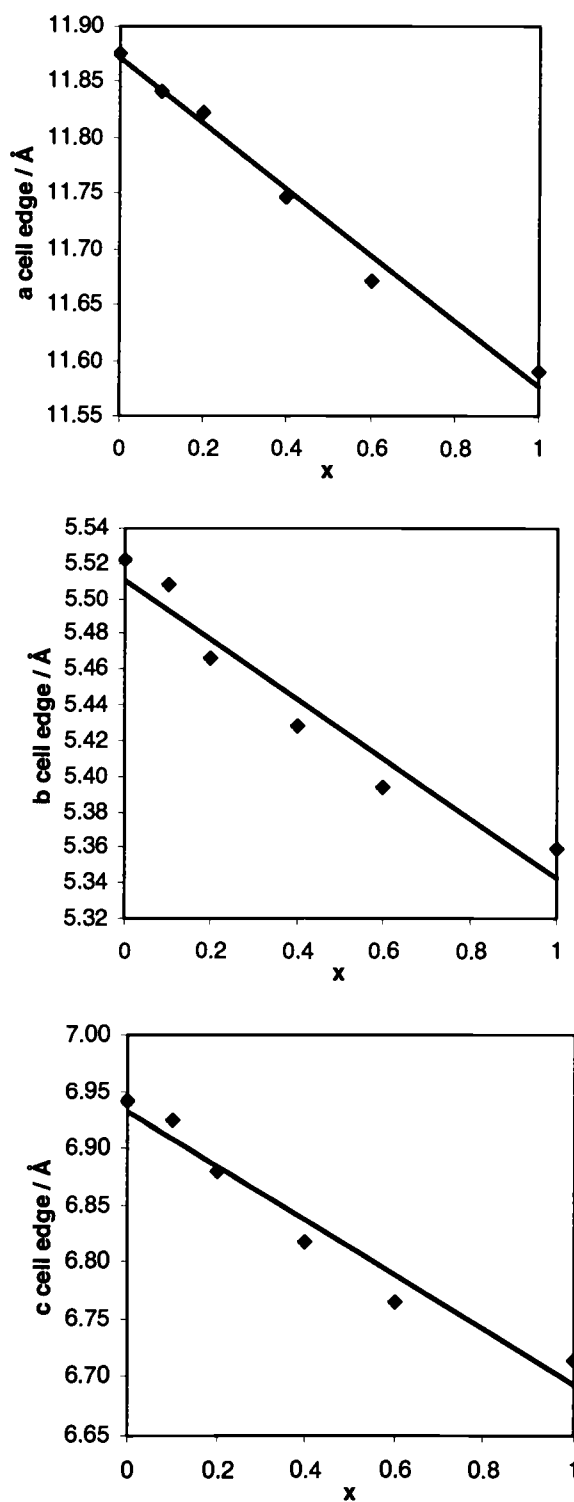


Figure 5.12. Cell dimensions as a function of As concentration, x

higher temperatures. Table 5.8 shows the refinement statistics at each temperature.

Table 5.8. Refinement Statistics for TaAs_{0.1}V_{0.9}O₅

Temp. (°C)	χ^2	wRp	Rp
20	3.097	0.1068	0.0834
100	4.735	0.0847	0.0672
200	3.244	0.0952	0.0753
300	3.300	0.0995	0.0778
400	4.295	0.1029	0.0875
500	5.079	0.1098	0.0934

Similar to the orthorhombic TaOVO₄ compound, this solid solution member also exhibits negative thermal expansion. Figures 5.13 and 5.14 show the changes in the cell dimensions and volume as a function of temperature. The thermal expansion coefficients are listed in Table 5.9.

Table 5.9. Coefficients of Thermal Expansion for TaAs_{0.1}V_{0.9}O₅

Parameter	α (°C ⁻¹)
a	-7.51×10^{-6}
b	-4.72×10^{-6}
c	-5.32×10^{-6}
Volume	-1.75×10^{-5}
α_1	-5.83×10^{-6}

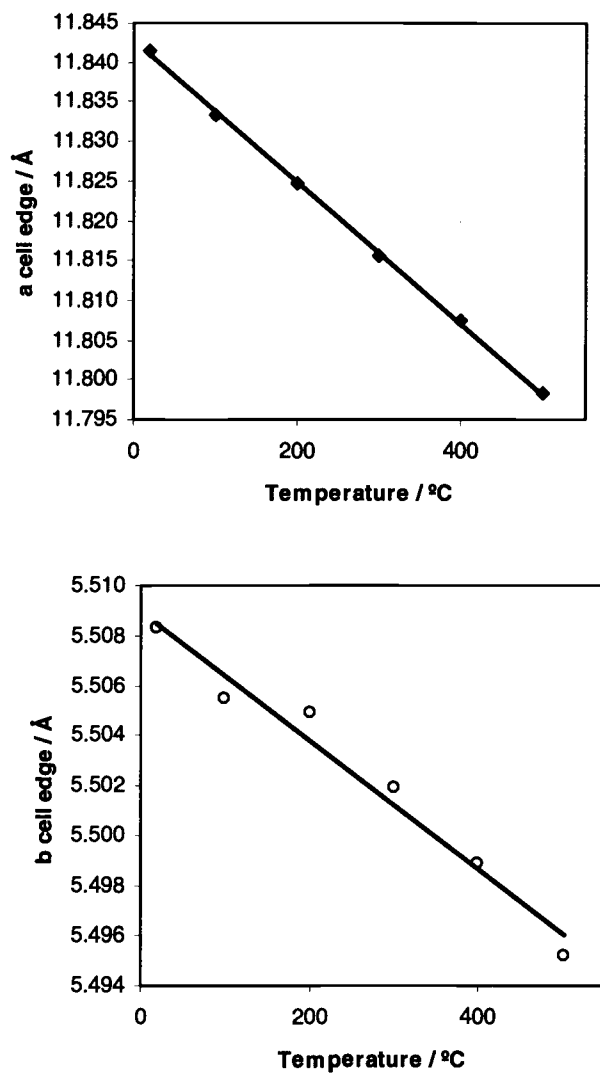


Figure 5.13. Variation of *a* and *b* cell edges with temperature

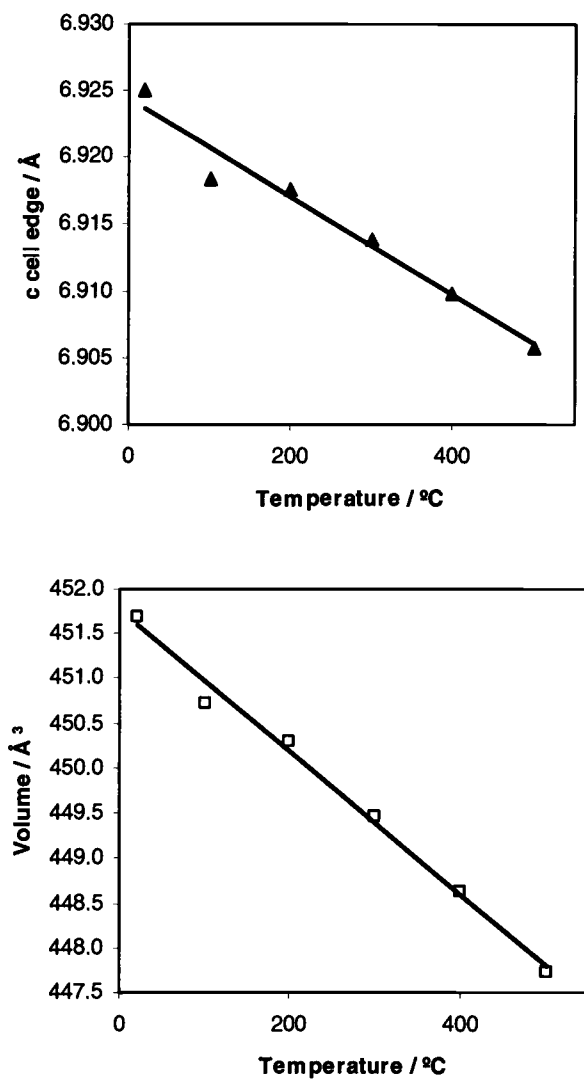


Figure 5.14. Variation of *c* cell edge and volume with temperature

The same trend seen in the metal-oxygen bond distances of the orthorhombic TaOVO_4 is apparent in the solid solution member (Figure 5.15). The average M-O bond distance (M = V, As) decreases slightly, while the Ta-O bond distance increases as the temperature is raised.

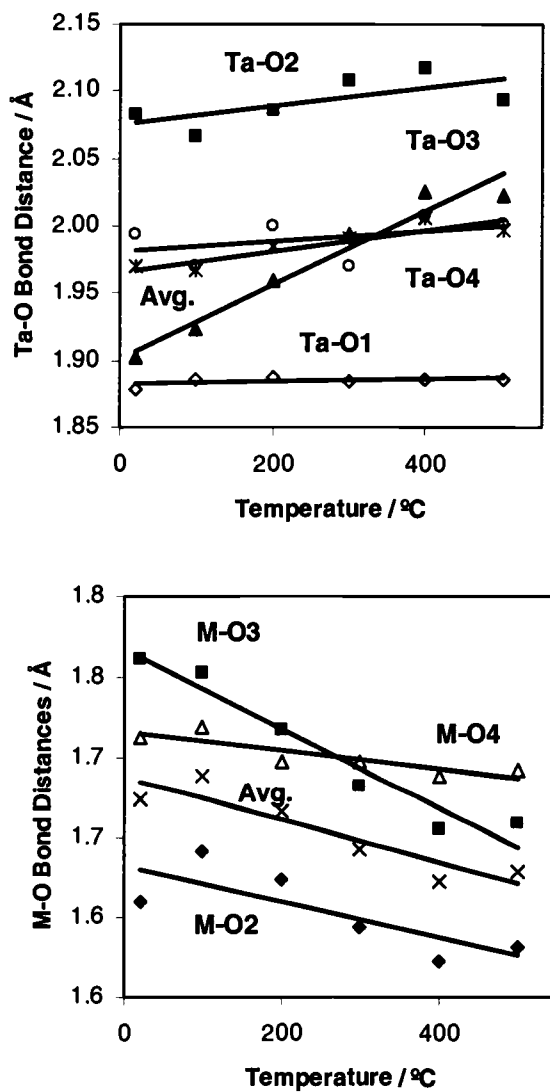


Figure 5.15. Variation of metal-oxygen bond lengths with temperature

A differential scanning calorimetry measurement was performed from room temperature to $-120\text{ }^{\circ}\text{C}$. This solid solution member did not show a transition like that found in the orthorhombic TaOVO_4 compound. This phase transition suppression is presumably due to the disorder on the M cation site.

Since this compound is isostructural with orthorhombic TaOVO_4 , the tilting polyhedra mechanism can be applied to this structure to explain the negative thermal expansion seen in this phase.

5.8. References

1. Jesse Jefferson Brown, Jr., Ph.D. Thesis, Pennsylvania State University, 1964
2. Jesse J. Brown and F. A. Hummel, *Trans. Brit. Ceram. Soc.*, 64, 419 (1965)
3. C. N. Chu, N. Saka and N. P. Suh, *J. Engin. Mater. Tech.*, 108, 275 (1986)
4. H. Chahboun, D. Groult B. and Raveau, *Mat. Res. Bull.*, 23, 805 (1988)
5. A. Leclaire, H. Chahboun, D. Groult and B. Raveau, *Z. Krist.*, 177, 277 (1986)
6. A. C. Larson and R. B. von Dreele, LANSCE, Los Alamos National Laboratory, Los Alamos, N.M., 1994
7. A. LeBail, H. Duroy and J. L. Fourquet, *Mat. Res. Bull.*, 23, 447 (1988)
8. A. W. Sleight, *Inorg. Chem.*, 37(12), 2854 (1998)
9. R. D. Shannon, *Acta Cryst.*, A32, 751 (1976)

Chapter 6

A Comparative Analysis of AOMO₄ Structures and Future Work

6.1. Polymorphs

The members of the AOMO₄ family studied in this thesis work crystallize in two structure types and 4 polymorphs [tetragonal (*P4/n*, *P4/nmm*), orthorhombic (*Pnma*) and monoclinic (*P2₁/c*)]. All consist of a three dimensional network built of corner shared AO₆ octahedra and MO₄ tetrahedra. The tetragonal polymorph contains AO₆ octahedra connected together on opposite corners to give a chain along a crystallographic axis. Each AO₆ chain is connected to another AO₆ chain by PO₄ tetrahedra. A view of this connectivity is shown in Figure 6.1.

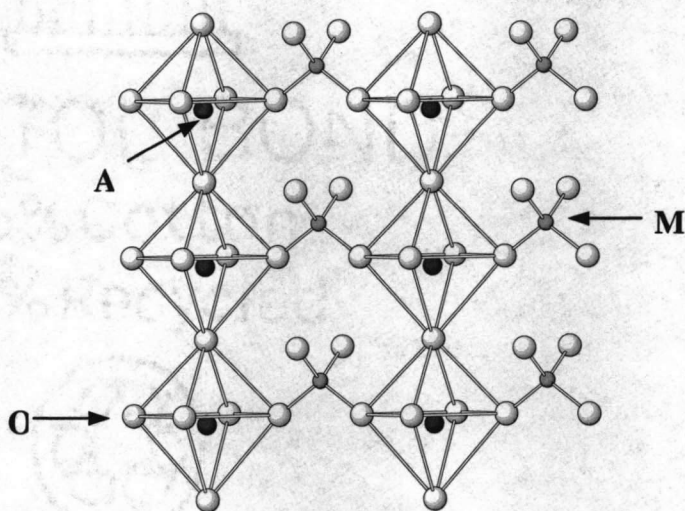


Figure 6.1. Chains of corner-shared polyhedra in tetragonal AOMO₄ compounds

In the monoclinic and orthorhombic structures, the AO_6 octahedra are connected on adjacent oxygen atoms to give a zig-zag chain of AO_6 octahedra. These chains are then coupled together with MO_4 tetrahedra. Figures 6.2 and 6.3 show the polyhedra connectivity for the monoclinic and orthorhombic polymorphs.

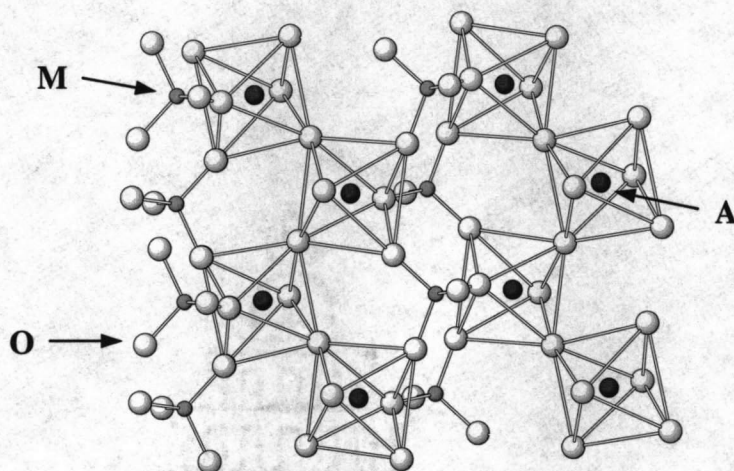


Figure 6.2.a. Chains of corner-shared polyhedra in monoclinic AOMO_4 compounds

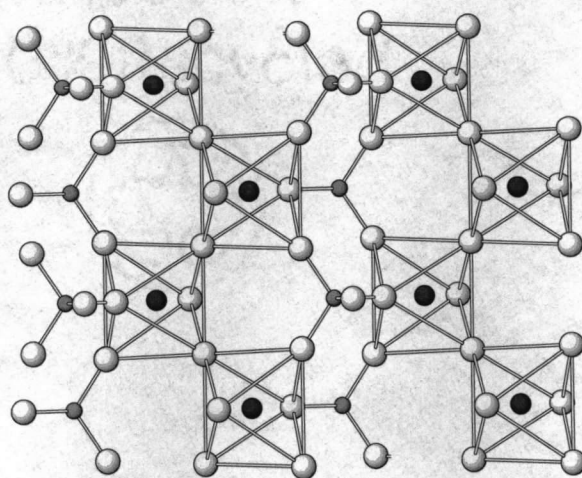


Figure 6.2.b. Chains of corner-shared polyhedra in orthorhombic AOMO_4 compounds

6.2. Octahedral Distortions

Kuntz and Brown (1) have examined the frequency of observed octahedral distortion associated with d^0 transition metal centers. They conclude that the distortion increases with increasing formal charge and decreases with increasing size of the cation. In addition to the electronic structure of the cation, other factors affect the structural distortion such as the bonding network, cation-cation repulsion, and lattice constraints or stresses. The $AOMO_4$ structures contain distorted metal-oxygen (AO_6) octahedra where the cation is displaced from the center of the octahedron. There is no strong contribution from cation-cation repulsion since there are only corner-shared polyhedra. There is lattice stress in the tetragonal structures since the axes lengths are determined by both the length of the axial A-O bonds and by the spacing between the MO_4 tetrahedra. The connectivity of the more covalent tetrahedra to the octahedra gives rise to different magnitudes of distortion for the monoclinic and orthorhombic structures. The octahedra are less distorted in the tetragonal $TaOPO_4$ structure compared to the niobium analog. This is a direct result of the more covalent Nb-O bond since the radii of Ta^{5+} and Nb^{5+} are essentially equal (2). An example of this is also seen in the isomorphous structures of $LiNbO_3$ (3) and $LiTaO_3$ (4). These contain distorted AO_6 octahedra. The octahedra in $LiTaO_3$ have two different distances Ta-O of 1.890 and 2.068 Å, whereas the Nb atom is displaced slightly more to give Nb-O distances of 1.889 and 2.112 Å in $Li NbO_3$.

6.3. Phase Transitions

The structures of several members in the $AOMO_4$ family have been investigated as a function of temperature. Each compound studied was found to undergo a structural phase transition with the exception of a solid solution member in the Ta-V-As-O system. Table 6.1 shows the phases and transition temperatures found in each of the investigated systems.

Table 6.1. Phase Transitions of the Investigated Systems

Low Temperature Phase (Space Group)	Phase Transition Temperature (°C)	High Temperature Phase (Space Group)
Tetragonal $NbOPO_4$ (P4/n)	~200	Tetragonal $NbOPO_4$ (P4/nmm)
Monoclinic $NbOPO_4$ (P2 ₁ /c)	290	Orthorhombic $NbOPO_4$ (Pnma)
Monoclinic $TaOVO_4$ (P2 ₁ /c) (uncharacterized)	- 20	Orthorhombic $TaOVO_4$ (Pnma)
Tetragonal $TaOPO_4$ (P4/n)	~200	Tetragonal $TaOPO_4$ (P4/nmm)

No phase transition was detected for the solid solution member $TaAs_{0.1}V_{0.9}O_5$. This compound is isostructural with the orthorhombic $TaOVO_4$ structure. The As^{5+} ion substitutions distributed randomly over the V^{5+} sites introduce disorder in this structure. This disorder affects the entropy of the system that lowers the phase transition temperature. Similar transition

temperature depression has also been reported for the $\text{ZrV}_{2-x}\text{P}_x\text{O}_7$ series (5). This effect is analogous to the observance of freezing point depression seen with the addition of a nonvolatile solute to a solvent.

Negative thermal expansion (NTE) is seen in all of the high temperature phases. The mechanism associated with this effect involves tilting corner-shared polyhedra back and forth within certain crystallographic planes that results in cell edge contraction. At lower temperatures, the rocking motion of the polyhedra results in a lowering of symmetry and this is locked in below the phase transition temperature. Of these compounds, the orthorhombic TaOVO_4 shows the most remarkable NTE. This is related to the larger polyhedra (due to the larger cations) having the ability for more facile rocking motion and possibly the effect of the polyhedra becoming more regular at higher temperatures. The latter mechanism has been described for the PbTiO_3 compound (6). Table 6.2 shows the relative volume of the polyhedra in each of the high temperature polymorphs.

Table 6.2. Polyhedra Volumes (\AA^3) for the High Temperature Polymorphs

AOMO ₄ Structure	Temp. (°C)	Data	Space Group	AO ₆ Volume (\AA^3)	MO ₄ Volume (\AA^3)
NbOPO ₄	200	Neutron	P4/nmm	11.989	1.816
NbOPO ₄	325	Neutron	Pnma	9.799	1.848
TaOPO ₄	200	X-ray	P4/nmm	11.609	1.714
TaOVO ₄	25	X-ray	Pnma	10.118	2.49

Table 6.3 shows some common materials with their corresponding thermal expansion coefficients. A typical polymer has a very high thermal expansion coefficient due to their weak secondary intermolecular bonds. The ZrW_2O_8 material has gained considerable interest due to the isotropic negative thermal contraction over a large temperature range. The compounds studied in this thesis work are represented in bold.

Most of the members have been used in a variety of applications thus far, mostly focusing on their intercalation abilities. This thesis work presents the first comparative analysis on the thermal contraction properties of these compounds.

Table 6.3. Thermal Expansion Coefficients

Material	α_1 (10^{-6})/ $^{\circ}\text{C}$	Ref.
Polypropylene	145	7
Copper	17.0	7
Al_2O_3	7.6	7
NbOPO₄ (P4/nmm)	6.0	this work
TaOPO₄ (P4/nmm)	-0.6	this work
NbOPO₄ (Pnma)	-3.7	this work
TaOVO₄ (Pnma)	-5.8	this work
TaAs_{0.1}V_{0.9}O₅	-5.8	this work
ZrW_2O_8	-9.1	8
AlPO_4 -17	-11.7	9

6.4. Suggestions for Future Work

There are many AOMO_4 compounds that remain uncharacterized as a function of temperature and have the potential to exhibit negative thermal expansion. The substitution of pentavalent cations such as V^{5+} , Sb^{5+} , As^{5+} , Mo^{5+} can be explored as well as cation couples such as $\text{Ti}^{4+}/\text{S}^{6+}$, $\text{V}^{4+}/\text{Mo}^{6+}$, and $\text{V}^{4+}/\text{S}^{6+}$. The synthesis of some of these compounds have been reported however, some remain unprepared. With the similar crystal systems of many of the AOMO_4 members, a limited or complete range of solid solutions might form. Determination of the effects of solid solution substitution on thermal expansion offers another wide avenue of experiments. Particularly interesting are the solid solution members of the Ta-V-P-O system. This system is complex due to the

fact that V^{5+} can substitute onto both the octahedral Ta^{5+} and the tetrahedral P^{5+} sites.

The members of the $AOMO_4$ family exhibit interesting crystal chemistry characteristics. This thesis work investigates the correlation of these features with their negative thermal expansion properties. It is important in the development of a systematic effort to understanding of the structure-property requirements in these NTE materials. Work towards advancement of the applications can be facilitated with the understanding of the fundamental science governing this behavior.

6.5. References

1. M. Kuntz and D.I. Brown, *J. Solid State Chem.*, 115, 395 (1995)
2. R. D. Shannon, *Acta Cryst.*, A32, 751 (1976)
3. S. C. Abrahams, J. M. Reddy, and J. L. Bernstein, *J. Phys. Chem. of Solids*, 27, 997 (1966)
4. S. C. Abrahams and J. L. Berstein, *J. Phys. Chem. of Solids*, 28, 1685 (1967)
5. V. Korthius, N. Khosrovani, A. W. Sleight, N. Roberts, R. Dupree and W. W. Warren Jr., *Chem. Mater.*, 7, 412 (1995)
6. A. W. Sleight, *Inorg. Chem.*, 37, 2854 (1998)
7. William D. Callister, Jr. *Materials Science and Engineering, An Introduction*; John Wiley & Sons: NY, 1985; p. 492
8. J. S. O. Evans, W. I. F. David and A. W. Sleight, *Acta Cryst. Sect. B.*, 55, 333 (1999)
9. Martin P. Attfield and Arthur W. Sleight, *Chem. Mater.*, 10, 2013 (1998)

Bibliography

- S. C. Abrahams and J. L. Bernstein, *J. Phys. Chem. of Solids*, 28, 1685 (1967)
- S. C. Abrahams, J. M. Reddy, and J. L. Bernstein, *J. Phys. Chem. of Solids*, 27, 997 (1966)
- Jose-Manuel Amarilla, Blanca Casal, Juan-Carlos Galvan and Eduardo Ruiz-Hitzky, *Chem. Mater.*, 4, 62 (1992)
- J. M. Amarilla, B. Casal, J. C. Galvan and E. Ruiz-Hitzky, *Mater. Sci. Forum*, 91-93, 153 (1992)
- J. M. Amarilla, B. Casal and E. Ruiz-Hitzky, *Mat. Letters*, 8, 132 (1989)
- J. M. Amarilla, B. Casal and E. Ruiz-Hitzky, *J. Solid State Chem.*, 99, 258 (1992)
- J. M. Amarilla, B. Casal and E. Ruiz-Hitzky, *J. Mater. Chem.*, 6(6), 1005, (1996)
- S. Arsalane, R. Brochu, J. Chassaing and M. Quarton, *J. Chim. Phys. Phys.-Chim. Biol.*, 88(10), 1951 (1991)
- Martin P. Attfield and Arthur W. Sleight, *Chem. Mater.*, 10, 2013 (1998)
- K. Beneke and G. Lagaly, *Inorg. Chem.*, 22, 1503 (1983)
- L. Benes, R. Hyklova, J. Kalousova and J. Votinsky, *Inorg. Chim. Acta*, 177, 71 (1990)
- L. Benes, K. Melanova, V. Zima, J. Kalousova and J. Votinsky, *Inorg. Chem.*, 36, 2850 (1997)
- Ludvik Benes, Klara Melanova and Vitezslav Zima, *J. Solid State Chem.*, 151, 255 (2000)
- Ludvik Benes, Klara Melanova, Vitezslav Zima, Jaroslava Kalousova and Jiri Votinsky, *J. Inclusion Phenom. Mol. Recognit. Chem.*, 31(3), 275 (1998)
- Ludvik Benes, Klara Melanova, Vitezslav Zima and Jiri Votinsky, *J. Solid State Chem.*, 141(1), 64 (1998)
- Ludvik Benes and Vitezslav Zima, *Sci. Pap. Univ. Pardubice, Ser. A*, 2, 121 (1996)

L. Benes, J. Votinsky, J. Kalousova and K. Handlir, *Inorg. Chim. Acta*, 176, 255 (1990)

L. Benes, J. Votinsky, J. Kalousova and J. Klikorka, *Inorg. Chim. Acta*, 114, 47 (1986)

Jesse Jefferson Brown, Jr., Ph.D. Thesis, Pennsylvania State University, 1964
Jesse J. Brown and F. A. Hummel, *Trans. Brit. Ceram. Soc.*, 64, 419 (1965)

S. Bruque, M. Martinez Lara, L. Moreno, T. Ramirez-Cardenas, J. Chaboy, M. Marziali and S. Stizza, *J. Solid State Chem.*, 114(2), 317 (1995)

William R. Busing and Henri A. Levy, *Acta Cryst.*, 17, 142 (1964)

William D. Callister, Jr. *Materials Science and Engineering, An Introduction*; John Wiley & Sons: NY, 1985; p. 492

H. Chahboun, D. Groult, M. Hervieu and B. Raveau, *J. of Solid State Chem.*, 65, 331 (1986)

H. Chahboun, D. Groult and B. Raveau, *Mat. Res. Bull.*, 23, 805 (1988)

N. G. Chernorukov, N. P. Egorov and I. A. Korshunova, *Inorg. Mater.*, 15, 1722 (1979)

N. G. Chernorukov, N.P. Egorov and I. A. Korshunov, *Zh. Neorg. Khim.*, 23, 2672 (1978)

N. G. Chernorukov, N. P. Egorov and I. A. Korshunov, *Izv. Akad. Nauk SSSR, Neorg. Mater.*, 15(2), 335 (1979)

N. G. Chernorukov, N.P. Egorov, E.V. Shitova and Yu. I. Chigirinskii, *Russ. J. Inorg. Chem.*, 26 (10), 1454 (1981)

C. N. Chu, N. Saka and N. P. Suh, *J. Engin. Mater. Tech.*, 108, 275 (1986)

B. D. Cullity *Elements of X-ray Diffraction*; Addison-Wesley Publishing: Reading, MA, 1978; p. 284

A. Datta, S. Bhaduri, R. Y. Kelkar and H. I. Khwaja, *J. Phys. Chem.*, 98, 11811 (1994)

W. A. Dollase, *J. Appl. Cryst.*, 19, 267 (1986)

- M. T. Dove, V. Heine and K. D. Hammonds, *Mineral. Magn.*, 59, 629 (1995)
- Harry Eick and Lars Kihlberg, *Acta Chem. Scand.*, 20, 722 (1966)
- J. S. O. Evans, W. I. F. David and A. W. Sleight, *Acta Cryst. Sect. B.*, 55, 333 (1999)
- John S. O. Evans and T. A. Mary, *Inter. J. Inorg. Mater.*, 2, 143 (2000)
- J. S. O. Evans, T. A. Mary and A. W. Sleight, *J. Solid State Chem.*, 133, 580 (1997)
- J. S. O. Evans, T. A. Mary and A. W. Sleight, *J. Solid State Chem.*, 137, 148 (1998)
- J. S. O. Evans, T. A. Mary, T. Vogt, M. A. Subramanian and A. W. Sleight, *Chem. Mater.*, 8, 2809 (1996)
- P. M. Forster and A. W. Sleight, *Inter. J. Inorg. Mater.*, 1, 123 (1999)
- P. M. Forster, A. Yokochi and A. W. Sleight, *J. Solid State Chem.*, 140(1), 157 (1998)
- A. L. Garcia-Ponce, L. Moreno-Real and A. Jimenez-Lopez, *Inorg. Chem.*, 27 (19), 3372 (1988)
- J. Gaubicher, Y. Chabre, J. Angenault, A. Lautie and M. Quarton, *J. Alloys Compd.*, 262, 34 (1997)
- J. Gaubicher, F. Orsini, T. Le Mercier, S. Llorente, A. Villesuzanne, J. Angenault and M. Quarton, *J. Solid State Chem.*, 150(2), 250 (2000)
- Andrew P. Giddy, Martin T. Dove, G. Stuart Pawley and Volker Heine, *Acta Cryst.*, A49, 697 (1993)
- R. Gopal and C. Calvo, *J. Solid State Chem.*, 5, 432 (1972)
- Richard B. Hahn, *J. Am. Chem. Soc.* 73, 5091 (1951)
- S. Z. Haider, *Anal. Chim. Acta*, 24, 250 (1961)
- S. Z. Haider, *Proc. Pakis. Acad. Sci.*, 1, 19 (1964)
- Kenton D. Hammonds, Martin T. Dove, Andrew P. Giddy and Volker Heine, *Am. Mineral.*, 79, 1207 (1994)

- E. Husson, F. Genet, A. Lachgar and Y. Piffard, *J. Solid State Chem.*, 75(2), 305 (1988)
- A. J. Jacobson, *Intercalation Chemistry* (M. S. Whittingham and A. J. Jacobson, Eds), p260. Academic Press, NY 1982
- A. J. Jacobson, J. W. Johnson, J. F. Brody, J. C. Scanlong and J. T. Lewandowski, *Inorg. Chem.*, 24, 1782 (1985)
- Jack Wayne Johnson and Allan Joseph Jacobson, Eur. Patent EP 81-305298, 1982
- Jack W. Johnson and Allan J. Jacobson U. S. Patent 82-40356, 1984
- Byron Jordan and Crispin Calvo, *Can. J. of Chem.*, 51, 2621 (1973)
- Jaroslava Kalousova, Jiri Votinsky, Ludvik Benes, Klara Melanova and Vitezslav Zima, *Collect. Czech. Chem. Commun.*, 63(1), 1 (1998)
- Mohd. Mahfooz Khan, Naseer Ahmad, A. U. Malik, *J. Inorg. Nucl. Chem.*, 31(9), 2955 (1969)
- N. Khosrovnavi and A. W. Sleight, *J. Solid State Chem.*, 121, 2 (1996)
- N. Khosrovani and A. W. Sleight, *J. Solid State Chem.*, 132, 355 (1997)
- P. Kierkegaard and J. M. Longo, *Acta Chem. Scand.*, 19, 1906 (1965)
- P. Kierkegaard and J. M. Longo, *Acta Chem. Scand.*, 24, 427 (1970)
- P. Kierkegaard, J. M. Longo and Bengt-Olov Marinder, *Acta Chem. Scand.*, 19 (3), 763 (1965)
- P. Kierkegaard and Margarita Westerlund, *Acta Chem. Scand.*, 18, 2217 (1964)
- N. Kinomura, T. Toyama and N. Kumada, *Solid State Ionics*, 78, 281 (1995)
- V. Korthius, N. Khosrovani, A. W. Sleight, N. Roberts, R. Dupree and W. W. Wareen Jr., *Chem. Mater.*, 7, 412 (1995)
- N. Kumagai, N. Ikenoya, I. Ishiyama and K. Tanno, *Solid State Ionics*, 28, 862 (1988)
- M. Kuntz and D.I. Brown, *J. Solid State Chem.*, 115, 395 (1995)
- Gerhard Ladwig, *Z. Chem.*, 20(2), 70 (1980)

- A. C. Larson and R. B. Von Dreele, LANSCE, Los Alamos National Lab, Los Alamos, NM, 1994
- A. LeBail, H. Duroy and J. L. Fourquet, *Mat. Res. Bull.*, 23, 447 (1988)
- A. LeClaire, H. Chahboun, D. Groult and B. Raveau, *Z. fur Krist.*, 177, 277 (1986)
- Ernest M. Levin and Robert S. Roth, *J. Solid State Chem.*, 2, 250 (1970)
- L. Lezama, K. S. Suh, G. Villeneuve and T. Rojo, *Solid State Commun.*, 7614, 449 (1990)
- J. M. Longo and R. J. Arnott, *J. Solid State Chem.*, 1, 394 (1970)
- John M. Longo and Peder Kierkegaard, *Acta Chem. Scand.*, 20, 72, (1966)
- J. M. Longo, J.W. Pierce and J. A. Kafalas, *Mat. Res. Bull.*, 6, 1157 (1971)
- Maple Software, Waterloo Maple Inc., 1996
- M. Martinez-Lara, A. Jimenez-Lopez, L. Moreno-Real, S. Bruque-Gamez, B. Casal and E. Ruiz-Hitzky, *Mater. Res. Bull.*, 20, 549 (1985)
- M. Martinez-Lara, L. Moreno-Real, A. Jimenez-Lopez, S. Bruque-Gamez and A. Rodriguez-Garcia, *Mater. Res. Bull.*, 21, 13 (1986)
- T. A. Mary, J. S. O. Evans, A. W. Sleight and T. Vogt, *Science*, 272, 90 (1996)
- Ikuya Mastuura, Tomohiro Ishimura, Satoko Hayakawa and Naomasa Kimura, *Catal. Today*, 28(1,2), 133 (1996)
- Heiko Mathis, Robert Glaum and Reginald Gruehn, *Acta Chem. Scand.*, 45, 781 (1991)
- G. Matsubayashi and S. Ohta, *Chem. Lett.*, 787 (1990)
- Helen D. Megaw, *Mat. Res. Bull.*, 6, 1007 (1971)
- W. M. Meier and H. Villiger, *Z. Kristallogr.*, 129, 161 (1966)
- Klara Melanova, Ludvik Benes, Viteslav Zima and Regina Vahalova, *Chem. Mater.*, 11, 2173 (1999)
- M. Morris, J. M. Adams and A. Dyer, *J. Mater. Chem.*, 1, 43 (1991)

- Y. Piffard, S. Oyetola, A. Verbaere and M. Tournoux, *J. of Solid State Chem.*, 63, 81 (1986)
- Y. Piffard, A. Verbaere, S. Oyetola, S. Deniard-Courant and M. Tournoux, *Eur. J. Solid State Inorg. Chem.*, 26(2), 113 (1989)
- A. L. Ponce, X. Lin and J. J. Fripat, *Solid State Ionics*, 84(3,4), 213 (1996)
- C. R'Kha, T. Vandenborre and J. Livage, *J. Solid State Chem.*, 63, 202 (1986)
- Manuel Roca, M. Dolores Marcos, Pedro Amoros, Jaime Alamo, Aurelio Beltran-Porter and Daniel Beltran-Porter, *Inorg. Chem.*, 36, 3414 (1997)
- E. Rodriguez-Castellon, A. Jimenez-Lopez, M. Martinez-Lara and L. Moreno-Real, *J. Inclusion Phenom. Mol. Recogn. Chem.*, 5, 335 (1987)
- Roy Rustum, D. K. Agrawal and H. A. McKinstry, *Annu. Rev. Mater. Sci.*, 19, 59 (1989)
- Deborah L. Serra and Shiou-Jyh Hwu, *Acta Cryst.*, C48, 733 (1992)
- R. D. Shannon, *Acta Cryst.*, A32, 751 (1976)
- Ikuyo Shiozaki, *J. Phys.: Condens. Matter*, 10, 9813 (1988)
- R. Siskova, L. Benes, V. Zima, M. Vlcek, J. Votinsky and J. Kalousova, *Polyhedron*, 12, 181 (1993)
- Jorge Skibsted, Claus J. H. Jacobsen and Hans J. Jakobsen, *Inorg. Chem.*, 37, 3083 (1998)
- A. W. Sleight, *Inorg. Chem.*, 37, 2854 (1998)
- Harold T. Smyth, *AIP Conf. Proc.*, 3, 244 (1972)
- G. T. Stranford and R. A. Condrate Sr., *J. Mat. Sci. Letters*, 3, 303 (1984)
- G. T. Stranford and R. A. Condrate Sr., *J. Solid State Chem.*, 52, 248 (1984)
- G. T. Stranford and R. A. Condrate Sr., *J. Solid State Chem.*, 76, 407 (1988)
- G. T. Stranford and R. A. Condrate, Sr., *J. Solid State Chem.*, 85, 326 (1990)
- M. Tachez, F. Theobald and E. Bordes, *J. Solid State Chem.*, 40, 280 (1981)

- F. Taulelle, C. Sanchez, J. Livage, A. Lachgar and Y. Piffard, *J. Phys. Chem. Solids*, 49(3), 299 (1988)
- M. Ulutagay, M.S. Thesis, Clemson University, Clemson, SC, 1997
- Mutlu Ulutagay, George L. Schimek, Shiou-Jyh Hwu and Hanna Taye, *Inorg. Chem.*, 37 (7), 1507 (1998)
- Ya. S. Usmanhodzhaeva, O. F. Khodzhaev, Z. M. Musaev and N. A. Parpiev, *Uzb. Khim. Zh.*, 1, 6 (1984)
- Jiri Votinsky, Ludvik Benes, Jaroslava Kalousova and Jiri Klikorka, *Inorg. Chim. Acta*, 126(1), 19 (1987)
- Anil Wali, S. Unnikrishnan, S. Pillai and S. Satish, *Indian J. Chem. Technol.*, 5(3), 172 (1998)
- Xiqu Wang, Lumei Liu, Heidi Cheng and Allan J. Jacobson, *Chem. Commun.*, 24, 2531 (1999)
- J. L. Waring and R. S. Roth, *J. Res. Nat. Bur. Stand., Sect. A*, 69, 2, 119 (1965)
- K. West, B. Zachau-Christiansen, S. Skaarup and T. Jacobsen, *Solid State Ionics*, 53, 356 (1992)
- Osamu Yamaguchi, Yasumichi Mukaida and Hiroyasu Shigeta, *J. Am. Ceram. Soc.*, 72 (10), 1914 (1989)
- V. Zima, L. Benes, J. Malek and M. Vlcek, *Mater. Res. Bull.*, 29, 687 (1994)
- Vitezslav Zima, Ludvik Benes and Klara Melanova, *Solid State Ionics*, 106(3,4), 285 (1998)
- V. Zima, L. Benes and K. Melanova, *Solid State Ionics*, in press
- V. Zima, L. Benes, R. Siskova, P. Fatena and J. Votinsky, *Solid State Ionics*, 67, 227 (1994)
- V. Zima, L. Benes, J. Votinsky and J. Kalousova, *Mol. Cryst. Liq. Cryst. Sci. Technol., Sect. A*, 224, 121 (1994)
- V. Zima, L. Benes, J. Votinsky and J. Kalousova, *Solid State Ionics*, 82, 33 (1995)
- V. Zima, M. Vlcek, L. Benes, L. Casciola, L. Massinelli and R. Palombari, *Chem. Mater.*, 8, 2505 (1996)